Quantum chemical investigation towards Raman enhancement effects.

seit 1558

Dissertation

(kumulativ)

zur Erlangung des akademischen Grades doctor rerum naturalium

(Dr. rer. nat.)

vorgelegt dem Rat der Chemisch-Geowissenschaftlichen Fakultät der
Friedrich-Schiller-Universität Jena

von Federico Latorre

geboren am 25.08.1985 in Valencia

Abstract

A well-known drawback of Raman spectroscopy is the low signal intensity. Therefore, the present thesis aims to elucidate the fundamental principles in state-of-the-art signal-enhanced Raman spectroscopy, i.e. resonance Raman (RR), surface-enhanced Raman scattering (SERS) and tip-enhanced Raman scattering (TERS).

Firstly, a new approach to evaluate RR scattering is discussed. This new approach, called real-time method, can evaluate the polarizabilitiy tensor in the time domain. The new method is benchmarked by being compared to other two well-known methods. All three methods give comparable results, and consequently, the novel computational approach is validated.

Afterwards, the chemical effect of SERS is studied by means of a theoretical spectroscopic analysis of the *cis/trans*-isomers of a molecular switch, the penta-2,4-dienoic acid, attached to gold clusters of different size (1, 2 and 20 gold atoms). By simulation of vibrational (IR, Raman and RR) and electronic spectroscopy (UV-vis), the effect of the molecule-metal nanoparticle interaction can be studied. Special emphasis is put on the resonance Raman spectra for the study of the isomers. In the present case, resonance Raman scattering is best suited to discriminate between the isomers on the gold clusters.

Finally a full quantum chemical description of the non-resonant chemical effects of the Raman spectrum of an adenine molecule mapped by a silver tip is presented. The tip is modeled as a single silver atom and as a small silver cluster. Pronounced changes in the Raman pattern and its intensities depending on the conformation of the nanoparticle-substrate system are found, concluding that the spatial resolution of the chemical contribution in TERS can be in the sub-nm range.

Abstrakt

Ein bekannter Makel der Raman-Spektroskopie ist die geringe Signalintensität. Daher wurden signalverstärkende Methoden wie Resonanz-Raman (RR) Spektroscopie, ober-flächenverstärkte Raman-Spektroskopie (surface-enhanced Raman spectroscopy; SERS) und spitzenverstärkte Raman-Spektroskopie (tip-enhanced Raman spectroscopy; TERS) entwickelt. Das Ziel dieser Arbeit ist die Wirkmechanismen dieser Techniken aufzudecken.

Zu Beginn wird ein neuer Ansatz zur Berechnung der RR-Streuung diskutiert. Diese neue Methode, die sogenannte Echt-Zeit Methode, ermöglicht die Berechnung des Po-larisierbarkeits tensors in im der Zeitdomäne und wird im Versteich mit zwei etablertë Techniken getestet. Alle drei Methoden erzielen ähnliche Ergebnisse, womit die Echt-Zeit Methode erfolgreich validiert werden konnte.

Als nächstes wurde der chemische Effekt von SERS untersucht. Hierfür wurden die *cis/trans*-Isomere eines molekularen Schalters, Penta-2,4-diencarbonsäure, welche an Gold-clustern verschiedener Größe (1, 2 and 20 Gold-Atome) befestigt sind, mithilfe von theoretischer spektroskopischer Analyse studiert. Durch Simulationen von Schwingungs-(IR, Raman, RR) und elektronischer Spektroskopie konnte der Effekt der Molekül-Metal nanopartikel-Wechselwirkung näher bestimmt werden. Ein besonderer Schwerpunkt wur-de hierbei auf die RR Spektren der Isomere gesetzt. Der Resonanz-Raman-Effekt erwies sich als bestes Mittel zur Unterscheidung der Isomere an den Goldclustern.

Zuletzt wird eine vollständige quantenchemische Beschreibung des nicht-resonanten chemischen Effekts eines Raman Spektrums eines Adeninmoleküls, welches mit einer Sil-berspitze gerastert wurde, präsentiert. Die Silberspitze wurde hierbei entweder als einzel-nes Silberatom oder als kleiner Silbercluster modelliert. Es wurden erhebliche Verände-rungen im Muster und der Intensität der Ramanspektren in Abhängigkeit der genutzten Konformation des Nanopartikel-Substrat-Systems gefunden. Es liegt daher nahe, dass der chemische Einfluss auf TERS im Sub-nanometer-Bereich stattfindet.

Table of Contents

List of Symbols

$\hat{H}$	System Halmitonian operator
Ψ	System Wavefunction
E	System Energy
r	Electron coordinates
R	Nuclei coordinates
$\hat{T}_e$	Electronic Kinetic Operator
$\hat{T}_N$	Nuclear Kinetic Operator
$\hat{V}_e$	Electronic Potential Operator
$\hat{V}_N$	Nuclear Potential Operator
$\hat{V}_{eN}$	Electron-Nuclei Interaction Potential Operator
$\hat{H}_N$	Nuclear Hamiltonian Operator
$\hat{H}_e$	Electronic Hamiltonian Operator
E_e	Electronic Energy
V_i	Potential Operator
Ψ_{iv}	Vibronic Wavefunction
ψ_{iv}	Electronic Wavefunction
χ_{iv}	Vibrational Wavefunction
$\hat{f}$	Fock Operator
χ	Spin-Orbital
ϵ	Eigen Energy
$\vec{x}_i$	Spin-Orbiy coordinate
V^{HF}	Hartree-Fock Potential Energy
E_{corr}	Correctional Energy
E_0^{exact}	Exact Energy
E_0^{HF}	Hartree-Fock Energy
$E_{\mathrm{corr}}^{\mathrm{dynamical}}$	Dynamical Correlation
$E_{\mathrm{corr}}^{\mathrm{static}}$	Static Correlation
ρ	Electron Density
N_e	Number of Electrons

$\lvert\theta_i\rangle$	Kohn-Sham Orbitals
$\langle\rho_i\lvert\nabla_i^2\rvert\rho_i\rangle$	Kinetic Energy of the Kohn-Sham Orbitals
$V_{ne}[\rho]$	Nuclei-Electron Coulomb Interaction
$J[\rho]$	Electron Coulomb Interaction
$E_{\mathrm{XC}}[\rho]$	Exchange-Correlation Functional
$\hat{f}_{\mathrm{KS}}$	Kohn-Sham Operator
ϵ_i	Kohn-Sham Energy
$E_{\mathrm{X}}[\rho]$	Exchange Functional
$E_{\mathrm{C}}[\rho]$	Correlation Functional
t	Time
v_{XC}	Exchange-Correlation Potential
$v_1(r,t)$	External Electric Field
v_{ext}	External Potential
$\hat{U}$	Time-Evolution Operator
$\hat{O}$	Time-Ordering Operator
ϕ^{SF}	Slater Function
N	Normalization Constant
$Y_{m,n}$	Spherical Harmonic
ϕ^{GF}	Gaussian Function
d_{wy}	Contraction Coefficient
X_{wy}	Contracted Gaussian Function
$\hat{H}_{val}$	All-Electron Hamiltonian
$\hat{V}_{pp}$	Pseudopotential Operator
$\hat{P}_l^A$	Projection Operator
Z_{eff}	Nuclear Effective Charge
ω_{ge}	Frequency of the Absorbed Photon
μ_{ge}	Transition Dipole Moment Matrix
$\hat{\mu}$	Dipole Moment Operator
f	Oscillator Strength
R_e	Nuclear Equilibrium Distance
q	Displacement
k	Force Constant
M_{red}	Reduced Mass
E_{vib}	Vibrational Energy
v_e	Vibrational Frequency
μ_0	Permanent Dipole Moment
$\alpha_{\alpha\beta}(\omega)$	Polarizability Tensor

|	
$E_i(\omega)$	Applied Electric Field
σ	Vibrational Raman Cross Section
$d\Omega$	Element of Solid Angle
D	Radiance
I	Intensity
ω_L	Incident Light Frequency
ω_S	Scattered Light Frequency
e_0	Electric Field Constant
c	Speed of Light
Γ	Damping Factor
S_l	Scattering Factor
$\tilde{\nu}_L$	Incident Light Wavenumber
$\tilde{\nu}_l$	Normal Mode l Wavenumber
h	Planck's Constant
k_B	Boltzmann's constant
T	Temperature
α_l	Normal Mode l Isotropic Polarizability
γ_l	Normal Mode l Anisotropic Polarizability
$\Delta_{e,l}$	Dimensionless Displacement
A	Signal Amplification

Chapter 1

Introduction

Spectroscopy is the study of the interaction between light and matter, that is heavily used in the fields of physics and chemistry. In the field of chemistry, spectroscopy allows the chemists to analyze complex samples, to characterize new chemical compounds or even to study chemical mechanisms. Spectroscopy acts as a bridge between experiment and theory. Theory gives a microscopic picture which often cannot be obtained in experiments. The overlap between theory and experiment are the observables, i.e. the parameters observed in spectroscopic experiments. If the spectra from theory and experiment are the same, probably the underlying theoretical model is correct. Then further conclusions, beyond the experimentally obtained ones, can be drawn from a detailed theoretical analysis. In this thesis, different kinds of spectroscopic methods, are employed to analyze various problems, as outlined below. Especially important in this work is the so-called Raman spectroscopy and its variants.

Historically, Raman scattering dates back to 1928, when the indian physicist C. V. Raman and his collaborator published a series of papers[1–4] that proved the existence of a new kind of effect. This new effect was named Raman scattering and in 1930, Raman was awarded with the Nobel Prize in physics for his discovery and became the first Asian scientist to receive this prestigious award.

Light scattering happens when a light beam passes through a transparent medium without absorption, but nevertheless, an attenuation of the intensity of the passing beam is observed because particles hit by the incident light-beam (ω_i) can act as a scattering center emitting secondary radiation (ω_f), thus dissipating energy to all directions. If $\omega_i = \omega_f$, the process is called elastic scattering or Rayleigh scattering; if $\omega_i \neq \omega_f$, it is called inelastic scattering or Raman scattering (Fig.1.1). From a microscopic point of view, Raman scattering is the result of the energy difference between an initial vibrational state and the final vibrational state passing through an intermediate excited state during the process. When the intermediate excited state is a virtual excited state we have the

so-called normal Raman scattering, which unfortunately has a critical shortcoming, low sensitivity. This shortcoming results in the need for a high concentration sample to have a detectable Raman signal. Then, variations of this spectroscopic technique that solve this shortcoming are needed to make Raman scattering a more useful tool for chemical purposes.
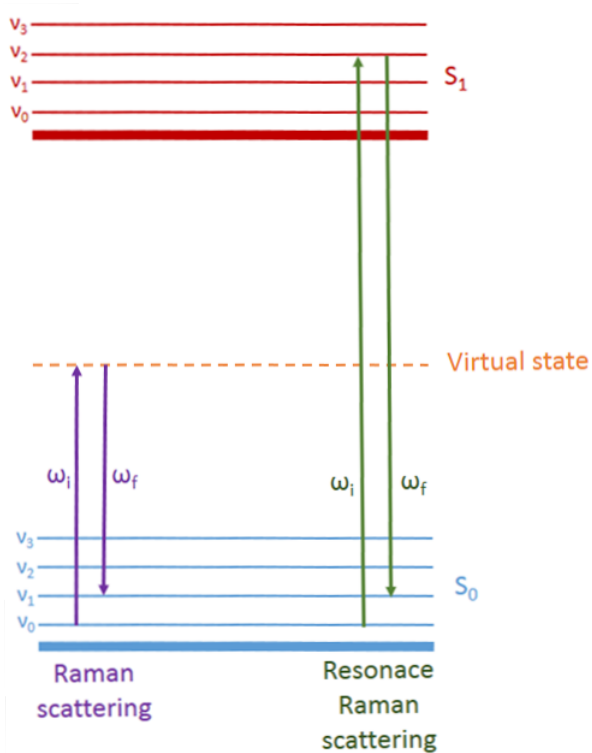
Figure 1.1: Scheme of the Raman scattering (purple) and resonance Raman scattering (green) process.

One of these variations is the so-called resonance Raman scattering (RR),[5] which results in an enhancement of the Raman signal between $10^2 - 10^6$ with respect to normal Raman scattering.[6] In RR, the laser beam is tuned to be similar to the frequency of a bright electronic excited state, which will have the role of the intermediate excited state (Fig.1.1). In addition to the enhancement of the Raman signal, RR features a high selectivity to normal modes that have different gradients in the ground state and the tuned electronic excited state, making this normal modes more intense than the rest (e.g. if the excitation is done to an electronic excited state with a huge contribution $\pi \to \pi^*$, the normal modes related to the corresponding π bonds will be activated more than other ones).[7–10]

Nowadays another variant of Raman scattering called surface-enhanced Raman scattering (SERS) has proven to be quite useful. SERS was observed for the first time in 1974 by Fleischman et al. in an experiment where the Raman spectra of pyridine adsorbed

at a silver electrode was obtained.[11] SERS is a technique that relies on the plasmonic effects[12] that occur in metallic structures (especially on noble metals like silver, gold or platinum) where the sample is adsorbed, resulting in an enhancement of the Raman signal of $10^6 - 10^8$ with respect to the normal Raman scattering.[13] This increase of the Raman signal is explained by two different effects, the electromagnetic effect[13-21] and the chemical effect.[13,22-26] The former corresponds to a creation of a locally confined strong electric field by an incident light source, i.e. a plasmon, on a metallic cluster leading to a pronounced increase of the corresponding Raman signals of a substrate near the metal. The latter chemical effect is correlated to interactions between the molecule and the metallic cluster and can be divided into three different contributions; ground state interactions between substrate and nanoparticle (non-resonant contribution), resonant enhancements of substrate excitations (resonant contribution), and the apparition of new charge transfer states between substrate and nanoparticle (charge-transfer contribution).[13,22] These three contributions can lead to changes in the shape and intensity of Raman spectra due to the different local environment of the substrate under investigation.[20] Because of the different nature of the electromagnetic and chemical effects, the theoretical description of SERS becomes a challenge where different disciplines have to be combined to arrive at a correct picture. While the electromagnetic effect can be studied by using classical electrodynamics, the chemical effect can be studied by using quantum chemical methods, modeling the substrate and a small part of the nanoparticle. Combining these two approaches a hybrid model can be created. For example, Corni and Tomasi,[16-19] Johansson et al.,[27,28] Lopata and Neuhauser,[29] Jensen et al.,[30,31] Chen et al.[32,33] or Thomas et al.[20] introduced different computational methodologies to study plasmonic field effects on a substrate in the scope of SERS by means of a hybrid method combining electrodynamics and quantum chemical approaches.

Additionally, if the setup of SERS is combined with the tip of an atomic force microscope (AFM) or a tip of a scanning tunneling microscope (STM), we obtain tip-enhanced Raman scattering (TERS).[34,35] With this setup, the metalized tip acts as an optical antenna that enhances both the incident and the emitted fields. TERS shares the advantages of SERS but also overcomes the shortcomings of SERS (i.e. the applicability of SERS depends on if the substrate can be adsorbed on the nanoparticle surface, while in TERS the surface can be a silicate) and has interesting additional features: the possibility of single molecule detection[36], extreme sensitivity and high spatial resolution (of 1 nm and below).[34,37-40] Elfick et al[41] predicted atomic resolution for 1 nm radius tips, but unfortunately this tip size is practically impossible to achieve nowadays, with common tip sizes between $10 - 20$ nm of radii.[42-44] Thanks to the high spatial resolution of TERS it will be possible to design experiments where the tip moves across a fixed substrate

making the mapping of molecules a reality.
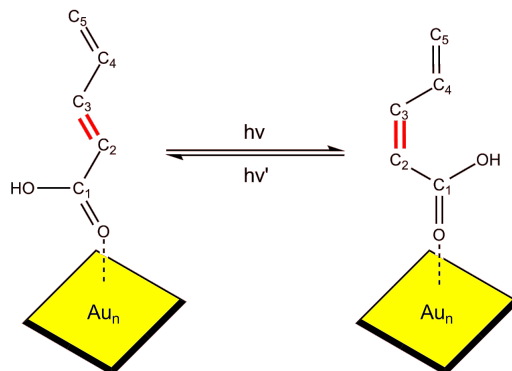
Figure 1.2: An example of a smart surface where a switch molecule, penta-2,4-dienoic acid (PDAH), is anchored on a gold surface. The PDAH shows a *cis-trans* isomerization around the double bond between the C_2 and C_3.

Related to the setup of SERS and TERS are smart surfaces. Such a kind of material can consist of photoswitchable molecules fixed on a conductive surface, for example a metallic cluster or semi-conductor, as can be seen in Fig.1.2.[45,46] Similar smart surfaces have been used to tune the response in applications from dye-based solar cells to sensors[47,48] and molecular electronics.[49] This functionality is due to the ability of photoswitchable molecules to reversibly shift from one microscopic state to another one with electromagnetic radiation of a specific wavelength. The molecules can either revert thermally to the original state or can be reverted by irradiation with light of different wavelength.[50–56] One of the most famous examples of photoswitchable molecules that can be found in nature is the retinal isomerization in rhodopsin, which is responsible for signal conversion in human vision.[57] For the study of such molecules as components of smart surfaces, SERS and TERS are specially suited.[45,58]

The main goal of this thesis is to unravel the details of the mechanisms of SERS and TERS, especially the chemical mechanism, through the use of quantum chemistry. Also the high spatial resolution of TERS is an important topic in this thesis and is studied theoretically to shed light on its causes and how it can be exploited. To achieve these goals, this thesis is divided in several chapters, the theoretical background is presented in Chapter 2, while an overview over the results are shown in Chapter 3 and Chapter 4 collects the appended publications. Finally, in Chapter 5 a summary of this thesis is given.

Chapter 2

Theory

In this chapter the theoretical background for the results presented in this thesis will be introduced. First, the time-independent and time-dependent Schrödinger equations and the Born-Oppenheimer approximation will be described. Then, an overview of the density functional theory and the time-dependent density functional theory will be given. Later, the concept of basis sets will be shortly summarized. Afterwards, it will be explained how relativistic effects are included via effective core potential and then finally the different types of spectroscopy treated in this thesis (absorption, vibrational and Raman scattering) will be presented.

2.1 Basics of Quantum Chemistry

One of the central equations in quantum mechanics is the time-independent Schrödinger equation (TISE):

$$\hat{H}\Psi = E\Psi, \tag{2.1}$$

where $\hat{H}$ is the Hamiltonian operator for a system consisting of nuclei and electrons described by the position vectors R and r, respectively. The expression for this operator is:

$$\hat{H}(r,R) = \hat{T}_{\text{e}}(r) + \hat{T}_{\text{N}}(R) + \hat{V}_{\text{e}}(r) + \hat{V}_{\text{N}}(R) + \hat{V}_{\text{eN}}(r,R), \tag{2.2}$$

where $\hat{T}_{\text{e}}$ and $\hat{V}_{\text{e}}(r)$ are the kinetic energy and potential energy operators for the electrons, $\hat{T}_{\text{N}}(R)$ and $\hat{V}_{\text{N}}(R)$ are the kinetic energy and potential energy operator for the nuclei; and $\hat{V}_{\text{eN}}(r,R)$ is the potential operator for interactions between electrons and nuclei.

In quantum chemistry, one usually seeks the solution of the electronic part of the problem. To this aim, the Born-Oppenheimer (BO) approximation[59] is introduced, which separates the motion of the electrons from the motion of the nuclei, because the mass of the electrons is smaller than the nuclei's mass. Within this approximation the total wave function for a vibronic state can be expressed as:

$$\Psi_{iv}(r, R) = \psi_i(r, \bar{R})\chi_v^i(R), \tag{2.3}$$

where $\psi_i(r, \bar{R})$ is the electronic wave function, which depends on the electron (r) and parametrically on the nuclei coordinates (indicated as $\bar{R}$), and $\chi_v^i(R)$ is the vibrational wave function for the i electronic state and the v for the vibrational state (which depends only in the nuclei coordinates, R).

Therefore, to solve Eq.2.1 we can construct two Hamiltonians, the electronic Hamiltonian $(\hat{H}_e)$ and the nuclear Hamiltonian $(\hat{H}_N)$. The first, $\hat{H}_e$, is given by:

$$\hat{H}_e = \hat{T}_e + \hat{V}_{ee} + \hat{V}_{eN}. \tag{2.4}$$

Consequently, we obtain Eq.2.1 for the electrons as:

$$\hat{H}_e\Psi(r, \bar{R}) = E_e\Psi(r, \bar{R}), \tag{2.5}$$

where, the wave function depends parametrically on the nuclear coordinates and we obtain the energy of the electrons. But there is a problem: we cannot solve Eq.2.1 exactly, except for very small systems, due to the presence of the inter-electronic repulsion term.

The nuclear Hamiltonian, $\hat{H}_N$, can be expressed as:

$$\hat{H}_N = \hat{T}_N(R) + \hat{V}_i(R), \tag{2.6}$$

where $\hat{V}_i(R)$ is the potential operator, which consists of E_e and $V_N(R)$. The eigenvalues of this Hamiltonian are the vibrational-rotational energies.

The first step to solve Eq.2.5 is to make an approach for the wave function $\Psi(r, \bar{R})$. One way to do it is constructing a Slater determinant[60], that fulfills the antisymmetric postulate (or Pauli principle).[61] The determinant is formed by the spin-orbitals for each electron; and these spin-orbitals are the product of the spatial orbital and the spin wave of a given electron. The first procedure that was designed to solve Eq.2.5 and uses the Slater determinant as the total wave function was the Hartree-Fock (HF) method[62], where the following equation has to be solved:

$$\hat{f}(\vec{x}_i)\chi(\vec{x}_i) = \epsilon\chi(\vec{x}_i), \tag{2.7}$$

where $\chi(\vec{x}_i)$ is the spin-orbital of the ith electron (and $\vec{x}$ contains the spatial coordinates r_i and the spin ϖ), ϵ is the eigen energy and $\hat{f}(\vec{x})$ is the Fock operator. This operator introduces the HF potential (V^{HF}) that treats the inter-electronic repulsion of the ith electron with an average field of the rest of the electrons.

The way to solve Eq.2.7 is by an iterative method known as *self consistent field* (SCF), through the eigenvalue problem known as the Roothaan-Hall equations.[63,64]The calculation starts with a guess wave function and then in each step of the iteration, the wave function is improved. This leads to the calculated energy to become lower in each step and the calculation is converged when a certain a threshold is reached (for example that the last calculated energy and the new calculated energy differ by a value lower than the specified threshold energy). The HF method follows the variational principle[65], which means that the obtained energy always will be larger than or at best equal to the exact energy of the system. To understand and measure how much the calculated energy with the Hartree-Fock method differs from the exact energy, Löwdin defined the correlation energy[66] as:

$$E_{corr} = E_0^{exact} - E_0^{HF} < 0, \tag{2.8}$$

where E_0^{exact} is the energy for the exact solution of the non-relativistic Schrödinger equation within the Born-Oppenheimer approximation, and E_0^{HF} is the energy of the Hartree-Fock limit. The E_{corr} is a mathematical fabrication to explain the short-comings of the HF method, but does not mean that it does not have any physical meaning. The E_{corr} can be expressed also as:

$$E_{corr} = E_{corr}^{dynamical} + E_{corr}^{static}, \tag{2.9}$$

where the dynamical correlation, $E_{corr}^{dynamical}$, is due to the approximation of transforming the repulsion interaction between the ith electron with the rest of the electrons in an average field, since the motion of the electrons depends on the immediate positions of all other electrons (which cannot be taken into account within this approximation). The lack of this type of correlation leads to shorter bond distances caused by the too small electron-electron distances (and this is the reason why in the literature it is referred to also as short range effect correlation). The static correlation, E_{corr}^{static}, is due to the description of a system using only one Slater determinant, since not all the systems can be perfectly described by one Slater determinant (e.g. systems with bond breaking, electronically excited states, and transition metals). In the literature this kind of correlation is referred to also as long range effect correlation. Therefore, modern quantum chemistry has the goal to solve the problem of the electron correlation.

2.2 Density Functional Theory Methods

A different approach to solve the electronic Schrödinger equation for ground states is applied in Density Functional Theory (DFT). The cornerstone of modern DFT was laid by the theorems of Hohenberg and Kohn[67], stating a unique relationship of the electronic ground state energy and the electron density as well as the introduction of the variational principle to DFT. The electron density $\rho(r)$ can be expressed as:

$$\rho(\vec{r}) = N_{\mathrm{e}} \int \int |\psi_{\mathrm{e}}(\vec{x}_1, \cdots, \vec{x}_{N_{\mathrm{e}}})|^2 d\varpi_1 d\vec{x}_2 \cdots d\vec{x}_{N_{\mathrm{e}}}. \tag{2.10}$$

The electronic density or probability density $\rho(\vec{r})$ refers to the probability of finding any of the N_{e} electrons in the volume element $d\vec{r}_1$ with any spin, while the remaining $N_{\mathrm{e}} - 1$ electrons have any position and spin in the state represented by the wave function $|\psi_{\mathrm{e}}\rangle$. The electronic density $\rho(\vec{r})$ only depends on the three spatial coordinates of $\vec{r}$, independently of the number of electrons.

2.2.1 Density Functional Theory

In the Kohn-Sham approach, a fictional non-interacting system is constructed, in such a way, that its density behaves as an interacting system. Hence, the initial problem of finding the density of an interacting system, which comes from an interacting wave function, is transformed into finding an operator that can describe a non-interacting system behaving in the same way as an interacting system. In this non-interacting system, the total wave function is exactly given by one Slater determinant of the Kohn-Sham orbitals $|\theta_i\rangle$, which form the electron density according to:

$$\rho = \sum_{i=1}^{N} |\theta_i\rangle\langle\theta_j|. \tag{2.11}$$

Then the electronic energy is given by (here and in the following, atomic units are used):

$$E[\rho] = -\frac{1}{2} \sum_{i=1}^{N} \langle\theta_i|\nabla_i^2|\theta_i\rangle + V_{ne}[\rho] + J[\rho] + E_{\mathrm{XC}}[\rho], \tag{2.12}$$

where $\langle\rho_i|\nabla_i^2|\rho_i\rangle$ is the kinetic energy of the Kohn-Sham orbitals, $V_{ne}[\rho]$ is the Coulomb interaction between the nuclei and the electrons; and $J[\rho]$ is the Coulomb interaction of the electrons. All these terms of Eq.2.12 are well known, with the exception of the term $E_{\mathrm{XC}}[\rho]$, which contains all unknown contributions to the energy: the kinetic correlation

energy, the exchange energy, the Coulombic correlation energy and the self-interaction correction.[68]

Based on the second Hohenberg-Kohn theorem[67], the Kohn-Sham orbitals are found by minimizing the electron energy with respect to the orbitals.[69] As a requisite for this, the Kohn-Sham orbitals have to be orthonormal, leading to the Kohn-Sham equations:[70]

$$\hat{f}_{\text{KS}}|\theta_i\rangle = \epsilon_i|\theta_i\rangle, \tag{2.13}$$

where ϵ_i are the Kohn-Sham energies and $\hat{f}_{\text{KS}}$ is the Kohn-Sham operator, which is expressed as:

$$\hat{f}_{\text{KS}} = -\frac{1}{2}\nabla_i^2 - \sum_{A=1}^{M}\frac{Z_A}{|r_1 - r_A|} + \int \frac{\rho(r_2)}{|r_1 - r_2|}dr_2 + v_{\text{XC}}(r_1). \tag{2.14}$$

With the Kohn-Sham equations, a pathway to determine electron-electron interaction was given. Since the electron density depends only of three spatial coordinates instead on the three coordinates and spin of all N electrons, DFT is a less computationally demanding method than the other electronic structure methods.

However, the weak point of DFT is that the explicit form of an universally valid exchange correlation functional, $E_{\text{XC}}[\rho]$, is unknown. Due to this problem, an approximate $E_{\text{XC}}[\rho]$ must be derived. For this reason, the functional is usually divided in two parts, an exchange and a correlation part:

$$E_{\text{XC}}[\rho] = E_{\text{X}}[\rho] + E_{\text{C}}[\rho]. \tag{2.15}$$

Based on this relation, a variety of different models were developed:

- **Local Density Approximation (LDA)**: The electron density can be treated as a uniform electron gas. For this kind of exchange correlation functional, the exact expression for the exchange energy can be derived as,

$$E_{\text{x}}^{\text{LDA}}[\rho] = -\frac{9\alpha}{8}\left(\frac{3}{\pi}\right)^{\frac{1}{3}}\int \rho^{\frac{4}{3}}(r)dr, \qquad \text{where} \qquad \alpha = \frac{2}{3}, \tag{2.16}$$

  unfortunately, it is not possible to obtain an analytic expression for the correlation, although it can be determined by quantum Montecarlo simulation. Problematic might be also that actual chemical systems are not a uniform electron gas. An example of a LDA functional is the Slater[71], Vosko, Wilk and Nusair functional (SVWN)[72]. A variation of the LDA functional is the Local Spin-Density Approximation (LSDA)[73], which is an extended version for open-shell systems.

9

- **Generalized Gradient Approximation (GGA)**: Extension of the LDA model by means of the gradient of the electron density, which allows to go beyond an universal electron gas to actual chemical systems. Examples of this kind of exchange correlation functional are BLYP (a combination of the Becke's exchange functional (B)[74] and the the correlation functional of Lee, Yang and Par (LYP)[75]), the exchange correlation functional of Perdew and Wang (PW91)[76] or the Perdew, Burke and Ernzerhof (PBE) functional.[77]

- **Hybrid functional**: A mixture of a pure functional (LDA, LSDA or GGA) with some exchange from Hartree-Fock theory. Its general form is:

$$E_{xc}[\rho] = \int_0^1 \langle \psi_{0,\lambda} | V_{XC}^{hole}(\lambda) | \psi_{0,\lambda} \rangle \mathrm{d}\lambda = E_x[\rho] + E_c[\rho], \qquad (2.17)$$

where we apply a perturbation λ that introduces the non-classical interaction between the electrons on the wave function $\psi_{0,\lambda}$, and V_{XC}^{hole} is the exchange correlation hole potential. The perturbation λ can have a value between 0 and 1 and activates the electron-electron non-classical interaction. When $\lambda = 0$, the system behaves as non-interacting system, which only has exchange contribution (there is no correlation energy); and when $\lambda = 1$, there is full correlation contribution in addition to the exchange energy. At $\lambda = 0$ it is known the exact solution (since is the exchange contribution of a Slater determinant), but at $\lambda = 1$ the exact solution is unknown, and further approximations have to be applied (for example, expressing λ as a linear function[78]). One of the most common hybrid functionals is the B3LYP functional, created by Becke in 1993:

$$E_{xc}^{B3LYP} = (1 - a_0)E_x^{LSDA} + a_0 E_x^{HF} + a_x E_x^{B88} + a_c E_c^{LYP} + (1 - a_c)E_c^{VWN}. \qquad (2.18)$$

B3LYP uses HF exchange with B88[74] and the LSDA to account for the exchange energy and the LYP[79] and VWN[72] functionals for electron-electron correlation. The mixing of the individual functionals, given by the parameters $a_0 = 0.20$, $a_x = 0.72$ and $a_c = 0.81$, was obtained by fitting to experimental atomization energies.[78]

An extention of this functional is CAM-B3LYP[80], which introduces a distance dependency of the HF and B88 exchange ratio to add long-range effects in the B3LYP functional:

$$\frac{1}{r_{12}} = \frac{1 - [a_0 + a_b \cdot \mathrm{erf}(\mu r_{12})]}{r_{12}} + \frac{a_0 + a_b \cdot \mathrm{erf}(\mu r_{12})}{r_{12}} . \qquad (2.19)$$

where the three parameters $a_0 = 0.19$, $a_b = 0.46$ and $\mu = 0.33$ control the mixing of E_x^{HF} and E_x^{B88}. The amount of HF exchange is given by $a_0 + a_b$, hence CAM-B3LYP uses at zero electron-electron distance 19 % and at infinite distance 65 % of exact-exchange.

2.2.2 Time-dependent Density Functional Theory and linear response theory

Runge and Gross developed a theorem[81] that extends the principles of DFT to time-dependent problems. Analogous to DFT, where the Kohn-Sham operator is used in the TISE (Eq.2.1), the Runge-Gross theorem starts from a time-dependent variant of the Kohn-Sham operator, $\hat{f}_{\text{KS}}(r_1, t)$ inserted in the time-dependent Schrödinger equation:

$$\hat{f}_{\text{KS}}(r_1, t)\theta_i(r_1, t) = i\frac{\partial}{\partial t}\theta_i(r_1, t) \tag{2.20}$$

and the Kohn-Sham time-dependent operator is expressed as:

$$\hat{f}_{\text{KS}}(r_1, t) = -\frac{1}{2}\nabla_1^2 + v_{\text{KS}}(r_1, t) = -\frac{1}{2}\nabla_1^2 + v_{\text{ext}}(r_1, t) + \int \frac{\rho(r_2, t)}{\mid r_1 - r_2 \mid}dr + v_{XC}(r_1, t), \tag{2.21}$$

where the exchange-correlation potential $v_{XC}(r_1, t)$ is unknown, as in DFT, hence further approximations have to be applied. The most common is the adiabatic approximation, where v_{XC} relies only on the electron density at the current time t. This approximation allows us to use the same exchange-correlation functionals as for the ground state (DFT).

A common way to extract physical properties of the excited states, e.g. the absorption spectrum, is to use linear response theory, giving as result the linear response time-dependent DFT (LR-TDDFT). In LR-TDDFT, the ground state of the molecule is an unperturbed system and then we apply a perturbation $v_1(r, t)$ to excite the molecule. This perturbation can be expressed as an external electric field that is usually included in the external potential:

$$v_{\text{ext}}(r, t) = v(r) + v_1(r, t) = v(r) + r \cdot E_0\cos(\omega\text{t}), \tag{2.22}$$

where the perturbation is turned on at $t = 0$ in this way, the interactions with electric-fields can be investigated, which opens the realm of electronic excited states to DFT. In case that the applied electric field is weak, this interaction can be treated by the linear response theory, obtaining the first-order response of the electron density $\rho_1(r, t)$, given by:

$$\rho_1(r,t) = \int \int \left. \frac{\delta\rho(r,t)}{\delta v_{\text{ext}}(r',t')} \right|_{v(r')} v_1(r',t')dr'dt', \qquad (2.23)$$

where the first term is the linear response function, which can be applied in both Kohn-Sham systems, the non-interacting and the interacting. The linear response function of the interacting system has poles at the real excitation, while the linear response function of the non-interacting system has poles at differences of the Khon-Sham orbitals, but since the linear response of the interacting systems is a function of the linear response function of the non-interacting system, it is necessary to find the latter to solve the former. The linear response function can be found in the non-interacting system applying a first-order time-dependent perturbation to Eq.2.20 and changing the resulting expression to frequency domain by a Fourier transform, obtaining a sum-over-states expression that runs over all Kohn-Sham orbitals. This leads to the loss of the time-dependency in further expressions.

Since the poles of the linear response function of the interacting part are located at frequencies denoted by Ω_k, we can obtain them through an eigenvalue problem.[82] If we choose the Kohn-Sham orbitals to be real and the adiabatic approximation is used:

$$R_{ij,kl}F_k = \Omega_k^2 F_k, \qquad (2.24)$$

where $R_{ij,kl}$ is a matrix which elements are over all possible excitations in the space of the Kohn-Sham orbitals. The eigenvectors F_k characterize the electronic transitions and they can be used to calculate the transition dipole moments (oscillator strengths).

2.2.3   Real Time Time-Dependent Density Functional Theory

Another option used in TDDFT is to calculate the explicit evolution of the system in the time domain and hence the TDSE is explicitly solved for each time step. This method, called real-time TDDFT (RT-TDDFT), is more computationally demanding than standard LR-TDDFT, but is able to calculate non-linear polarizabilities in the presence of large electric fields. In an integral formulation, the Kohn-Sham equations are given by:

$$\theta_i(r,t) = \hat{U}(t,t_0)\theta_i(r,t_0), \qquad (2.25)$$

where the time-evolution operator $\hat{U}(t,t_0)$ is expressed as:

$$\hat{U}(t,t_0) = \hat{O}\exp\left(-i\int_{t_0}^{t} \hat{f}_{\text{KS}}(\tau)d\tau\right), \qquad (2.26)$$

where the time-ordering operator $\hat{O}$ is introduced. To circumvent the application of this operator, the time interval is split into several smaller timesteps, expressing the time-evolution operator $\hat{U}(t, t_0)$ as:

$$\hat{U}(t, t_0) = \prod_{i=0}^{N-1} \hat{U}(t_0 + (i+1)\Delta t, t_0 + i\Delta t), \tag{2.27}$$

where $t = t_0 + N\Delta t$. In each timestep (Δt), the time-dependence of the Kohn-Sham operator in Eq.2.26 can be neglected and this simplifies the integral in the exponential giving the expression:

$$\begin{aligned}
\hat{U}(t, t_0) &= \hat{O}\exp\left(-i\hat{f}_{\text{KS}} \int_{t_0}^{t} (\tau)d\tau\right) \\
&= \hat{O}\exp\left[-i\hat{f}_{\text{KS}}\left(t - t_0\right)\right].
\end{aligned} \tag{2.28}$$

Then, to evaluate Eq.2.25, the time-evolution operator $\hat{U}$ has to be applied numerically. An overview and further details can be found in Ref.[83]

2.3 Basis Sets

The TISE (Eq.2.1) belongs to the class of differential equation problems, which are difficult to solve computationally since it is difficult to program an algorithm able to solve these kind of equations. A way to avoid this problem is introducing basis sets. A basis set in theoretical and computational chemistry is a set of functions which are combined linearly to create molecular orbitals. Using basis sets to construct the wave function allows to transform the differential equation problem into a linear algebra problem, which is easier to solve numerically. For convenience, the functions that compose the basis set are typically atomic orbitals of the hydrogen atom centered at the different atoms of the investigated system, but theoretically can be any function. One of the most used type of basis set is the *Gaussian Type basis set*, that was used in this thesis.

2.3.1 Gaussian Type Basis Set

In 1930[84], the physicist J.C. Slater used a simplified version of the orbitals obtained from the exact solution of the TISE equation for the hydrogen atom to create a kind of orbital that was named after him, the Slater type orbital (STO). The general form of a STO is:

$$\phi^{SF} = NY_{\mathrm{m,n}} r^n exp^{-\zeta r}, \tag{2.29}$$

where r is the distance of the electron from the atomic nucleus, the $Y_{\mathrm{m,n}}$ are spherical harmonics, N is the normalization constant and the exponential factor ζ determines the long-range decay of the function. This kind of orbital possesses exponential decay at long range and Kato's cusp condition[85] at short range. The main shortcoming of these type of orbitals are the three- and four-center two-electron integrals, because they are very difficult to solve in a computational way.

Later, in 1950, Boys[86] applied the *product theorem* in the field of quantum chemistry. This theorem states that the product of two Gaussian functions located on different centers is a new Gaussian function (ϕ^{GF}) located on a new center. This theorem leads to the use of the Gaussian type orbitals (GTOs), which shows a decrease of the computational time for the SCF calculation in comparison with the STO, since the GTOs are easier to treat computationally than the STOs.

The mathematical expression for the Gaussian functions used by Boys is:

$$\phi^{GF} = Nx^i y^j z^z exp^{-\alpha r^2}, \tag{2.30}$$

where i, j and z are non-negative integers, x, y and z are the radial functions and α is a positive orbital exponent. Because an individual primitive Gaussian function gives a rather poor description for the electronic wave function near the nucleus, Gaussian basis sets are a linear combination of primitive Gaussian functions (also called contracted):

$$X_{wy} = \sum_{w=1}^{L} d_{wy} \phi_w^{GF}, \tag{2.31}$$

where L is the length of the contraction, ϕ_w^{GF} are the primitive Gaussian function and d_{wy} are the contraction coefficient. The values of the contraction coefficients d_{wy} and the orbital exponent α (of Eq.2.30) are obtained by fitting a contracted Gaussian function to a STO or by finding the contracted Gaussian functions that minimize the SCF energies of atoms. These optimized d_{wy} and α values are stored in the software and treated as constants when a contracted Gaussian function is used in a calculation.

The size of the basis set is determined by the number of basis function in a linear combination of them. A minimal basis set contains only the minimum number of basis functions (one function per atomic orbital) that are needed for each atom. For example, in the hydrogen molecule it will be the linear combination of basis functions for each 1s orbital:

14

$$c_1 X_{1s,1} + c_2 X_{1s,2}. \tag{2.32}$$

The accuracy of the calculation depends on the size on the applied basis set; larger basis sets typically improve the results. One way to increase the size of a basis set is to take more basis functions per atom. As an example, the double zeta valence basis sets are formed by linear combinations of two sets of functions for each atomic valence orbital. Similarly, triple split valence basis sets such as 6-311G[87], use three sets of contracted functions for each valence orbital type.

Another way to improve a basis set is by adding polarization functions and diffuse functions. The first ones, polarization functions, allow for orbitals with angular momentum going beyond the required one for the proper description of the ground state of each atom at the HF level. Polarized basis sets add d-functions to atoms of the second shell and p-functions to first shell atoms (H and He). Diffuse functions allow for orbitals that occupy a larger region of space. Basis sets with diffuse functions are important for systems where electrons may be far away from the nucleus or to describe properties like polarizability that implies that electrons need an increased flexibility.

2.4   Relativistic effects

In this section, we discuss how to treat the relativistic effects computationally, which are related to heavy atoms (as transition metals). There are two levels of theory to treat them, *ab initio* all-electron (AE), where we apply the relativistic effects for all the electrons of the system; and the valence-only (VO) model Hamiltonian, which exclusively applies the relativistic effects for the so called *valence electrons*, while the rest of the electrons, called *core electrons*, are treated by an effective potential. Of course the AE model is the more rigorous approach to treat relativistic effects, but is also more computationally demanding than the VO model, which is the reason why we chose the VO model for the calculations presented in this thesis. Particularly, the Effective Core Potential[88] (ECP), also known as Pseudopotential (PP), was used in this thesis.

2.4.1   Effective Core Potential (ECP)

The AE Hamiltonian for a system with N_v valence electrons and N_N nuclei is given by:

$$H_{\text{val}} = -\frac{1}{2} \sum_i^{N_v} \Delta_i + \sum_{i<j}^{N_v} \frac{1}{r_{ij}} + \sum_i^{N_v} \sum_A^{N_N} \hat{V}_{\text{pp}}^A(i), \tag{2.33}$$

where i and j are the indices for the electrons and A for the nuclei. $\hat{V}_{pp}^A(i)$ is an angular-momentum-dependent (semi local) pseudopotential operator that imitates the electron-nucleus attraction, core-valence repulsion and the core-valence orthogonality:

$$\hat{V}_{pp}^A(i) = V_{loc}^A(r_{Ai}) + \sum_{l=0}^{l_{max}} V_l^A(r_{Ai})\hat{P}_l^A, \tag{2.34}$$

where $\hat{P}_l^A$ is a projection operator on the spherical harmonics centered at the nucleus A:

$$\hat{P}_l^A = \sum_{m=-l}^{l} |Y_{lm}\rangle\langle Y_{lm}|. \tag{2.35}$$

Because of orthogonality considerations, the value of l_{max} should at least be equal to the highest-angular-momentum quantum number present in the core of the atom. The parameters in the local component V_{loc}^A and in the non-local channels V_l^A are variational parameters.

The ECP used in this thesis are *energy-consistent*, this means that the ECP requires that the potential reproduces the all-electron valence energies of a number of different configurations for the atom under consideration. A parametrized analytical form for the pseudopotential is chosen and the parameters are determined by direct fit of the reference energies, which are obtained from AE calculations.

A continuation the expressions for $V_{loc}^A(r)$ and $\hat{V}_{pp}^A$ are solved for the second row core electrons ($s-$ and $p-$electrons, therefore $l_{max} = 1$). The ECPs used in this thesis have a *functional shape*, which prevents singularities at the nucleus. These ECPs are parametrized as a sum of Gaussian functions multiplied by powers of the electron-nucleus separation, which is the standard form accepted by most of the quantum chemistry packages. Expressing the local component from Eq.2.34 as:

$$V_{loc}^A(r) = -\frac{Z_{eff}}{r} + \frac{Z_{eff}}{r}\exp(-\alpha r^2) + Z_{eff}\alpha r\exp(-\beta r^2) + \gamma\exp(-\delta r^2). \tag{2.36}$$

The local component is finite and behaves quadratically for small r. Z_{eff} is the effective charge of the nucleus and α, β, γ and δ are variational parameters. The complete non-local ECP is given by:

$$\hat{V}_{pp}^A = V_{loc}^A + \xi\exp(-\eta r^2)\,|\,0\rangle\langle 0\,| + \mu\exp(-\nu r^2)\,|\,1\rangle\langle 1\,|, \tag{2.37}$$

where $|\,0\rangle\langle 0\,|$ and $|\,1\rangle\langle 1\,|$ are the projection operators with angular momentum 0 and 1 from Eq.2.35; and ξ, η, μ and ν are variational parameters. Due to orthogonality

considerations, the full $s-$ and $p-$core potentials have to be repulsive close to the nucleus where the core electrons reside and become more attractive at larger distances. Hence, the these core potentials are required to have negative curvature at the origin by imposing an additional nonlinear constraint on the variational parameters:

$$\gamma\delta + \xi\eta > 0 \qquad \text{and} \qquad \gamma\delta + \mu\nu > 0. \qquad (2.38)$$

For elements with $d-$core electrons, as silver and gold atoms, Eq.2.34 is described by a single Gaussian function, which has two additional variational parameters and yields one additional constraint.[88]

2.5 Computation of spectral properties

The following section provides insight into the spectroscopic methods applied in this thesis. Firstly, the fundamental principles of UV-vis absorption spectroscopy aiming to investigate the electronic properties are introduced. Afterward, we elucidate the cornerstones of different vibrational methods, namely infrared (IR) and Raman scattering (RS). Finally, three different methods to evaluate the resonance enhanced version of RS, known as resonance Raman scattering (RR), are discussed in detail.

2.5.1 UV-vis spectroscopy

Excitations of electronic states, mainly from the electronic ground state g to an excited state e, are typically in the spectral range extending from the visual region (vis, $700-380$ nm) towards the ultraviolet (UV, $380-10$ nm) and is known as UV-vis absorption. Hence, UV-vis absorption spectroscopy provides insight into the electronic structure of a chemical system.

The intensity pattern of such a spectrum is determined by energetic position of the excited states with respect to the electronic ground state, also reflected in the frequency of the absorbed photon ω_{ge}, as well as the brightness. The brightness of an electronic (single) excitation is correlated to the transition dipole matrix element μ_{ge}:

$$\mu_{ge} = \langle\psi_g|\hat{\mu}|\psi_e\rangle, \qquad (2.39)$$

whereas $|\psi_e\rangle$ and $\langle\psi_g|$ represent the wave functions of the electronic states e and g and $\hat{\mu}$ is the dipole moment operator, which is basically the position operator $\hat{r}$ multiplied by the charge of a electron, e, $\hat{\mu} = e \cdot \vec{r}$.

Normally the oscillator strength[89], f, is used as indicator of the intensity for the UV and is a dimensionless quantity that is proportional to the probability of absorption or emission in a transition. The oscillator strength is expressed as:

$$f = \frac{2}{3}\Delta E(\mu_{ge})^2,$$ (2.40)

where ΔE is the difference between the energy of the electronic excited state and the electronic ground state. Since it is directly proportional to $(\mu_{ge})^2$, when $\mu_{ge} = 0$ and $f = 0$, we have the so-called *dark state*, a state that does not absorb in the energy range of the UV; and in case of $\mu_{ge} \neq 0$, f has a value greater than zero and the transition between excited states has a intensity associated. When the intensity is big enough, we have the so-called *bright state*, a state who is remarkable in comparison with other excited states with lower intensities or with zero intensity.

2.5.2   IR spectroscopy

The infrared (IR) spectrum occurs between transitions on different vibrational states, that commonly are within the same electronic state. The wavelength range between these kind of states are larger than the one in UV (or at lower frequencies), being between $16,000 - 2,500$ nm (or $400 - 4000$ cm^{-1}). IR is specially useful for the recognition of functional groups in organic chemistry, since vibrations of each functional group can be related to one or several normal modes with a specific range of frequencies (or wavelengths). For example, the π bonds can be related to the stretching normal modes (noted by $\nu_{C=C}$), that are between the range of $1600 - 1700$ cm^{-1}; or the acid groups "COOH" can be related to the stretching in the bond O-H (noted by ν_{O-H}), which normally are in the frequency range of $2500 - 3300$ cm^{-1}.

The first step is to construct the Hamiltonian operator of Eq.2.6 to fit the eigenfunctions of $\chi_v^i(R)$, for this goal we expand $V_i(R)$ in a Taylor series around R_e. Taking the displacement $q = R - R_e$, this expansion is expressed as:

$$V(q) = V(0) + \left(\frac{dV}{dq}\right)_0 q + \frac{1}{2}\left(\frac{d^2V}{dq^2}\right)_0 q^2 + \frac{1}{3!}\left(\frac{d^3}{dq^3}\right)_0 q^3 + \cdots$$ (2.41)

The energy at $V(0)$ can be defined as zero, leading to the quadratic term as the first non-zero term. Hence, truncation after the second term leads to a harmonic expansion of the potential for the nuclei:

$$V(q) = \frac{1}{2}\left(\frac{d^2V}{dq^2}\right)_0 q^2 = \frac{1}{2}kq^2,$$ (2.42)

where we defined the force constant k as the second derivative of the potential energy at the minimum energy position. The harmonic approximation gives good results at small energies. However, due to the harmonic nature of V, larger displacements q are hardly described, e.g. making dissociation impossible, as can be seen in Fig 2.1.
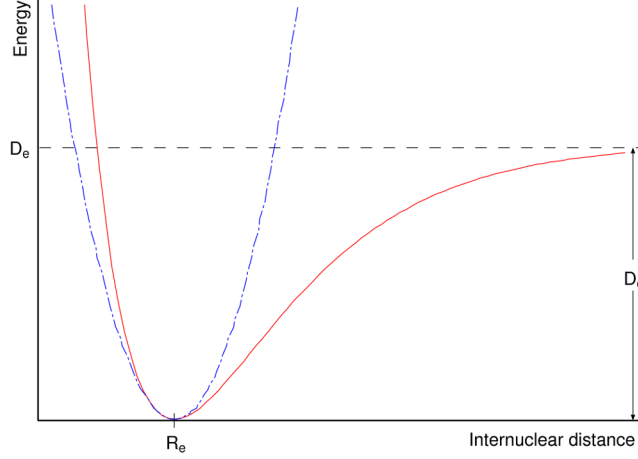
Figure 2.1: Differences between the an anharmonic potential (red, solid line) and an harmonic potential (blue, dashed line).

The kinetic energy operator of the nuclei is expressed as:

$$\hat{T}_{\mathrm{N}} = \frac{\hbar^2}{2M_{red}}\nabla^2_{\mathrm{int}}, \tag{2.43}$$

where ∇^2_{int} is a term that depends in the angular momentum $\hat{L}$, so $\hat{T}_N$ includes both vibration and rotation and M_{red} is the reduced mass, given by:

$$M_{red} = \frac{M_A M_B}{M_A + M_B}, \tag{2.44}$$

where M_A and M_B are the mass for the nuclei A and B. Finally, the Hamiltonian operator of the nuclei is expressed as:

$$\hat{H}_{\mathrm{N}} = \frac{\hbar^2}{2M_{red}}\nabla^2_{\mathrm{int}} + \frac{1}{2}kq^2 \tag{2.45}$$

Applying the nuclear Hamiltonian to the Born-Oppenheimer wave function $\Psi_{iv}(r, \bar{R})$ of equation 2.3 and separating the rotational part form the vibrational part we obtain the vibrational Schrödinger equation:

$$\hat{H}_v \chi^i_v(q) = E_v \chi^i_v(q)$$
$$= \frac{\hbar^2}{2M_{red}} \frac{d^2}{dq^2}\chi^i_v(q) + \frac{1}{2}kq^2\chi^i_v(q), \tag{2.46}$$

whose eigenvalues are:

$$E_v = (v + \frac{1}{2})h\nu_e \qquad (2.47)$$

where v is the vibrational quantum number and ν_e is the vibrational frequency, which is related to the force constant k through $k = 4\pi^2\mu\nu_e^2$. When $v = 0$ at Eq.2.47, $E_v = \frac{1}{2}h\nu_e$, meaning that any system will have an energy associated at $0K$, called *zero-point energy*.[90]

The IR intensity is evaluated according to the transition dipole moment between vibrational states, $\mu_{v,v'}$, which is given by:

$$\mu_{v,v'} = \langle \chi_{v'}|\mu(q)|\chi_v\rangle, \qquad (2.48)$$

$\mu(q)$ can be expanded in a Taylor series as:

$$\mu(q) = \mu_0 + \left.\frac{\partial\mu}{\partial q}\right|_{q=q^0} q + \cdots \qquad (2.49)$$

where μ_0 is the permanent dipole moment and $\left.\frac{\partial\mu}{\partial q}\right|_{q=q^0}$ is the variation of the dipole moment respect to the vibration movement. If we substite Eq.2.49 into Eq.2.48, we obtain:

$$\mu_{v,v'} = \mu_0\langle\chi_{v'}|\chi_v\rangle + \left.\frac{\partial\mu}{\partial q}\right|_{q=q^0}\langle\chi_{v'}|q|\chi_v\rangle, \qquad (2.50)$$

The first term, μ_0 does not depend on q, hence it does not contribute to the IR activity. Then, to have IR activity $\left.\frac{\partial\mu}{\partial q}\right|_{q=q^0} \neq 0$. This term permits vibrational transitions in which $\Delta v = \pm 1$, which are the bands with highest intensity. Higher terms in $\mu(q)$ are the ones responsible for the bands known as *overtones* ($\Delta v = \pm 2, \pm 3, \cdots$), but they cannot be predicted within the harmonic approximation.

2.5.3   Raman Scattering (RS)

The interaction of the incident light with a chemical system is described by the frequency dependency of the dipole moment $\mu_j(\omega)$:

$$\mu_j(\omega) = \sum_i \alpha_{\alpha\beta}(\omega)E_i(\omega) \qquad (2.51)$$

where $\alpha_{\alpha\beta}(\omega)$ is the polarizability tensor of the chemical system depending on the vibrational modes and runs over two independent directions of space (α and β); and

$E_i(\omega)$ is the applied electric field, i and j run over the three independent directions of space (x, y and z in Cartessian coordinates). The polarizability tensor $\alpha_{\alpha,\beta}(\omega)$ can be expanded in a Taylor series:

$$\alpha_{\alpha\beta}(\omega) = (\alpha_{\alpha\beta})_0 + \sum_l \left(\frac{\partial \alpha_{\alpha\beta}}{\partial Q_l}\right)_0 Q_m + \sum_{l,m} \left(\frac{\partial^2 \alpha_{\alpha\beta}}{\partial Q_l \partial Q_m}\right)_0 Q_l Q_m \; \dots \; , \qquad (2.52)$$

where $(\alpha_{\alpha\beta})_0$ is the polarizability in the equilibrium geometry and Q_l and Q_m the corresponding normal coordinates along the lth and mth mode. If the harmonic approximation is applied, Eq.2.52 is truncated in the second term.

To solve Eq.2.51 (within the harmonic approximation), we apply the time-dependent electronic field as $E_i(\omega) = E_0 \vec{e}_{x/y/z} \cos(\omega_L t)$ on the truncated Eq.2.52, obtaining:

$$\mu_j(\omega) = (\alpha_{\alpha\beta})_0 E_0 \vec{e}_{x/y/z} \cos(\omega_L t) +$$
$$\frac{1}{2}\sum_l \left(\frac{\partial \alpha_{\alpha\beta}}{\partial Q_l}\right)_0 E_0 \vec{e}_{x/y/z} Q_l \cos\left((\omega_L \pm \omega_l \pm \delta_l)\, t\right) = \qquad (2.53)$$
$$\mu_j(\omega_L) + \mu_j(\omega_L - \omega_l) + \mu_j(\omega_L + \omega_l)$$

$$,$$

where E_0 is the amplitude of the incidental electric field, $\vec{e}_{x/y/z}$ is the polarization of the electric field, δ_l is the phase factor, and ω_L and ω_l are the frequencies of the incident light and lth vibrational normal mode respectively.

In Eq.2.53, the first term, $\mu(\omega_L)$ is the predominant elastic scattering or Rayleigh scattering. The necessary condition to have Rayleigh scattering is $(\alpha_{\alpha\beta})_0 \neq 0$, meaning that all chemical systems can show Rayleigh scattering, because all molecules can be polarized to a certain extent.

The second and the third terms in Eq.2.53, $\mu_j(\omega_L - \omega_l)$ and $\mu_j(\omega_L + \omega_l)$, are the inelastic or RS[1,91], which describe the Stokes ($\mu_j(\omega_L - \omega_l)$) and Anti-Stokes scattering ($\vec{\mu}(\omega_L + \omega_l)$), respectively. RS occurs when at least one component of the derived polarizability tensor $(\partial \alpha_{\alpha\beta}/\partial Q_l)_0$ of the lth normal mode evaluated at the equilibrium geometry exhibits a non-zero gradient along the coordinate of the normal mode Q_l.

Unfortunately, we cannot obtain information from $(\partial \alpha_{\alpha\beta}/\partial Q_l)_0$ by using classical methods when the frequency of the incident light is in resonance with at least one electronic excited state of the chemical system. This particular case is known as resonance Raman (RR) and quantum mechanics has to be applied to describe it properly.

2.5.4 Resonance Raman Scattering (RR)

The vibrational Raman cross section averaged over all orientations and integrating over all orientations and polarizatations of the scattered light is given by:[5]

$$\sigma_{i \to f} = \frac{\omega_{\text{L}} \omega_{\text{S}}^3}{18\pi e_0^2 c^4} \sum_{\alpha,\beta} \left| (\alpha_{\alpha\beta})_{i \to f} \right|^2 \ , \tag{2.54}$$

where ω_{L} and ω_{S} are the frequencies of the incident and the scattered light, e_0 the electric field constant, c the speed of light and $(\alpha_{\alpha,\beta})_{i \to f}$ the Raman polarizability tensor for a transition from the initial $|i\rangle$ to the final $|f\rangle$ vibrational state. Kramers, Heisenberg and Dirac[92,93](the so-called KHD formalism) derived the Sum-over-States (SOS) expression for the Raman polarizability tensor:

$$(\alpha_{\alpha\beta})_{i \to f} = \frac{1}{\hbar} \sum_n \left(\frac{\langle f|\hat{\mu}_\alpha|n\rangle\langle n|\hat{\mu}_\beta|i\rangle}{\omega_{n,i} - \omega_{\text{L}} - \text{i}\Gamma} + \frac{\langle f|\mu_\beta|n\rangle\langle n|\mu_\alpha|i\rangle}{\omega_{n,f} + \omega_{\text{L}} + \text{i}\Gamma} \right) \ , \tag{2.55}$$

where $\hat{\mu}_\alpha$ is a component of the dipole moment operator, ω_{ni} and ω_{nf} are the frequencies for transitions between two vibrational states defined as $\omega_{ni} \equiv (E_n - E_i)/\hbar$ and $\omega_{nf} \equiv (E_n - E_f)/\hbar$; and Γ is the damping factor due to the finite lifetime of the involved states, describing homogeneous broadening. Unfortunately, the KHD formalism is too complicated to be used in practice. Hence, several approximations have to be made in order to calculate RR intensities. The following approximations are done for three different methods to evaluate Eq.2.55, the *Dynamic polarizabilities method*, the *Real-time method* and the *Vibronic theory method*, that were used in this work:

1. The polarizability tensor of Eq.2.55 holds a *resonant* and a *non-resonant* term ($\frac{\langle f|\hat{\mu}_\alpha|n\rangle\langle n|\hat{\mu}_\beta|i\rangle}{\omega_{n,i}-\omega_{\text{L}}-\text{i}\Gamma}$ and $\frac{\langle f|\mu_\beta|n\rangle\langle n|\mu_\alpha|i\rangle}{\omega_{n,f}+\omega_{\text{L}}+\text{i}\Gamma}$ respectively); the latter is neglected. This approximation is appropriate if ω_{L} is in close resonance with the intermediate vibrational states $|n\rangle$ ($\omega_{\text{L}} \approx \omega_{n,i}$).

2. The electronic and vibrational eigenstates are separated by virtue of the BO approximation.[59]

3. The Condon Principle[94–96] is applied, where the transition dipole moments are assumed to be invariant of the nuclear coordinates:
   $\langle\chi_f\psi_f|\hat{\mu}|\chi_i\psi_i\rangle \approx \langle\chi_f|\chi_i\rangle\langle\psi_f|\hat{\mu}|\psi_i\rangle$
   This approximation is valid for strongly dipole-allowed electronic transitions.

4. The ground and excited states potential energy surfaces (PESs) are assumed to be harmonic, allowing to calculate vibrational states and frequencies of the PESs and thus the Franck-Condon (FC) factors in a straightforward manner.

5. The excited state PESs are assumed to be merely displaced with respect to the ground state equilibrium structure, so that the PESs share the same set of vibrational states and frequencies. This approximation is known as the independent mode displaced harmonic oscillator model (IMDHOM).

6. Intensities for overtone and combination bands are not taken into account.

2.5.4.1 Dynamic polarizabilities method

In the dynamic polarizabilities method[97] (DP), the (normal and resonance) Raman intensities are given by the differential cross sections (in m²/sr), expressed as (averaged of an angle of 180 degrees between the incident and the scattered light):

$$I\left(180\right) = \frac{d\sigma}{d\Omega}\left(180\right) = K_l \left[\frac{S_l}{45}\right], \tag{2.56}$$

where S_l is the scattering factor, which is a purely molecular property. K_l, which is independent of the experimental setup but depends on both incident light and lth vibrational mode frequencies, is given by:

$$K_l = \frac{\pi^2}{\epsilon_0^2}\left(\tilde{\nu}_L - \tilde{\nu}_l\right)^4 \frac{h}{8\pi^2 c\tilde{\nu}_l} \frac{1}{1 - \exp\left(-\frac{hc\tilde{\nu}_l}{k_B T}\right)}, \tag{2.57}$$

where $\tilde{\nu}_L$ and $\tilde{\nu}_l$ are the wavenumbers of the incident light and of the normal mode l, respectively, h is the Planck's constant, k_B is Boltzmann's constant and T is the temperature (set to 300 K).

The scattering factor S_l is expressed as:

$$S_l = 45{\alpha_l}^2 + 7{\gamma_l}^2, \tag{2.58}$$

where α_l and γ_l are the isotropic polarizability and the anisotropic polarizability of the lth normal mode, given by:

$$\alpha_l = \frac{1}{3}\sum_{\alpha}\left(\alpha_{\alpha\alpha}\right)_l, \tag{2.59}$$

$$\gamma_l = \frac{1}{2}\sum_{\alpha\beta}\left[3\left(\alpha_{\alpha\beta}\right)_l\left(\alpha_{\alpha\beta}\right)_l - \left(\alpha_{\alpha\alpha}\right)_l\left(\alpha_{\alpha\alpha}\right)_l\right]. \tag{2.60}$$

The polarizability tensor is evaluated by expanding it in a Taylor series about the equilibrium geometry q^0,

$$\alpha_{\alpha\beta}(\omega, q) = \alpha_{\alpha\beta}(\omega, q^0) + \left.\frac{\partial\alpha_{\alpha\beta}}{\partial q}\right|_{q=q^0} + \cdots \tag{2.61}$$

Within the harmonic approximation (section 2.5.2), the first term in the expansion accounts for elastic scattering (also known as Rayleigh scattering) and the second term for the inelastic scattering, the fundamental Raman scattering.

2.5.4.2 Real-time method

The main feature of real-time method (RT) is the use of RT-TDDFT method, shown in section 2.2.3, that can solve the time-dependent Kohn-Sham equations, Eq.2.25, delivering the evolution of the electron density over time. This can be used to calculate the time-dependent dipole moment, Eq.2.51, where $\alpha_{\alpha\beta}$ can be expressed as:

$$\alpha_{\alpha\beta} = \frac{\mu_j(\omega)}{E_i(\omega)} = \frac{\int \mu_j(t)\exp(i\omega t)\exp(-\Gamma t)dt}{\int E_i(t)\exp(i\omega t)dt} \tag{2.62}$$

where a Fourier transform to convert has been applied $\alpha_{\alpha\beta}$ from frequency domain to time domain. Without the exponential damping factor. Γ, the polarizability could only be calculated for non-resonant frequencies.

With $\alpha_{\alpha\beta}$ given by Eq.2.51, the resonance Raman intensity for the lth normal mode is evaluated as the differential Raman scattering cross section shown in Eq.2.56.

2.5.4.3 Vibronic theory method

In the vibronic theory, the Raman polarizability tensor of Eq.2.55 is given here within the transform theory originally derived by Hizhnyakov and Tehver[98–102]:

$$(\alpha_{\alpha\beta})_l = \frac{1}{\hbar} \sum_e (\mu_{g,e})_\alpha (\mu_{g,e})_\beta \frac{\Delta_{e,l}}{\sqrt{2}} \{\Phi_e(\omega_L) - \Phi_e(\omega_L - \omega_l)\} , \tag{2.63}$$

where the summation over e takes all contributing electronic excited states to the RR scattering into account, $(\mu_{g,e})_\alpha$ is a component of the transition dipole moment of the excited state e at the ground state equilibrium geometry, $\Delta_{e,l}$ is the dimensionless displacement of the minimum of the excited state e PES in the lth normal coordinate and ω_l is the frequency of the lth normal coordinate. Summing over the excited states e, we take into account interference effects between the contributing electronic states leading to constructive or destructive effects on the RR intensity pattern. On the basis of $\Phi_e(\omega_L)$ the dependency of the RR signal on the frequency of the incidental light ω_L is described:

$$\Phi_e(\omega_L) = \sum_u \frac{\prod_i^{3N-6} |\langle \chi_{g0_i} | \chi_{eu_i} \rangle|^2}{\omega_{g0,e0} + \sum_j^{3N-6} u_j\omega_j - \omega_L - i\Gamma}. \tag{2.64}$$

The summation of u runs over all vibrational quantum numbers u_i of the respective electronic excited state e, this way the one-dimensional FC factors along the lth vibrational

coordinate are defined. The frequency $\omega_{g0,e0}$ refers to the energy gap between the vibrational ground state in the electronic ground state $|g0\rangle$ and the vibrational excited state in the electronic excited state $|e0\rangle$.

Φ_e can be further simplified if the absorption band features a large broadening and no resolved vibronic structure. In this case, the one dimensional FC factors can be neglected and Φ_e becomes:

$$\Phi_e(\omega_{\mathrm{L}}) = \frac{1}{\omega_{g,e} - \omega_{\mathrm{L}} - \mathrm{i}\Gamma} \, , \tag{2.65}$$

here $\omega_{g,e}$ is the vertical excitation energy within the FC region of the electronic ground state.

The dimensionless displacement $\Delta_{e,l}$ of the excited state e with respect to the ground state g is defined in the IMDHOM by the partial derivative of the excited PES E^e along the mass-weighted normal mode Q_l:

$$\Delta_{e,l} = -\frac{1}{\sqrt{\hbar\omega_l^3}} \left(\frac{\partial E^e}{\partial Q_l} \right)_0 \tag{2.66}$$

$$= -\frac{1}{\sqrt{\hbar\omega_l^3}} L^T M^{-\frac{1}{2}} \left(\frac{\partial E^e}{\partial x_l} \right)_0 \, . \tag{2.67}$$

The partial derivatives along Q_l are obtained from the non-mass-weighted Cartesian coordinates x_l applying the matrix M, containing the atomic masses, and the orthogonal matrix L, obtained from solving the ground state normal mode eigenvalue problem.

Consequently, the RR intensities for a fundamental transition $g0 \rightarrow g1_l$ with respect to the excitation energy ω_{L} are given by:

$$I_{g0 \rightarrow g1_l}(\omega_{\mathrm{L}}) \propto \omega_{\mathrm{L}} \left(\omega_{\mathrm{L}} - \omega_l\right)^3 \sum_{\alpha\beta} \left| (\alpha_{\alpha,\beta})_{g0 \rightarrow g1_l} \right|^2 \, . \tag{2.68}$$

If only one excited state e is in resonance with ω_{L}, Eq.2.68 can be simplified to the so called short-time approximation[103] (STA). This equation neglects the dependency of the relative RR intensities on ω_{L}:

$$I_{e,g0 \rightarrow g1_l} \propto \frac{1}{\hbar\omega_l} \left(\frac{\partial E^e}{\partial Q_l} \right)_0^2 = \omega_l^2 \Delta_{e,l}^2 \, . \tag{2.69}$$

Within the STA the obtained RR intensity is only depending on the frequency of the lth vibrational normal mode and the gradient of the excited state $\partial E^e / \partial Q_l$ within the electronic ground state minimum.

Chapter 3

Results

The results of this thesis are pulished in three articles. In this chapter, each section contains a summary of these papers and is structured as follows: In Sec. 3.1 the validation of the real-time method (RT) to simulate resonance Raman scattering (RR) spectra is discussed. For this goal, *ortho*-Nitrophenol is selected as benchmark model since it has been studied by a variety of computational methods to simulate RR (see Sec. 2.5.4). The results of the real-time method (RT) are compared with the results obtained using the dynamic polarizability mehtod (DP) and the vibronic theory (VT) method within the short-time approximation (STA). In Sec. 3.2 the effect of nanoclusters on how the spectral pattern changes for several spectroscopic techniques is discussed. The computational results of penta -2, 4-dienoic acid (PDAH) isolated and attached to gold nanoclusters are introduced. The PDAH-gold interaction has been investigated based on spectroscopical methods, namely: infrared (IR), absorption (UV), Raman scattering (RS) and resonance Raman scattering (RR); and depending on the cluster size (1, 2 and 20 gold atoms). Furthermore, different bonding scenarios of PDAH to the Au_{20} cluster have been studied, giving a first impression of the chemical effect in surface-enhanced spectroscopy (with special interest on the case of Raman scattering) and how the shape of the plasmon surface affects the intensity pattern. The last section, 3.3, aims to extend the computation model of Sec. 3.2 towards tip-enhanced Raman scattering (TERS). Therefore, a full quantum chemical description of the non-resonant chemical effects on the Raman spectrum is discussed, where we simulate the Raman signal of an adenine molecule when a silver tip is located at different positions. The results show pronounced changes in the Raman pattern and its intensities depending on the conformation of the nanoparticle-substrate system.

3.1 Resonance Raman Spectra of ortho-Nitrophenol Calculated by Real-Time Time-Dependent Density Functional Theory

In this sections of results the paper *Resonance Raman spectra of ortho-nitrophenol calculated by real-time time-dependent density functional theory* by Martin Thomas, Federico Latorre and Philipp Marquetand, published on The Journal of Chemical Physics 138 in 2013 is discussed. Resonance Raman spectroscopy is an important tool in modern analytical chemistry, hence, accurate computational models are essential in order to understand the underlying photophysics of this process. Recently, Chen et al[32] used real-time TD-DFT (RT-TDDFT) to calculate dynamic polarizabilities, avoiding the use of linear response theory. This method was developed to simulate surface enhanced Raman scattering (SERS) spectra, however Thomas et al. derived from this method a formulation (called RT in the following) to allow the simulation of RR spectra.

In this section, the RT method is validated by comparing the simulated RR spectra of *ortho*-Nitrophenol[104] (*o*-NP) using the vibronic theory (VT), within the short-time approximation[103], and the dynamic polarizabilities (DP) method.[97] Besides the use of the different methods, the performance of several functionals and basis sets is benchmarked to test the accuracy of the RT method to simulate RR intensities.

3.1.1 Computational setup

All equilibrium geometries and frequency vibrations in the ground state were calculated at the DFT level of theory using the PBE[77], BLYP[74,75], PBE0[105] and B3LYP[72,74,75] exchange-correlations (XC) functionals, except for the DP. These calculations were performed using the ADF package, which did not feature vibrational frequencies using hybrid functionals (PBE0 and B3LYP) at the time this study was done. The excited state properties were obtained at the TD-DFT level of theory (for the DP and the VT methods) and at the RT-TDDFT level of theory for the RT method, where the same functionals that were applied for the ground state, were used for the excited state properties.

In RT, the polarizabilities were calculated within the theory explained in Sec. 2.5.4.2 using the CP2K quantum program.[106] The Goedecker-Teter-Hutter pseudopotentials[107] and the corresponding polarized valence-double-ζ (DZVP) basis sets were applied to model the molecule.[106] A wavelet Poison solver[108] for the electrostatic interactions under non-periodic boundary conditions was used. The equilibrium geometry was optimized and a subsequent vibrational analysis was performed, where the optimized geometry was

displaced along each of the normal modes on three separate RT-TDDFT trajectories. These trajectories run for 3500 steps with a time step of 0.6 $a.u.$. An electric field of 5.338×10^{-5} $a.u.$ was applied where the three independent directions of space were covered by the three separate trajectories for every geometry. The dipole moment was recorded for all trajectories and was used to calculate the polarizability tensor. A damping factor of 2.7212 $a.u.$ was chosen and the polarizability derivatives were obtained numerically from finite differences with a displacement of 0.02 Å along the Cartesian normal vector mode vectors.

In DP, all calculations were performed with the ADF program package[109] using the double-ζ polarized Slater-type (DZP)[110] basis set, while the quantum chemical calculations in the scope of VT were carried out with the GAUSSIAN 09[111] program using the 6-31G**[112] basis set. The RR intensities were simulated within the short-time approximation(see Eq. 2.69).

3.1.2 Vibrational frequency and Resonance Raman intensity pattern

The applied quantum chemical calculations to simulate RR intensities within RT, DP and VT were performed using basis sets of similar size that are: double-ζ type with p-polarization for hydrogen atoms and one d-type polarization function for heavier atoms. The most notable difference is the Slater Type functions used in the DP calculations, whereas the other two methods use Gaussian type functions. Also in RT the core electrons are modeled by pseudopotentials, but vibrational frequencies and polarizabilities normally are not affected by the core electrons significantly.
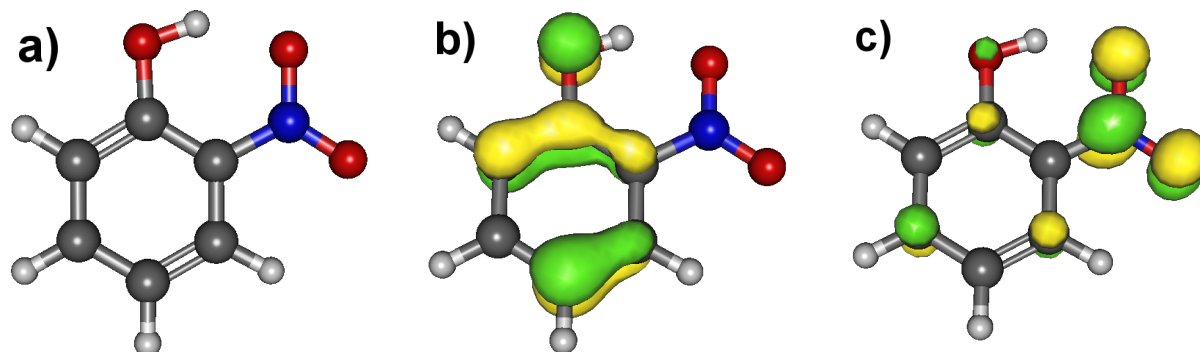
Figure 3.1: Optimized geometry of o-NP (a); and HOMO (b) and LUMO (c) involved in the predominant excited state.

Comparing the frequencies obtained by one chosen functional, the three methods (RT, DP and VT) give a general frequency difference of -10 cm^{-1}, with a few exceptions. These deviations are attributed to the different nature of the basis sets that the programs use. However, the differences in the vibrational frequencies within the same functional are smaller than when using different functionals, where it can be found differences up to 95 cm^{-1}. Considering these findings, it can be stated that the effects of the different nature of the basis sets are smaller than the effect of the different exchange-correlation functional, validating the comparison of the three methods within the same functional.

Before comparing the RR intensity pattern, it is necessary to focus on the electronic energies for the resonant excitation. The experimental absorption spectrum of *o*-NP shows the first absorption band at 3.57 *eV*. All methods predict for the four XC functionals (PBE, PBE0, BLYP and B3LYP) the first excited single state characterized by an electron density transfer from the hydroxil group and the aromatic ring to the nitro group(Fig.3.1(b) and (c)).
The results coincide with Guthmuller's[104] conclusion that the amount of Hartree-Fock exchange in the XC functional has a large influence on the estimated excitation energies. For the *o*-NP, the hybrid functionals PBE0 (3.74 eV for VT) and B3LYP (3.53 for VT) give more accurate results than the PBE (2.99 and 3.00 eV, for VT and DP respectively) and BLYP (2.90 and 2.93 eV, for VT and DP respectively) functionals. Within the framework of RT-TDDFT, the absorption spectrum is calculated by a Fourier transform of the time-dependent dipole moment during the propagations. This is the reason that no individual states are obtained within this method, instead, a whole spectrum is calculated at once, making difficult to characterize the individual transitions. Nonetheless, the obtained absorption spectra using the VT and DP approaches are in good agreement within the functionals and the absorption spectra obtained using the B3LYP with the VT method is in good agreement with the experimental data (3.57 eV).

3.1.3 Method comparison

As stated before, RR spectra were calculated using four different XC functionals: PBE, BLYP, PBE0 and B3LYP. Unfortunately, it was not possible at the time to calculate the RR spectra using the hybrid functionals (PBE0 and B3LYP) with the DP method. Comparing the three methods within the same functional (Fig. 3.2) it can be concluded that there is a good agreement between the three methods, independently of the functional, specially between RT and VT methods. While RT and VT methods show an overall similar intensity pattern with small differences in normal modes of low intensity (located

in the frequency region of $1100 - 1600$ cm^{-1}), the DP method shows more discrepancies in the intensity ratio. The differences between DP and the other two methods can be explained by the different nature of the basis sets between the methods. The differences in the intensity ratio between RT and VT methods can be attributed to a slight mixing of the normal modes because of differences in how the core electrons are treated. Since the RT and DP methods are based on the same idea of calculating the polarizability derivatives, these two approaches have to give equal absolute scattering cross sections as long the same damping factor Γ is used, which is also fulfilled in the calculated spectra. Last but not least, when the calculated spectra are compared to experimental data, the hybrids functionals calculate better simulated RR spectrum than PBE and BLYP.
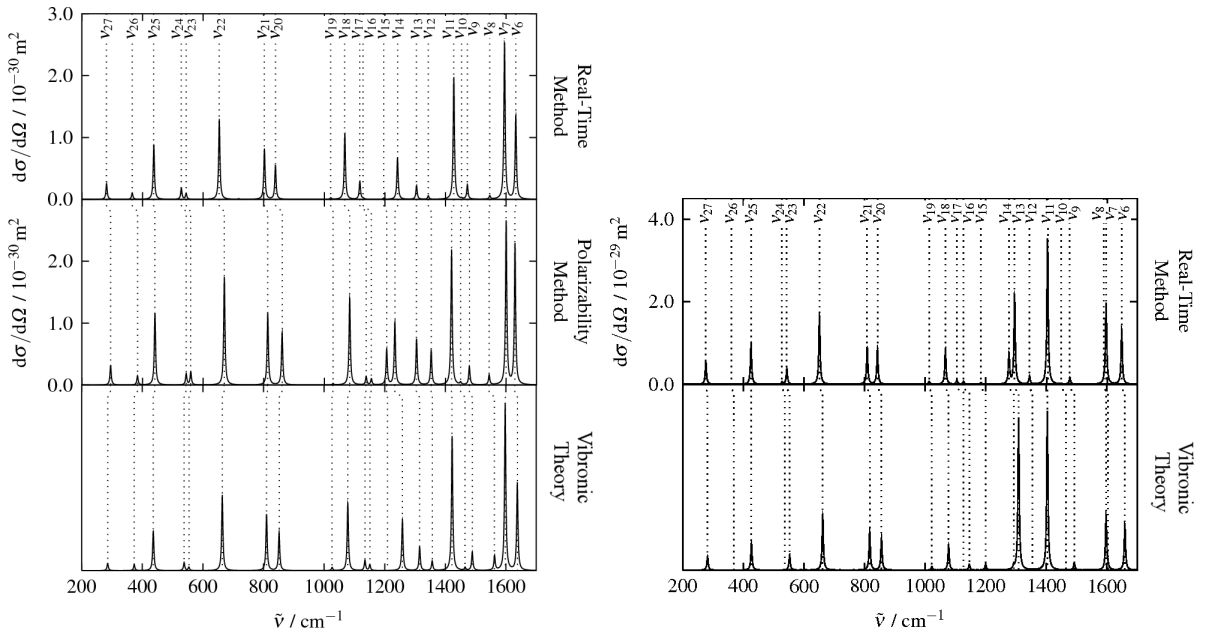
Figure 3.2: On the left the comparison of RRS spectra with PBE functional; on the right comparison of RR spectra with PBE0 functional. Both spectra have peaks broadened by Lorentzian functions with 5 cm^{-1}.

3.1.3.1   Functional and basis set effect

The comparison between functionals reveals remarkable differences only for the modes above 1000 cm^{-1}, below this value the intensity ratios are very similar. Noticeable changes concern the nature of the most intensive normal modes, being different for each functional. This dependency on the functional is reproduced in the same manner by all methods presented here. This proves that the RT, DP and VT give similar RR spectra despite the disparities produced by the different nature of the basis sets used in each method.

31
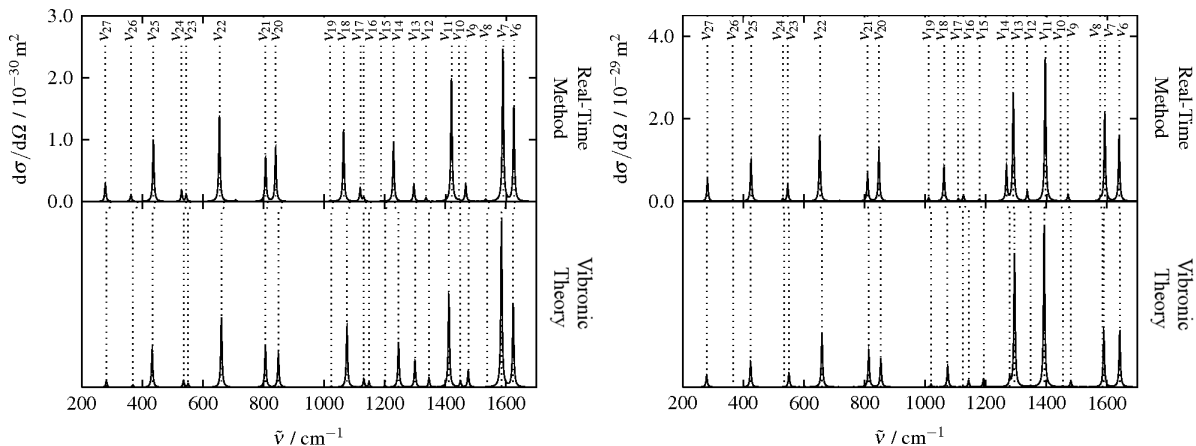
Figure 3.3: On the left the comparison of RR spectra with augmented basis set and PBE functional; on the right comparison of RRS spectra with augmented basis set and PBE0 functional. Both spectra have peaks broadened by Lorentzian functions with 5 cm^{-1}.

To evaluate the influence of the basis set, we performed additional calculations using the PBE and PBE0 functionals using a larger basis set, an augmented double-ζ basis. For this reason we used the aug-DZVP basis set in RT and the 6-31++G** basis set in VT. Comparison of the new spectra (Fig. 3.3) with the ones obtained with the smaller basis sets (Fig.3.2) leads to the conclusion that merely a minor basis set dependency on the RR spectra is obtained for PBE. The frequency differences are lesser than 15 cm^{-1} and also the intensities vary only a bit. Similar conclusions can be taken for the PBE0 spectra. The addition of diffuse functions to the double-ζ basis set does not lead to big differences in the RR spectrum in comparison with the original double-ζ basis set, making this basis set enough for a qualitatively correct prediction of the RR spectrum. Nonetheless, the deviations between the methods for the computation of the RR spectra are reduced by using larger basis sets, supporting the statement that the deviations between the methods can be attributed to the differing nature of the basis sets.

3.1.4 Conclusions

In this section a new approach to calculate RR spectra was presented, based on dynamic polarizabilities as proposed by Jensen and Schatz.[97] However, the polarizabilities are not calculated in the frequency domain using linear response theory, instead the RT-TDDFT method was used.[32] For testing this method, *ortho*-Nitrophenol was used as a model system. The spectra obtained by the RT-TDDFT method were also compared to the vibronic method within the short-time approximation and the dynamic polarizability method. The three methods deliver comparable RR and, therefore, it can be stated that

the calculation of dynamic polarizabilities via RT-TDDFT provides a new alternative to simulate resonance Raman intensities.

3.2 Resonance Raman combined with nanoparticles as a tool for distinguishing the two isomers of penta-2,4-dienoic acid

In this section of results the paper *Resonance Raman combined with nanoparticles as a tool for distinguishing the two isomers of penta-2,4-dienoic acid* by Federico Latorre, Julien Guthmuller and Philipp Marquetand, published on Physical Chemistry Chemical Physics 17 in 2015 is discussed. Here, the results of different simulated spectra (infrared (IR), absorption (UV), Raman scattering (RS) and resonance Raman scattering (RR)) of the penta-2,4-dienoic acid (PDAH) attached to gold nanoclusters of different sizes: Au, Au_2 and Au_{20} are presented. The PDAH was chosen because it presents an *cis/trans* isomerization of the double bond between the carbons 2 and 3 (see Fig.3.4), resulting in an interesting model to study switch molecules. The presence of gold nanoclusters in the systems will affect the shape and intensity pattern of the spectra in a way that the bigger the gold nanocluster, the bigger will be the difference between both isomers. The Au_{20} nanocluster was modeled as a tetrahedral structure[113–115], enabling two different orientations: when one of the faces of the tetrahedron is looking towards the PDAH (called onwards Au_{20} surface) and when one of the peaks of the tetrahedron is pointing at the PDAH (called Au_{20} vertex in the following), see Fig.3.5.
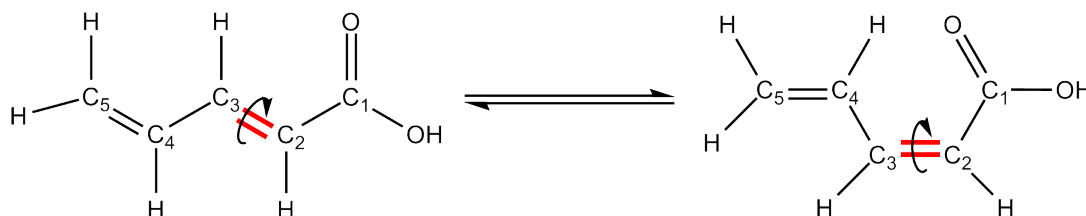

Figure 3.4: Isomerization *cis/trans* of the PDAH. The isomerization occurs in the double bond localized between C_2-C_3.

3.2.1 Computational setup

All the quantum chemical calculations presented in this work have been carried out using the GAUSSIAN 09 program.[111] The optimized geometries and frequencies in the ground state were calculated at the density functional theory (DFT) level[67] using the B3LYP XC functional.[72,74,75] As basis sets, we use 6-311(d)[87] for the description of the PDAH molecule and the quasi-relativistic effective core potential MWB60[88] for the description of the gold nanoclusters. The excited-state properties were obtained at the time-dependent DFT (TD-DFT) level[81] using the same XC functional, basis set and core

potential. All systems are assumed neutral, i.e., the systems with only one Au atom are open-shell systems. For the evaluation of the RR intensities, we used the vibronic theory (also called excited-state gradient method)[116] employing our own code. For the isolated molecule and PDAH-Au cluster, the RR intensities were obtained within the short-time approximation (STA)(eq.2.69). The PDAH-Au$_2$ and specially the PDAH-Au$_{20}$ clusters exhibit several close-lying electronic states which are conjointly excited in a RR process. Therefore, for these systems the sum-over-states (SoS) expression was employed (eq.2.68).

(a)   **(b)**   **(c)**   **(d)**   **(e)**

(f)   **(g)**   **(h)**   **(i)**   **(j)**
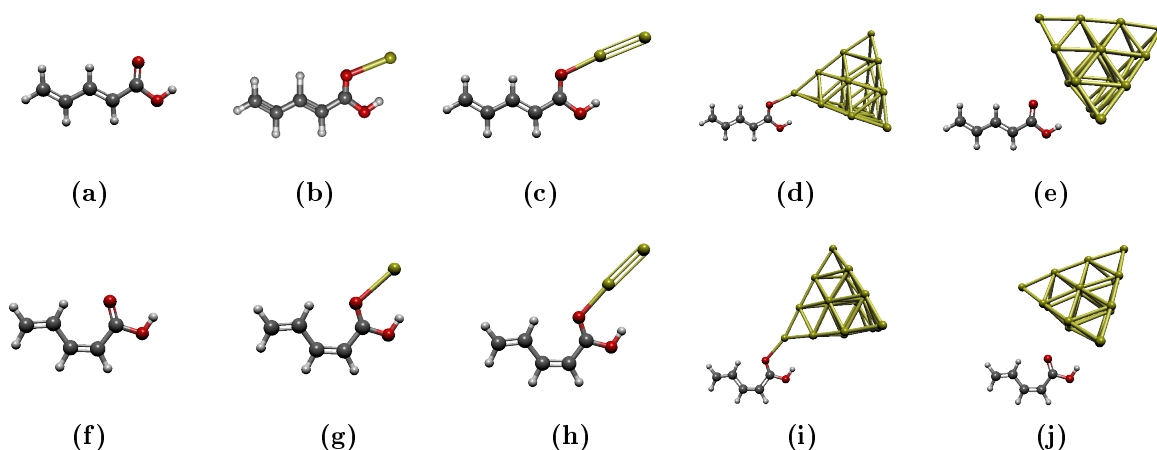
Figure 3.5: The systems under study: (a) *trans*-PDAH, (b) *trans*-PDAH-Au, (c) *trans*-PDAH-Au$_2$, (d) *trans*-PDAH-Au$_{20}$ vertex, (e) *trans*-PDAH-Au$_{20}$ surface, (f) *cis*-PDAH, (g) *cis*-PDAH-Au, (h) *cis*-PDAH-Au$_2$, (i) *cis*-PDAH-Au$_{20}$ vertex and (j) *cis*-PDAH-Au$_{20}$ surface.

3.2.2 Ground state properties

The interaction of the PDAH with the different gold clusters leads to changes in the electronic structure of the organic molecule. This modification is reflected in the geometry. The molecule is attached via its carboxylic oxygen to the gold (Fig.3.5). As a consequence, the bond of the carboxyl group is stretched and the effect is promoted further along the conjugated chain of the PDAH, leading to the following bonds to be contracted and stretched in alternating order. A second effect is that the O-H bond of the acid group is stretched, implying that the bond is weakened and the molecule becomes more acidic.[117] The bond-length changes can be explained by how the electric charges vary with respect to the gold-cluster size. In all calculations, according to a Hirshfeld population analysis, the gold cluster obtains a negative summed partial charge of approximately -0.1 e for the PDAH-Au system and -0.2 e in the other systems. Hence, electron density is transferred from the PDAH to the gold. This process can be seen as a partial enolisation, where the gold acts as a Lewis acid.

An increase of the dipole moment strength with cluster size with exception of the PDAH-Au_{20} surface cluster was founded. In the latter case, the carboxylic O-Au bond is longer, compared to the other systems, due to steric reasons. Hence, the electrostatic interaction is less pronounced and the dipole moment is smaller. When comparing the *trans* and *cis* isomers, we see that already for the pure molecule the *trans* isomers exhibits a stronger dipole moment than the *cis* form. The difference of 0.5 D is retained also for the different Au-cluster systems.

3.2.3   Infrared Spectra

All IR spectra presented in this section (Fig.3.6a)) have been limited to the frequency range from 1000 to 1800 cm^{-1}in order to focus on the normal modes of interest, the single bonds normal modes stretching and specially in the double bonds and C-O normal modes stretching. All frequencies have been scaled by a factor of 0.97 (to account for a systematic error in the DFT predictions)[118] and the intensities were convoluted by Lorentzians of 20 cm^{-1} full width at half maximum (FWHM)[119] to account for line broadening in possible future experimental spectra.

The intensity patterns in the IR spectra show a strong dependency on the size of the cluster. For the isolated molecule, the IR spectrum shows higher peaks in the range of the carbon-carbon single bond modes (ν_{C-C}, 1000-1300 cm^{-1}) than in the double bond modes range ($\nu_{C=C}$ and $\nu_{C=O}$, 1500-1800 cm^{-1}). This intensity ratio changes when the molecule interacts with the gold nanoclusters, and even inverted in the PDAH-Au_2 and PDAH-Au_{20} vertex systems. The PDAH-Au_{20} surface system shows a relative intensity pattern more similar to the PDAH-Au system than the PDAH-Au_{20} vertex system. In addition the absolute intensities of the $\nu_{C=C}$ modes increase when the gold cluster size increases, while the $\nu_{C=O}$ intensities decrease, with exception of the PDAH-Au_{20} surface system.

The frequencies for the normal modes $\nu_{C=C}$ and $\nu_{C=O}$ are also affected by the interaction between PDAH and the gold nanoclusters showing a shift to lower values. The absolute frequencies increase in the following order: PDAH < PDAH-Au_{20} surface < PDAH-Au < PDAH-Au_{20} vertex < PDAH-Au_2.

Looking at how different the intensities and frequencies are affected by the interaction of vertex vs surface in PDAH-Au_{20}, it becomes clear that the binding place on the Au_{20} is of vital importance.[13] Note that our simulations can reproduce only a part of the surface-enhancement infrared absorption (SEIRA) enhancement mechanism, plasmonic contributions[13] or phenomena like hot electrons[120,121] are not described in the present

approach. We show additionally that the above-discussed changes are more pronounced in the *trans* than in the *cis* isomer, because the *trans* isomer is bound closer to the Au cluster than the *cis* isomer. If we want to distinguish between the isomers, conventional IR spectra are expected to be unsuited, since the spectra are very similar because of the broad linewidths.[119] This shortcoming can be solved by using high-resolution spectroscopy[122], since the attachment to gold clusters leads to more pronounced differences in the spectra and makes the differentiation between the isomers easier.
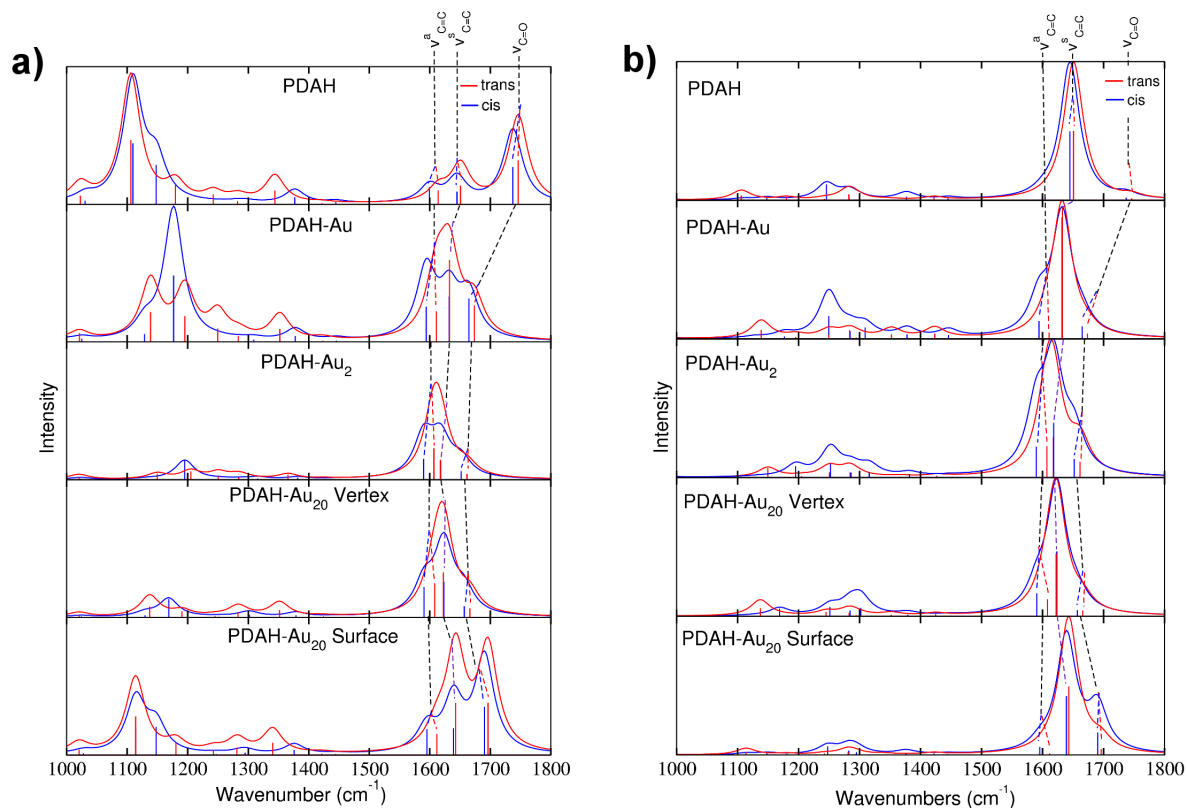
Figure 3.6: a) IR spectra of *trans* (red) and *cis* (blue) isolated PDAH and attached to Gold clusters of different size. The spectra were convoluted by Lorentzians of 20 cm^{-1} FWHM. b) RS of *trans* (red) and *cis* (blue) isolated PDAH and attached to Gold clusters of different size. The spectra were convoluted by Lorentzians of 20 cm^{-1} FWHM. The laser frequency used is 1064 nm.
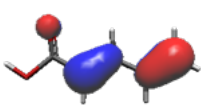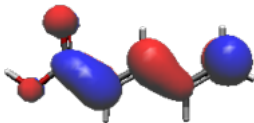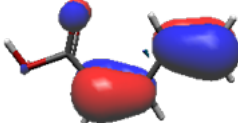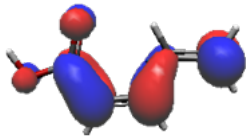
3.2.4   Raman Scattering

The RS spectra presented in this section have been prepared analogously to the IR spectra. Also the RS spectra are shown for the frequency range from 1000 to 1800 cm^{-1} (see Fig. 3.6b)).

Looking at the intensities of the RS spectra, one observes that the $\nu_{C=C}$ modes are dominating while the ν_{C-C} and $\nu_{C=O}$ modes are less intense, but no clear trend is found for the absolute intensities. Nevertheless, the absolute intensities of the $\nu_{C=C}$ and $\nu_{C=O}$ modes are higher for the larger gold clusters. This effect is well-known and contributes to the chemical enhancement mechanism in SERS[13,123] Note that a full simulation of SERS spectra requires incorporating additional mechanisms like the electromagnetic enhancement induced by plasmonic excitations, see e.g. Refs.[13,124] Also the absolute intensities are higher for the PDAH-Au$_{20}$ vertex than for the PDAH-Au$_{20}$ surface system. This fact, once again, shows that the geometry of the metal nanostructure, where the molecule is attached, is important. Additionally, the absolute intensities are higher for the *trans* than for the *cis* systems and also the increase with gold-cluster size is more pronounced for the *trans* isomers. However, this effect in absolute intensity can be rarely observed in experimental spectra since the measurement of absolute scattering cross sections is difficult. Therefore, the RS spectra are normalized with respect to the highest peak of each spectrum as is often done in experiments. In combination with the typical line broadening[125], a distinction between *cis* and *trans* isomers is hardly possibly using RS. Higher resolution is commonly obtained employing RR spectroscopy, which will be discussed below.

3.2.5 Absorption Spectra

In the present study, special attention is paid to states that have an important $\pi \to \pi^*$ contribution(Tab. 3.1), because this transition influences the nature of the double bonds which are key for the *cis*/*trans* isomerization of the PDAH molecule.

| *trans*		*cis*	
π	π^*	π	π^*

Table 3.1: π and π^* Kohn-Sham orbitals of interest for the isolated PDAH molecule calculated at the B3LYP/6-311(d)/MWB60 level of theory.

The absorption spectra (Fig. 3.7a)) reveal how the excited state composition changes for the different molecule-gold clusters. The low energy region of the absorption spectra is governed by metal-center (MC) states, the intraligand (IL) states of interest (with

$\pi \rightarrow \pi^*$ transition) are found approximately between 4.5 and 5.5 eV and the high energy region (above 5.5 eV) is dominated by metal-ligand charge transfer (MLCT) states.

While for the pure PDAH molecule the $\pi \rightarrow \pi^*$ orbitals are important only for a single electronic state, the situation is more complex if gold atoms are added. For the cluster systems, the character of the states of interest is highly mixed and a clear classification of the state character is hence impossible for the larger clusters, not only because of the mixing of transitions but also because the orbitals themselves already show some mixed character. Such mixed orbitals are quite common and further conclusions based on this fact are difficult since in general a specific molecular orbital basis is not unique. However, the observed mixture may indicate that the different parts of the system may not be seen as separate fragments but are entangled to a great extent.

When comparing the *cis* and *trans* isomers, we find it difficult to distinguish the two forms of the respective systems. However, small differences can be found and these will lead to noticeable differences in the RR spectra, as discussed in the next section.
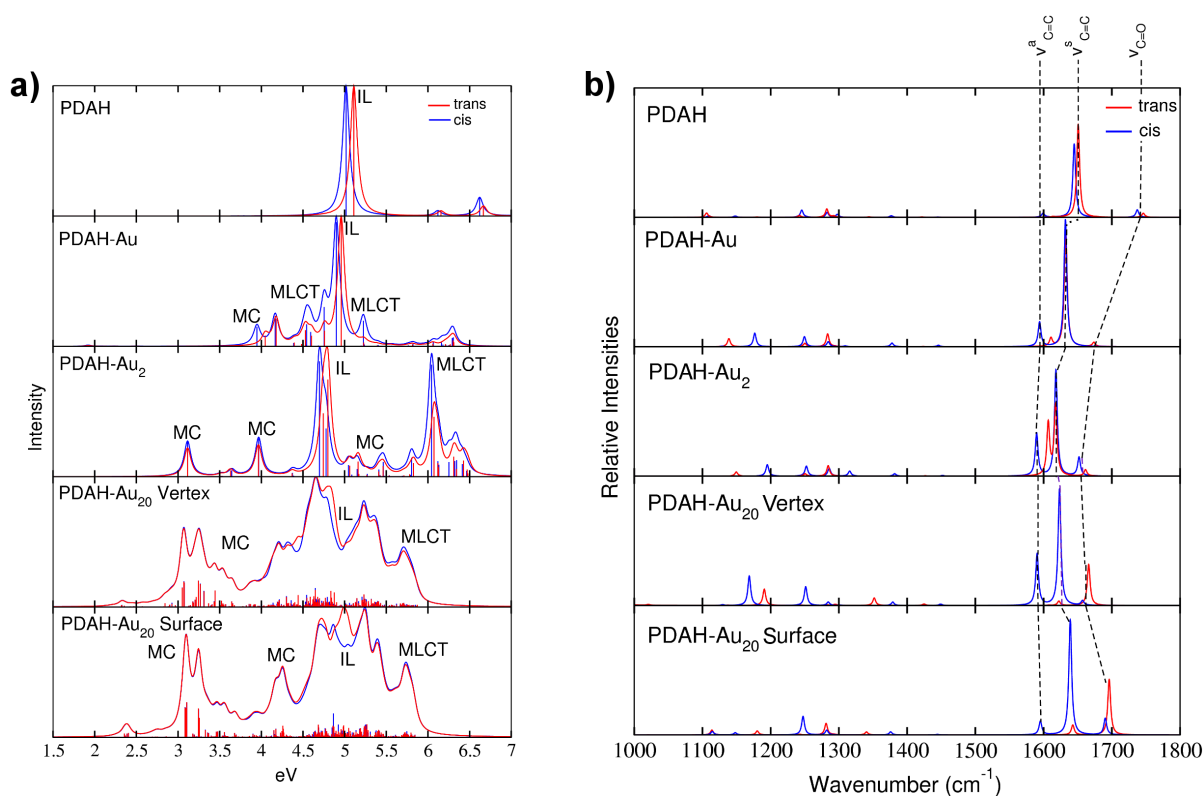
Figure 3.7: a) UV spectra of *trans* (red) and *cis* (blue) isolated PDAH and attached to Gold clusters of different size. The transitions were broadened by Lorentzians of 0.05 eV FWHM. b) RR spectra of *trans* (red) and *cis* (blue) isomers of the various systems. The line spectra were convoluted by Lorentzians of 5 cm^{-1} FWHM.

3.2.6   Resonance Raman scattering

Due to the high-resolution of RR (simulated with a FWHM of $5\,\mathrm{cm}^{-1}$)[104], the two stretching C=C normal modes can be distinguished. They are the the asymmetric C=C stretch ($\nu^a_{C=C}$), and the symmetric C=C stretch ($\nu^s_{C=C}$). The main feature of $\nu^a_{C=C}$ is that one of the C=C double bonds is enlarged while the other C=C double bond is shortened and for $\nu^s_{C=C}$, both C=C double bonds are stretched concertedly. They are indicated in Table 3.2 for the *cis* and the *trans* isomer, respectively.
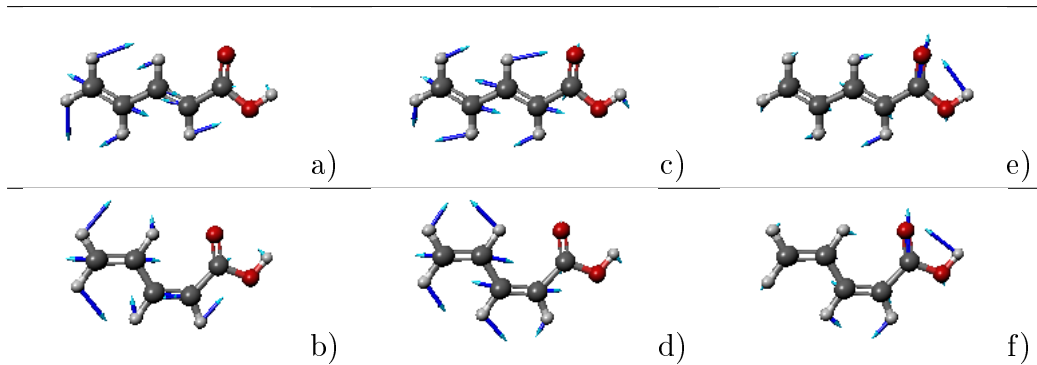
Table 3.2: Normal modes of the *trans* and *cis* PDAH. a) $\nu^a_{C=C}$ for the *trans* isomer, b) $\nu^a_{C=C}$ for the *cis* isomer, c) $\nu^s_{C=C}$ for the *trans* isomer, d) $\nu^s_{C=C}$ for the *cis* isomer, e) $\nu_{C=O}$ for the *trans* isomer, f) $\nu_{C=O}$ for the *cis* isomer.

Fig. 3.7b) shows the RR spectra of the different PDAH systems. The wavelength for the resonant excitation is chosen to match the energy difference between the electronic ground state and the IL states with a strong oscillator strength and the biggest contribution of the transition $\pi \rightarrow \pi^*$. As intended by the choice of the excitation wavelength, the RR spectra are dominated by peaks in the region of the $\nu_{C=C}$ modes.

The RR spectra of the isolated PDAH molecule are very similar comparing the *cis* and *trans* isomers and only minor changes are observed for the PDAH-Au. For the PDAH-Au$_2$ system, differences are visible in the RR spectra, the vibrational mode $\nu^a_{C=C}$ is shifted to higher wavenumbers in the *trans* isomer, while the *cis* isomer exhibits approximately the same frequency as the pure molecule. Differences in the spectra are even more pronounced for the PDAH-Au$_{20}$ clusters. The *trans* isomers of the PDAH-Au$_{20}$ surface and PDAH-Au$_{20}$ vertex systems show an intense peak for the normal mode $\nu_{C=O}$, while the *cis* isomer exhibits an intense $\nu^s_{C=C}$ mode for these systems. Additionally, the mode $\nu^a_{C=C}$ is enhanced in the *cis* isomer of the PDAH-Au$_{20}$ vertex system, while in the *trans* isomer this vibrational normal mode has a very low intensity.

As stated above, the attachment of a molecule to gold nanoparticles leads to significant enhancement of the spectroscopic signals. The spectra presented here predict such SERRS signals, since the chemical effect included in the present calculations is mainly responsible for the relative intensities of the peaks, while plasmonic effects (neglected here) primarily influence the absolute intensities.[123,124] The critical difference in the intensities of the $\nu_{C=C}$ and $\nu_{C=O}$ modes are the reason why both isomers of PDAH can be discriminated in the present case.

3.2.7 Conclusions

In this section, a computational study focused in the discrimination between the *cis* and *trans* isomers of the PDAH molecule attached to gold clusters of different size using different spectroscopic techniques has been presented. It was shown that the interaction between our molecule and the gold clusters leads to a partial enolisation of the two isomers, which affects the intensity pattern of IR and RS spectra. The effect is more pronounced for larger gold clusters, however, the respective *cis* and *trans* isomers show very similar spectra.

Furthermore, we investigated properties of the excited states and simulated UV absorption spectra giving insight into how the interaction between PDAH and Au cluster leads to the mixing between the IL states of the PDAH with the MC states of the Au cluster and becoming more mixed with the increase of the Au cluster size. The data obtained in the UV was used in the simulation of RR spectra and their interpretation.

Finally, we found that RR spectroscopy is a suitable tool for the discrimination of the PDAH isomers attached to gold nanoparticles. The reasons are a high spectral resolution and ,more importantly, the excited-state properties influence the signal strength of vibrational modes differently for the different isomers. Additionally, we have shown that the position where the molecule binds to a larger cluster matters. In the present study, the Au_{20} vertex and Au_{20} surface positions were compared and found to yield different spectra.

3.3 Spatial Resolution of Tip-Enhanced Raman Spectroscopy - DFT Assessment of the Chemical Effect

In this section of results the paper *Spatial Resolution of Tip-Enhanced Raman Spectroscopy - DFT Assessment of the Chemical Effect* by Federico Latorre, Stephan Kupfer, Thomas Bocklitz, Daniel Kinzel, Steffen Trautmann, Stefanie Gräfe and Volker Deckert, published on Nanoscale in 2016 is discussed. The spatial resolution of tip-enhanced Raman scattering (TERS) is studied theoretically within the quantum chemical framework. For this goal, the chemical effects[13] of TERS have been simulated using density functional theory (DFT) calculations for the interaction of adenine with a silver tip. The silver tip was modeled as a single silver atom (Ag atom) and as a small silver cluster (Ag_{20}), and it is located at different positions on the adenine molecule. The adenine was chosen because the adenine-silver nanoparticle interactions have already been widely studied both experimentally and theoretically using surface-enhanced Raman scattering (SERS)[126–129] and TERS.[126,130–132] With this set up, we theoretically investigate "forced" tip-molecule conformations that can only be formed under TERS conditions and study the effects of such geometries on the Raman spectra with respect to the lateral resolution. Furthermore, the influence of the longitudinal distance between the tip and the molecule is studied, which is of specific interest for TERS experiments because the tip-sample distance is a crucial parameter that determines signal enhancement.

3.3.1 Computational details

The Ag tip is positioned at several points according to a grid of 6.5×5.5 Å with step size of 0.5 Å on top of the adenine, defined as the xy-plane (see Fig. 3.8), at different heights of 10, 8, 6, 5, 4, 3 and 2.5 Å, defined as the z-distance. The Ag tip was represented in form of two different models: a) one Ag atom and b) Ag_{20} cluster. The Raman spectra were evaluated using Gaussian 09[111] at the DFT level[67] of theory using the CAM-B3LYP XC functional.[80] As basis sets, 6-311G+(d,p)[133] was used for the description of the adenine molecule and the quasi-relativistic effective core potential MWB28[88] for the description of the silver tip (in both models). Because of the TERS set up, the adenine molecule is anchored parallel to a surface (xy-plane), the TERS signal is mainly obtained in the z-direction. Therefore the intensity can be evaluated as:

$$I_l \propto \left| \frac{\partial (\alpha_{zz})_l}{\partial q_l} \right|^2 \tag{3.1}$$

To evaluate how the Raman signal is amplified at a given z-distance and at a specific grid point, the signal amplification, A, is introduced as:

$$A = \frac{I}{I_{min}} = \sum_{l=8}^{37} \frac{\left| \frac{\partial \alpha_{zz}}{\partial q_l} \right|^2}{\left| \frac{\partial \alpha_{min,zz}}{\partial q_l} \right|^2} \tag{3.2}$$

where the sum is over all the normal modes within the studied frequency range and I_{min} is the Raman intensity for the layer at a greater z-distance value (at 10 Å) taken as a reference. Moreover, the signal amplification calculated for a specific normal mode l, A_l, is defined as:

$$A_l = \frac{I_l}{I_{l,min}} = \sum_{l=8}^{37} \frac{\left| \frac{\partial \alpha_{zz}}{\partial q_l} \right|^2}{\left| \frac{\alpha_{min,zz}}{\partial q_l} \right|^2} \tag{3.3}$$

where the specific intensity at the normal mode l, I_l, is normalized by means of $I_{l,min}$. The first, A, is the integrated signal intensity within the selected frequency range, from 500 to 1700 cm^{-1} [126,127,134], and normalized with respect to the minimum intensity at z = 10 Å; while the latter, A_l, evaluates the amplification of the Raman signal for a given normal mode with respect to the same mode at $z = 10$ Å. All frequencies have been scaled by a factor of 0.95 (to account for a systematic error in the DFT predictions and to correct for the lack of anharmonicity)[118] and peaks were convoluted by Lorentzians of 15 cm^{-1} full width at half maximum (FWHM) to account for line broadening in possible future experimental spectra.
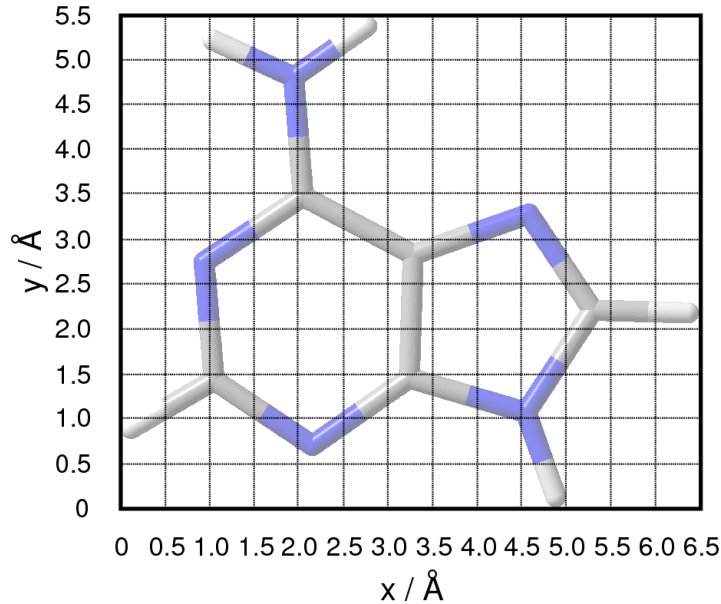

Figure 3.8: Adenine orientation and computational grid of 6.5 Å times 5.5 Å and with a step size of 0.5 Å as used in the quantum chemical simulations.

3.3.2 One atom model

Firstly, the behavior of the intensity as a function of the metal-molecule position is discussed. At $z = 10$ Å the TERS spectra resembles the z-polarized Raman spectrum of the adenine at any point of the grid. At medium z-distances, between 8 and 6 Å, there are no critical alternations on the Raman pattern. Nevertheless, at closer z-distances, the appearance of the Raman spectrum becomes drastically affected by the position of the tip. This phenomenon starts at 4 Å (see Fig. 3.9 a), where the spectra for the Ag located in the center of the pyrimidine ring (blue) and in the imidazole moiety (red) at $z = 4$ Å are showed) and escalates exponentially towards smaller z-distances, where the silver tip induces slight shifts of the vibrational frequencies, as well as alterations of intensity ratios, leading to unique spectral patterns with respect to the specific lateral position of the silver atom. This drastic change of the Raman signal behavior at closer z-distances is directly related with the interaction between the silver tip and the adenine.

Moreover, the dependency in the longitudinal z-coordinate was evaluated. The general behavior of the intensity as a function of the metal-molecule distance is illustrated in Fig.3.9 b) and d) for the center of the pyrimidine and the imidazole moiety at $z = 10.0$, 6.0, 4.0, 3.0, and 2.5 Å, respectively, while A_l are presented in Fig.3.9 c) and e). At 10.0 Å, the spectra in the center of the pyrimidine ring and imidazole moiety are identical and dominated by intense C-H and N-H bending modes. Alterations are induced by the silver atom at 4 Å, while at 3 Å, the spectrum in the center of the pyrimidine ring is dominated by three intense CH/NH bending modes at 1490, 1390 and 980 cm^{-1}. In the imidazole moiety, the Raman intensity pattern features two intense modes at 1490 and 880 cm^{-1} (CH/NH bending), both at higher absolute intensities compared to the center of the pyrimidine ring. Moving the tip closer to z $= 2.5$ Å, substantially alters the intensity pattern in the center of the pyrimidine ring. Now, the intense CH bending mode (880 cm^{-1}) is shifted by 12 cm^{-1} to lower frequencies, and an intense skeleton mode at 520 cm^{-1} emerges.

Furthermore, the Raman amplification, A, shows an exponential increase towards closer z-distances (see Fig.3.11 a)). Fig.3.10 a) and b) show maps of the calculated A at each grid point for z-distances at 4 and 2.5 Å. For the Ag atom model, the highest values of A are obtained at the C-H bond of the pyrimidine ring amounting to 10.6 and 631.8 at 4 and 2.5 Å respectively. Also at the C-H bond on the imidazole moiety high values of 17.9 and 553.2 at 4 and 2.5 Å respectively can be observed. Analogously, the bending normal modes (in plane) related to these bonds, the C-H bending mode of the pyrimidine ring (975-980 cm^{-1}) and the C-H bending mode of the imidazole moiety (870-875 cm^{-1}), show the highest values of A_l (see Fig.3.9 c) and e)).
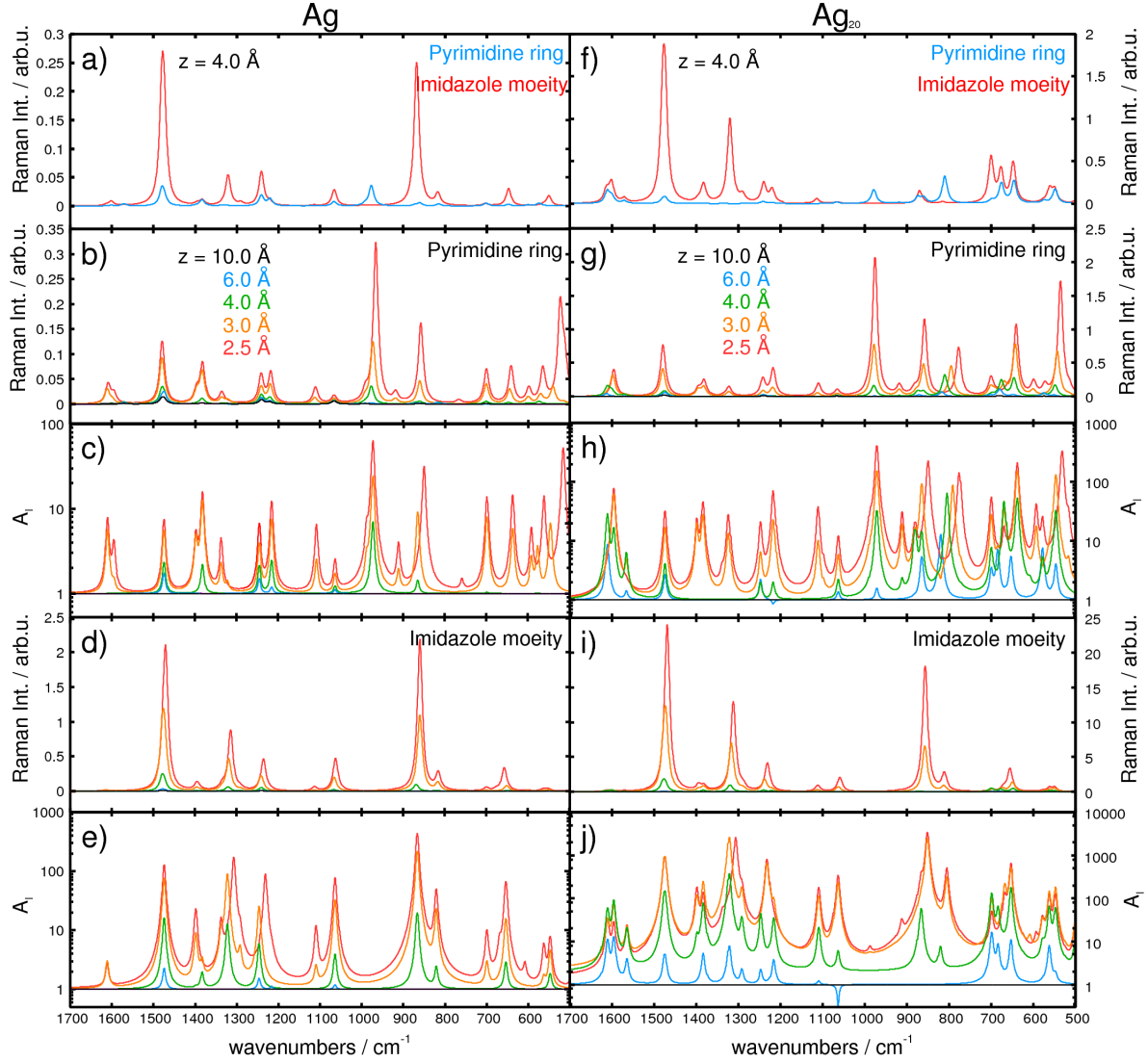
Figure 3.9: Simulated Raman spectra based on the one-silver-atom model for a) at the center of the pyrimidine ring and at the imidazole moiety. The z-dependency is shown for the center of the pyrimidine ring and the imidazole moiety, for $z=$ 10.0, 6.0, 4.0, 3.0, and 2.5 Å, in arb. u. in b) and d) and in mode amplification in, c) and e), respectively. Respective Raman spectra based on the silver-cluster model are shown in f) the silver tip is located at the pyrimidine ring and at the imidazole moiety, g) and i) illustrate the z-dependency in at the pyrimidine ring and the imidazole moiety (Raman Intensity in arb. u.). Mode amplifications in the pyrimidine ring and the imidazole moiety are shown in h) and j). Vibrational normal modes were broadened by Lorentzians with a FWHM of 15 cm^{-1}. Note the different scales for both models.

To unravel the nature of the chemical interaction of the system adenine-Ag, the potential energy surface (PES) and frontier orbitals need to be studied. A z-scan (see Fig. 3.11 b)), on top of the center of the pyrimidine ring, features attractive interactions of the silver atom and the adenine in the range from 6 to 3 Å, while the minimum is ap-
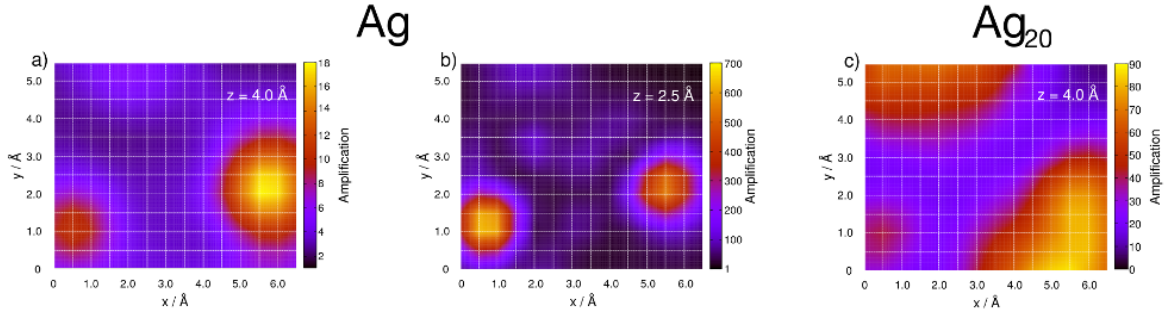
Figure 3.10: Simulated Raman signal amplification, A, along the grid at a) $z = 4$ Å, b) 2.5 Å for the Ag atom model and c) 4 Å for the Ag_{20} model.

proximated at 3.62 Å. At longer distances, the attractive interactions decay, hence, the ground state energy rises towards the threshold of 0.06 eV. This trend is in agreement with the evolution of the amplification factors in the interval between 6 and 10 Å from 1.6 to 1.0. At small distances ($z < 3$ Å) the PES is dominated by repulsive interactions and the amplification rises exponentially.
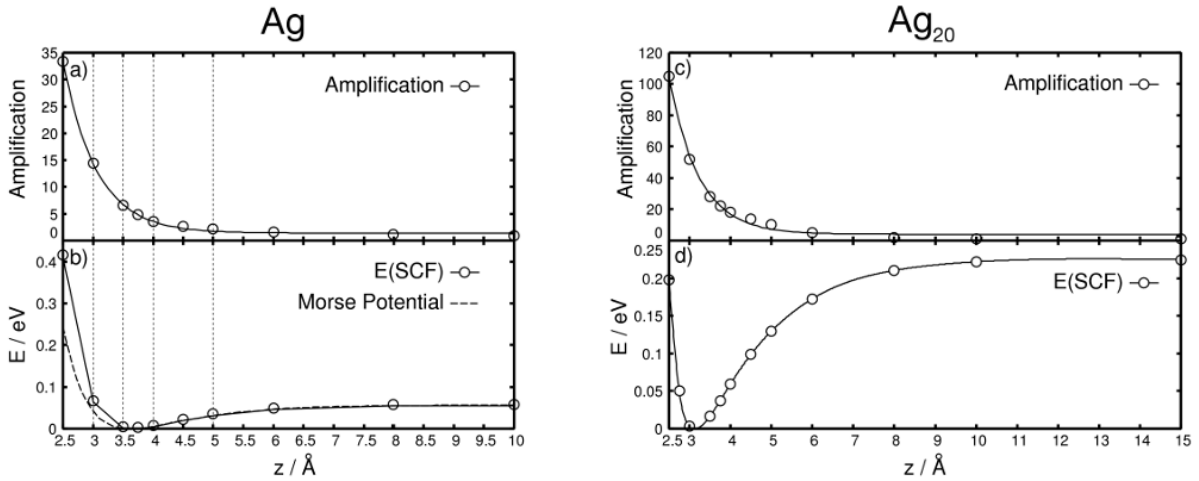
Figure 3.11: a) Intensity amplification (black circle) and exponential fit (black line) and b) cut of the potential energy surface of the doublet ground state (solid line/circle) along z using the Ag atom model as well as Morse potential (dashed line) in the center of the pyrimidine ring; c)Intensity amplification (black circle) and exponential fit (black line) and d) cut of the potential energy surface of the double ground state (solid line/circle) along z using the Ag_{20} model as well as Morse potential (dashed line) in the center of the pyrimidine ring

These interactions can be better visualized by meanings of the frontier orbitals. At $z = 10$ Å the frontier orbitals are almost degenerated, however, with the tip converging towards the adenine this degeneration becomes abrogated. The interaction of the Ag $5s$ orbital with the adenine π-system highly depends on the silver atom position and, eventually, on the presence of a nodal plane between the silver and the adenine. For positions

46

in the periphery of the molecule only small interactions are observed. The orbital interactions in the center of the purine fragment are more complicated, and constructive as well as destructive interactions are found. However, on top of the imidazole ring a clear constructive overlap is given. Lowering the silver atom further towards the adenine consequently enhances the constructive and destructive orbital interactions. The spherical shape of the s-orbital leads to a manifold of delocalized interactions with the π-orbital, especially in the center of the pyrimidine and the imidazole rings. Hence, in these regions a bonding situation is unfavored.

3.3.3 Ag$_{20}$ cluster model

The second model, the Ag$_{20}$ cluster, includes the possibility to evaluate the chemical effect of the silver atoms in the second, third and fourth layers of the tip on the TERS signal. Due to the computational resources that this model needs, only some critical points have been calculated.

The obtained amplification with respect to z for this model (Fig.3.10 c)) shows a similar behavior with the former model (Fig.3.10 a)). However, A is even larger with the Ag$_{20}$ model. In the center of the pyrimidine ring values of A are 5.1, 18.1 and 105.1 at 6, 4 and 2.5 Å, respectively. In the C-H bond of the imidazole ring the amplifications are even higher: 7.7, 63.8 and 747 (at 6, 4 and 2.5 Å). The amplification factor of these two positions are in accordance with the results obtained for the one silver-atom model. Nevertheless, while in the Ag atom model the highest values of A are located at the C-H bond of the pyrimidine ring and the C-H bond of the imidazole moiety, in the Ag$_{20}$ model are mainly located between the C-H and N-H bonds of the imidazole moiety and the amino group. Furthermore, as in the Ag atom model, the normal modes related to these bonds show the highest values for the A_l. Interestingly, the potential minimum and thus the bonding region of the cluster and the adenine is offset from 3.62 to 3.14 Å, while the bonding energy increased from 0.06 to 0.22 eV (see Fig.3.11 d)).

The impact of the tip model size on the out-of-pane modes can be explained by looking at the tip charge and its variation with the z-distance. In both models, the tip features the same total charge (-0.1 Mulliken charge), independently of the grid point. However, in the Ag$_{20}$ cluster, the four vertex positions hold pronounced negative charges. At z = 10 Å, all four vertices have the same charge, whereas at shorter z-distance, the charges on the vertices become different, where the vertex oriented towards the adenine is more negatively charged. Hence, this charge gradient on the vertices along z induces distinct chemical effects that mainly affect the out-of-plane modes.

47

3.3.4 Conclusions

In this section of results, DFT calculations were presented on the adenine-silver tip system to investigate the properties of the lateral resolution on TERS. For this purpose, three-dimensional grid calculations were performed and the silver tip was simulated using two different models, Ag atom and Ag_{20} tetrahedron cluster. Both computational models suggest a hypothetical TERS resolution in the Ångström regime. Also, pronounced dependencies of the simulated Raman patterns and intensities on the tip model and its position were found. Furthermore, high mode amplifications were computed based on the chemical interactions between the adenine and the silver tip. It is important to note that only the molecular properties of the silver-adenine system were accounted for and not the external fields, particularly the field confinement due to plasmonic effects.

Chapter 4

Appended Publications

4.1 Resonance Raman spectra of ortho-nitrophenol calculated by real-time time-dependent density functional theory

Reprinted from Thomas et al. *J. Chem. Phys.* **138**, 044101 (2013), with the permission of AIP Publishing.

Resonance Raman spectra of *ortho*-nitrophenol calculated by real-time time-dependent density functional theory

Martin Thomas,[1,2] Federico Latorre,[1,2] and Philipp Marquetand[2,a)]
[1]*Institute of Physical Chemistry, Friedrich-Schiller-University Jena, Helmholtzweg 4, 07743 Jena, Germany*
[2]*Institute of Theoretical Chemistry, University of Vienna, Währinger Str. 17, 1090 Vienna, Austria*

A new approach for the calculation of resonance Raman spectra is presented. The new method is based on dynamic polarizabilities from real-time time-dependent density functional theory, and its estimations are compared to two established techniques for the prediction of resonance Raman spectra. These established methods either use dynamic polarizabilities from linear-response time-dependent density functional theory or employ excited-state gradients. The three different ways to calculate resonance Raman spectra are investigated using the example of *ortho*-nitrophenol. The three methods give very similar results, respectively, for the four different exchange-correlation functionals applied. Thus, the new approach is validated for the calculation of resonance Raman intensities and advantages as well as disadvantages are discussed. © *2013 American Institute of Physics.*
[http://dx.doi.org/10.1063/1.4776218]

I. INTRODUCTION

Resonance Raman spectroscopy is an important tool in modern analytical chemistry.[1] In this method, molecules are irradiated with frequencies near electronic transitions to increase the normal Raman scattering intensity by several orders of magnitude. This does not only enhance the sensitivity of Raman spectroscopy, but it also provides better selectivity because only normal modes strongly coupled to the electronic transition are intensifie in the spectrum. This leads to an interesting method for studying the nature of electronic excited states as it has been shown, e.g., for a ruthenium-palladium photocatalyst complex.[2–4]

Several different approaches have been established to calculate resonance Raman scattering intensities. Most of them are based either on the vibronic theory of Albrecht and co-workers[5–7] or on the time-dependent formalism of Heller and co-workers.[8–11] The vibronic theory applies the Born-Oppenheimer approximation to the general formalism of Kramers, Heisenberg and Dirac[12,13] to separate electronic and vibrational states, and it expands the transition dipole moments in a Taylor series in the nuclear coordinates. The resonance Raman intensity is then given by a sum of several terms, which describe the Franck-Condon scattering and the Herzberg-Teller scattering. All these terms consist of sums over intermediate vibrational levels and therefore this method is computationally very demanding for large molecules with many normal modes. For that reason, the transform theory[14] has been developed; it is based on a Kramers-Kronig transform of the absorption spectrum to avoid the large summations. This formulation has been adopted by Guthmuller and co-workers[15] where the intensities are finall based on excited-state gradients. It has successfully been applied to different molecules, including julolidinemalononitrile,[15] rho-

damine 6G,[16] several ruthenium complexes,[4,17] and *ortho*-nitrophenol (oNP).[18] The time-dependent formalism of Heller redefine the expression of Kramers, Heisenberg, and Dirac in time domain and the results are based on wave packet dynamics. If only short-time dynamics is considered, the relative intensities are given by excited-state gradients. The results of both approaches have been compared by Kane and Jensen using the examples of uracil, rhodamine 6G, and an iron complex.[19] Other formulations based on the vibronic theory have recently been described by Rappoport *et al.*[20] and Santoro *et al.*[21]

A basically different approach was taken by Jensen and Schatz.[22] Their method is similar to Placzek's polarizability theory, which nowadays is available in many quantum chemical software packages for the calculation of non-resonant Raman spectra. It is based on geometrical derivatives of the dynamic polarizability for the calculation of resonance Raman intensities. The dynamic polarizability is calculated in the framework of time-dependent density functional theory (TDDFT) using linear response theory. Explicitly including the finit lifetime of excited states allows to get the dynamic polarizability also for resonant frequencies,[23] which is a prerequisite for describing resonance Raman scattering. Chen *et al.*[24] recently used real-time time-dependent density functional theory (RT-TDDFT) to calculate dynamic polarizabilities. This method avoids solving the linear-response equations, which is advantageous for larger molecules. Furthermore, it is able to give the dynamic polarizability for resonant frequencies and should therefore be able to describe resonance Raman scattering. However, the latter point has not been tested until now. Therefore, we take the general approach of Chen *et al.*[24] and apply it to the calculation of resonance Raman spectra.

In the following, resonance Raman spectra of oNP are presented that are based on dynamic polarizabilities from RT-TDDFT calculations (named real-time method below). This

---

a)Electronic mail: philipp.marquetand@univie.ac.at.

molecule has recently been studied by Guthmuller[18] using the vibronic theory within the short-time approximation (named excited-state gradient method below), which allows to compare the spectra obtained using these two different ways for the calculation of resonance Raman intensities. Furthermore, the dynamic polarizabilities were also calculated using the approach of Jensen and Schatz[22] (named polarizability method below) to test whether they are equal to the real-time method. Assets and drawbacks of all these methods are discussed.

II. THEORETICAL BACKGROUND

A. Real-time method

In the framework of density functional theory, dynamic polarizabilities can be calculated using the RT-TDDFT method as described by Chen $et\ al.$[24] Unlike in widely used TDDFT calculations within the linear response formalism, the RT-TDDFT approach requires to explicitly solve the time-dependent Kohn-Sham equations:

$$\left(-\frac{\hbar^2}{2m_e}\nabla^2 + v(\mathbf{r}, t) + \frac{e^2}{4\pi\varepsilon_0} \int \frac{\rho(\mathbf{r}', t)}{|\mathbf{r} - \mathbf{r}'|}\,\mathrm{d}\mathbf{r}' \right.$$
$$\left. + v_{\mathrm{xc}}(\mathbf{r}, t) \right)\phi_i(\mathbf{r}, t) = i\hbar\frac{\partial}{\partial t}\phi_i(\mathbf{r}, t), \quad (1)$$

where the ϕ_i denote the Kohn-Sham orbitals. The operator on the left side consists of the kinetic energy, the external potential, the classical Coulomb interaction, and the exchange-correlation potential. Unfortunately, the exact form of the exchange-correlation potential is unknown and therefore approximations have to be made. The external potential contains the interaction of the electrons with the nuclei and the external electric field It is therefore possible to include an arbitrary time-dependent electric field The time-dependent Kohn-Sham equations are usually solved by numerical integration, e.g., by the enforced time reversible symmetry algorithm.[25]

Solving the time-dependent Kohn-Sham equations delivers the evolution of the electron density over time, which can be used to calculate the time-dependent dipole moment. In frequency domain, the induced dipole moment P is connected to the applied electric fiel E by the polarizability tensor α according to

$$P_j(\omega) = \sum_i \alpha_{ij}(\omega)E_i(\omega), \quad (2)$$

where i and j run over the three independent directions of space. Using this definition the polarizability is calculated by

$$\alpha_{ij}(\omega) = \frac{P_j(\omega)}{E_i(\omega)} = \frac{\int P_j(t)e^{i\omega t}e^{-\Gamma t}\,\mathrm{d}t}{\int E_i(t)e^{i\omega t}\,\mathrm{d}t}, \quad (3)$$

where a Fourier transform is applied to convert from frequency domain to time domain. The exponential damping factor was introduced to account for the finit lifetime of excited states. Effectively, it retards the displacement of the electron density due to the external electric field Without this damping, the integration would diverge at the resonance frequencies and the polarizability could only be calculated for non-resonant frequencies.

The absorption cross section of an isolated molecule with random orientation is provided by[26]

$$\sigma = \frac{\omega}{\varepsilon_0 c}\,\mathrm{Im}\left(\frac{1}{3}\left(\alpha_{xx} + \alpha_{yy} + \alpha_{zz} \right) \right), \quad (4)$$

where ε_0 is the vacuum permittivity and c is the speed of light.

The differential Raman scattering cross section for a normal mode p is given by[27]

$$\frac{\mathrm{d}\sigma}{\mathrm{d}\Omega} = \frac{\pi^2}{\varepsilon_0^2}(\tilde{\nu}_{\mathrm{in}} - \tilde{\nu}_p)^4 \frac{h}{8\pi^2 c\tilde{\nu}_p}\frac{45|a_p|^2 + 7\gamma_p^2}{45}$$
$$\times \frac{1}{1 - \exp\left(-\frac{hc\tilde{\nu}_p}{k_{\mathrm{B}}T} \right)}, \quad (5)$$

where $\tilde{\nu}_{\mathrm{in}}$ is the wavenumber of the incident light, $\tilde{\nu}_p$ is the wavenumber of normal mode p, h is Planck's constant, k_B is the Boltzmann constant, T is the temperature (set to 298 K), a_p is the isotropic polarizability derivative:

$$a_p = \frac{1}{3}\left(\frac{\partial\alpha_{xx}}{\partial p} + \frac{\partial\alpha_{yy}}{\partial p} + \frac{\partial\alpha_{zz}}{\partial p} \right), \quad (6)$$

and γ_p is the anisotropic polarizability derivative:

$$\gamma_p^2 = \frac{1}{2}\left(\left| \frac{\partial\alpha_{xx}}{\partial p} - \frac{\partial\alpha_{yy}}{\partial p} \right|^2 + \left| \frac{\partial\alpha_{yy}}{\partial p} - \frac{\partial\alpha_{zz}}{\partial p} \right|^2 + \left| \frac{\partial\alpha_{zz}}{\partial p} - \frac{\partial\alpha_{xx}}{\partial p} \right|^2 \right.$$
$$\left. + 6\left(\left| \frac{\partial\alpha_{xy}}{\partial p} \right|^2 + \left| \frac{\partial\alpha_{yz}}{\partial p} \right|^2 + \left| \frac{\partial\alpha_{zx}}{\partial p} \right|^2 \right) \right). \quad (7)$$

B. Polarizability method

The resonance Raman intensities evaluated with the polarizability method have been obtained using the AORESPONSE module[22,23,28] (which calculates the response of the atomic orbitals to an external field of the ADF program package.[29,30] In this module we have specifie a damping parameter of 0.1 eV (0.00367493 a.u.), which describes the lifetime of the excited state.

C. Excited-state gradient method

In the short-time approximation (STA),[8] the expression for the relative intensities of the fundamental transition $0 \rightarrow 1_p$ is given by

$$I_{0\rightarrow 1_p} \propto \frac{1}{\omega_p}\left(\frac{\partial E^e}{\partial p} \right)_0^2, \quad (8)$$

where ω_p is the frequency of the normal mode p and $(\partial E^e/\partial p)_0$ is the partial derivative of the excited state electronic energy along that normal mode at the ground state equilibrium position. In this formulation, the normal modes are nonmass-weighted.[18]

III. COMPUTATIONAL DETAILS

A. Real-time method

All DFT calculations for the real-time method were carried out using the CP2K program package.[31] The Goedecker-Teter-Hutter pseudopotentials[32] were applied together with the corresponding polarized valence-double-zeta (DZVP) basis sets.[31] All calculations were performed with four different exchange-correlation functionals: the gradient-corrected PBE functional[33] and its corresponding hybrid version PBE0,[34] as well as the gradient-corrected BLYP functional[35,36] and its three-parameter hybrid version B3LYP.[37,38] A wavelet Poisson solver[39] was used for the electrostatic interactions under non-periodic boundary conditions.

First, the geometry was optimized and a vibrational analysis was carried out. The molecular geometry was then displaced along each of the normal modes and three separate RT-TDDFT trajectories were started for each of the displaced geometries. The trajectories were run for 3500 steps with a time step of 0.6 a.u. During the firs step, an electric fiel of 5.338 $\times 10^{-5}$ a.u. was applied where the three independent directions of space were covered by the three separate trajectories for every geometry. The dipole moment was recorded for the whole trajectories and it was used to calculate the polarizabilities according to Eq. (3), where a damping factor of 0.1 eV was chosen. The damping factor essentially determines the width of the peak features in the polarizability curve. Higher damping leads to broader peaks and by this means reduces the maximum values at the resonance frequencies. Therefore, the predicted absolute scattering cross sections depend on it and the same values should be used for the real-time method and the polarizability method.

The polarizability derivatives needed for the Raman scattering cross sections were obtained numerically from finit differences with a displacement of 0.02 Å along the Cartesian normal mode vectors. Single-sided differentiation was used to save computational resources since numerical errors in comparison to two-sided differentiation were found to be negligible in several test cases.

B. Polarizability method

In the polarizability method, the quantum chemical properties and the resonance Raman intensities were determined by using the ADF program package.[29,30] The ground state properties were obtained at the DFT level of theory using the PBE[33] and BLYP[35,36] exchange-correlation functionals with the double-zeta polarized Slater-type (DZP) basis set. The excited state properties and resonance Raman intensities have been obtained with TDDFT using the same functionals and basis set. The hybrid functionals PBE0 and B3LYP could not be used with this method due to the implementation limits of ADF.

C. Excited-state gradient method

In the STA, the quantum chemical calculations were carried out using the GAUSSIAN 09[40] program. The geometries and frequencies of vibrations in the ground state were calculated at the DFT level of theory using PBE,[33] BLYP,[35,36] PBE0,[34] and B3LYP[37,38] exchange-correlation functionals with the 6-31G** basis set. The excited state properties were obtained at the TDDFT level of theory using the same functionals and basis set. The resonance Raman intensities were evaluated as detailed in Ref. 18.

IV. RESULTS AND DISCUSSION

First, the vibrational frequencies obtained with the three different methods are analyzed to compare the applied basis sets. In principle, these are on the same level of quality because they are all of double-zeta type in the valence shell and contain one p-type polarization function for hydrogen and one d-type polarization function for the second-row elements. Nevertheless, the polarizability method relies on Slater-type functions whereas the other two methods use Gaussian-type functions so that minor differences have to be expected. In addition, the real-time method applies pseudopotentials to model the core electrons, but since vibrational frequencies and polarizabilities are rarely influence by the core electronic configuration this is not an issue.

The vibrational frequencies of in-plane normal modes in the 200–1700 cm^{-1} wavenumber range are presented in Table I for the four different exchange-correlation functionals that were used. None of the out-of-plane normal modes shows a significan resonance Raman intensity and therefore they are omitted here. To account for the anharmonicity

TABLE I. Comparison of vibrational frequencies in cm^{-1} (frequencies scaled by 0.96 for PBE0 functional and by 0.97 for B3LYP functional, RT—real-time method, PO—polarizability method, and EG—excited-state gradient method).

No.	PBE			PBE0		BLYP			B3LYP	
	RT	PO	EG	RT	EG	RT	PO	EG	RT	EG
ν_6	1632	1629	1638	1648	1659	1600	1604	1610	1619	1634
ν_7	1595	1600	1598	1597	1597	1571	1580	1578	1581	1588
ν_8	1546	1544	1562	1589	1603	1508	1516	1525	1543	1569
ν_9	1472	1479	1489	1477	1492	1458	1470	1475	1465	1483
ν_{10}	1453	1450	1465	1449	1464	1418	1416	1436	1445	1462
ν_{11}	1427	1420	1422	1403	1403	1394	1396	1399	1385	1392
ν_{12}	1343	1353	1357	1344	1355	1333	1329	1340	1333	1344
ν_{13}	1304	1304	1315	1295	1308	1276	1277	1291	1287	1299
ν_{14}	1242	1233	1258	1276	1292	1218	1225	1227	1253	1272
ν_{15}	1196	1206	1209	1184	1200	1196	1187	1202	1204	1206
ν_{16}	1128	1155	1151	1126	1146	1148	1150	1154	1138	1153
ν_{17}	1117	1138	1135	1104	1127	1127	1132	1130	1125	1131
ν_{18}	1068	1084	1078	1066	1078	1055	1072	1068	1063	1077
ν_{19}	1021	1029	1026	1013	1022	1017	1022	1019	1017	1023
ν_{20}	839	861	852	842	856	838	854	847	843	854
ν_{21}	802	813	810	808	817	789	798	795	802	811
ν_{22}	654	670	664	651	662	653	667	660	655	664
ν_{23}	544	559	554	543	553	545	558	552	548	554
ν_{24}	528	544	538	527	537	526	540	535	531	538
ν_{25}	437	441	436	425	427	429	434	430	430	427
ν_{26}	366	384	373	360	369	362	378	371	366	371
ν_{27}	281	295	286	276	282	280	290	283	284	283

and the systematic error of the functionals, scaling factors of 0.96 and 0.97 were applied to the PBE0 frequencies and the B3LYP frequencies, respectively.[41,42] The numbering of the normal modes was adopted from previous analyses in the literature.[18,43,44] There, the assignment is based on theoretical calculations and experimental infrared, Raman and resonance Raman spectra. For the assignment used here, the calculated frequencies and the normal mode vectors were compared to the ones presented by Guthmuller,[18] which agree very well. Looking at one functional, respectively, the frequencies of the three methods are very similar, only in some cases there are differences of up to 25 cm^{-1}. These deviations have to be attributed to the different basis sets. Nevertheless, the differences within the functionals are much smaller than the differences between the functionals. In particular for the normal modes ν_8 and ν_{14}, the frequencies are distributed over a range of up to 95 cm^{-1} comparing PBE0 and BLYP. Considering all the above findings it is seen that there are minor deviations due to the differing basis sets, but the choice of the exchange-correlation functional provides a much larger influence. For that reason, the comparison of the three methods within the functionals is justifiable. In any case, larger basis sets would be required to fully recover the predictive power of the calculations in a comparison to experimental data,[45,46] but this is not within the aim of the present work. However, a short consideration of the basis set truncation effect will be given for two of the exchange-correlation functionals later on.

Next, we focus on the electronic energies for the resonant excitation during the resonance Raman process. The experimental absorption spectrum of oNP shows the first absorption band at 3.57 eV.[44] Within linear-response TDDFT, all four exchange-correlation functionals (PBE, PBE0, BLYP, and B3LYP) predict this absorption band as the first excited singlet state, characterized by an electron density transfer from the hydroxyl group and the aromatic ring to the nitro group.[18] However, the functionals differ in the excitation energy. In the excited-state gradient method calculations, the PBE functional predicts 2.99 eV, which is 0.58 eV below experiment, whereas the PBE0 functional predicts 3.74 eV which is only 0.17 eV above experiment, the BLYP functional predicts 2.90 eV, which is 0.67 eV below experiment, and the B3LYP functional predicts 3.53 eV, which is only 0.04 eV below experiment (spectra not shown). The excitation energies in the polarizability method calculations are very similar, 3.00 eV versus 2.93 eV with PBE or BLYP, respectively. The results coincide with Guthmuller's[18] conclusion that the amount of Hartree-Fock exchange in the exchange-correlation functional has a large influence on the estimated excitation energies. In the case of oNP, the hybrid functionals PBE0 and B3LYP perform definitely better than PBE and BLYP. Within the framework of RT-TDDFT, the absorption spectrum is calculated by a Fourier transform of the dipole moment during the propagations. For that reason, no individual states are obtained in the real-time method, instead the whole spectrum is calculated at once. As a minor drawback, it is therefore hard to characterize the individual transitions. Nevertheless, the overall shapes of the absorption spectra obtained using the two different approaches are in good agreement.
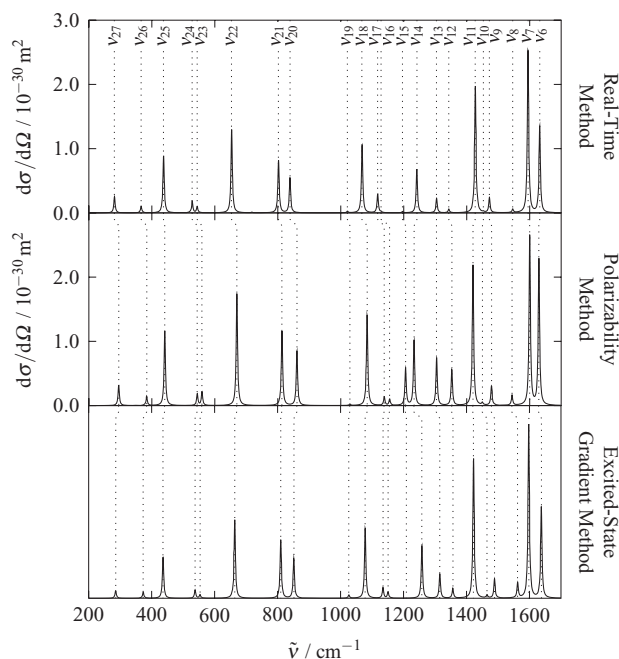

FIG. 1. Comparison of resonance Raman spectra with PBE functional (peaks broadened by Lorentzian functions with a FWHM of 5 cm^{-1}).

Finally, the resonance Raman spectra are discussed. For every calculation, the excitation wavelength for the resonance Raman process was adjusted to the center of the first absorption band for the respective method and functional as discussed in the last paragraph. The resonance Raman spectra calculated using the PBE functional are shown in Figure 1. The spectra for the three different methods agree very well. In all of them, the most intensive peak is connected to the vibration ν_7 and further important peaks belong to the normal modes ν_6, ν_{11}, ν_{18}, and ν_{22}. Noteworthy differences between the methods appear for the intensities of ν_6, ν_{12}, ν_{13}, and ν_{15}. Here, the polarizability method yields higher peaks than the other two approaches. These differences can be attributed to the fact that the polarizability method uses a Slater basis set whereas the other two methods use Gaussian basis sets. The general features of the spectrum are however not influenced and one can conclude that all three methods give a comparable resonance Raman spectrum with the PBE functional. Since the real-time method and the polarizability method are based on the same idea, they should give equal absolute scattering cross sections as long as the same damping factor is used. Also this is nicely fulfilled in the spectra calculated here (see Figure 1).

The resonance Raman spectra calculated using the PBE0 functional are presented in Figure 2. Although it was not possible to use the polarizability method here, the remaining two methods are again in good agreement. The most intensive peak belongs to ν_{11} and further important normal modes are ν_6, ν_7, ν_{13}, and ν_{22}. A noteworthy difference between the two spectra arises for the intensity ratio of ν_{13} and ν_{14}. With the real-time method, ν_{14} shows significant intensity whereas it is negligible with the excited-state gradient method, where ν_{13} in turn is more intensive. This deviation can be attributed
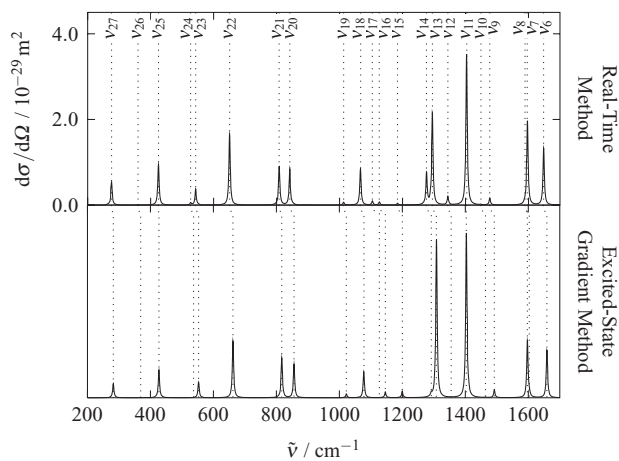
FIG. 2. Comparison of resonance Raman spectra with PBE0 functional (peaks broadened by Lorentzian functions with a FWHM of 5 cm^{-1}).
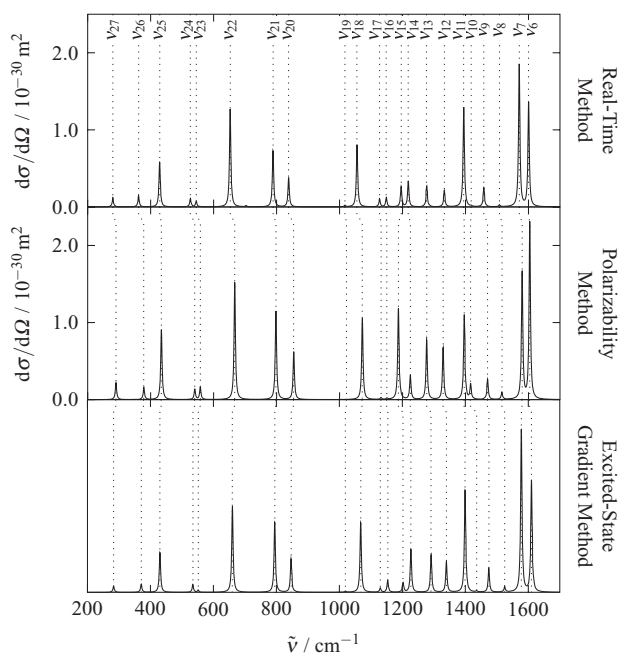

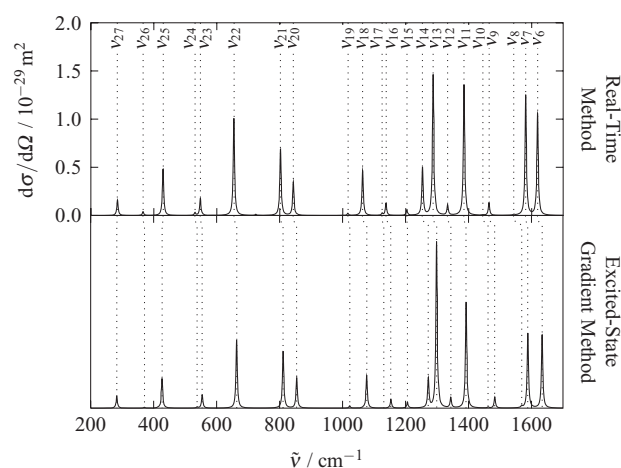FIG. 4. Comparison of resonance Raman spectra with B3LYP functional (peaks broadened by Lorentzian functions with a FWHM of 5 cm^{-1}).

to a slight mixing of the corresponding normal modes that is caused by the differing basis sets. Potentially, the actual nuclear displacement that is responsible for the high resonance Raman intensity is distributed to both normal modes in the real-time method, but it is confine   to ν_{13} in the excited-state gradient method.

In Figure 3, the resonance Raman spectra obtained using the BLYP functional are shown. Similar to the PBE spectra, the general agreement between the methods is very good in particular for the real-time method and the excited-state gradient method. Comparing the polarizability method to the other two methods, there are again noteworthy differences in the intensities of ν_6, ν_{12}, ν_{13}, and ν_{15}. These are the same four normal modes as with PBE and the deviations can again be attributed to the fact that the polarizability method uses a Slater

FIG. 3. Comparison of resonance Raman spectra with BLYP functional (peaks broadened by Lorentzian functions with a FWHM of 5 cm^{-1}).

basis set instead of Gaussian basis sets as the other two methods. Due to these differences, ν_6 is the most intensive normal mode with the polarizability method, whereas ν_7 shows the largest intensity in the other two spectra. Nevertheless, the general features remain the same for all three methods. Also the absolute scattering cross sections given by the real-time method and the polarizability method are in very good agreement.

As shown in Figure 4, similar conclusions can be drawn for the B3LYP functional. Although the polarizability method was not available, the remaining two spectra agree very well. The most intensive peak is connected to ν_{13} and other important normal modes are ν_6, ν_7, ν_{11}, and ν_{22}. A similar effect as with PBE0 is observed for ν_{13} and ν_{14} though it is less pronounced here. Again it can be attributed to a slight mixing of the normal modes.

A comparison of the results obtained within the exchange-correlation functionals reveals noticeable differences only for peaks above 1000 cm^{-1}. For the other peaks, ν_{20} up to ν_{27}, the intensity ratios are very similar. Important changes concern the most intensive normal mode, which is ν_7 for PBE, ν_6 or ν_7 for BLYP, ν_{11} for PBE0, and ν_{13} for B3LYP. The intensity of ν_{13} is much higher with the hybrid functionals PBE0 and B3LYP. These general disparities between the different exchange-correlation functionals are reproduced in the same manner by all the methods investigated here. This endorses that the real-time method, the polarizability method, and the excited-state gradient method produce in principle similar resonance Raman spectra despite the slight deviations caused by the differing basis sets and the use of pseudopotentials in the real-time method.

It has been stated several times now that the application of different basis sets is responsible for slight deviations in the resonance Raman spectra. To address the general influ ence of the basis set truncation, the calculations with the PBE and the PBE0 functional were repeated with a larger basis set. In particular, the addition of diffuse functions should be important here since electronically excited states are treated, so an augmented double-zeta basis set was chosen. For this
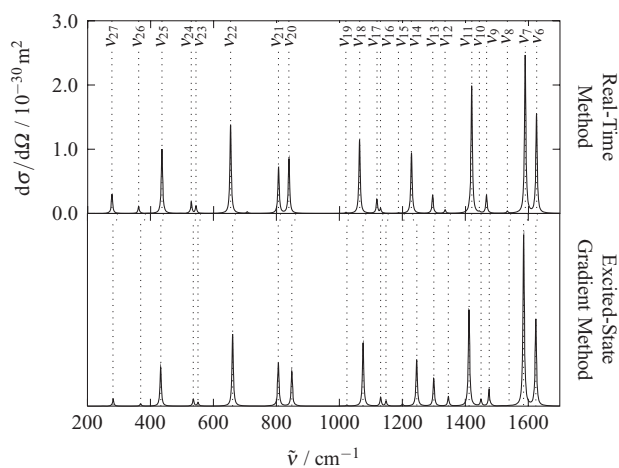
FIG. 5. Comparison of resonance Raman spectra with augmented basis set and PBE functional (peaks broadened by Lorentzian functions with a FWHM of 5 cm^{-1}).

purpose, the aug-DZVP basis set available in CP2K was used for the real-time method and the 6-31++G** basis set was taken from GAUSSIAN 09 for the excited-state gradient method. The corresponding resonance Raman spectra are shown in Figures 5 and 6. Comparing the PBE spectra with Figure 1, the results are very similar. The vibrational frequencies change in a range of less than 15 cm^{-1} and also the intensities deviate only slightly. In the real-time method, the most notable difference concerns ν_{20} and ν_{21}, which approximately swap their intensities. In the excited-state gradient method, the most important changes are the increasing intensity of ν_{11} and the emerging peak for ν_8. Similar facts are observed for the PBE0 spectra. Compared to Figure 2, the most notable difference in the real-time method concerns again ν_{20} and ν_{21}, which are of equal intensity with the DZVP basis set, whereas ν_{20} is more intensive with aug-DZVP. In the excited-state gradient method, the most important deviation is the partial intensity transfer from ν_{13} to ν_{14}. Summing up these findings the extension of the basis set by diffuse functions shows that the original double-zeta basis sets are sufficien for a quali-
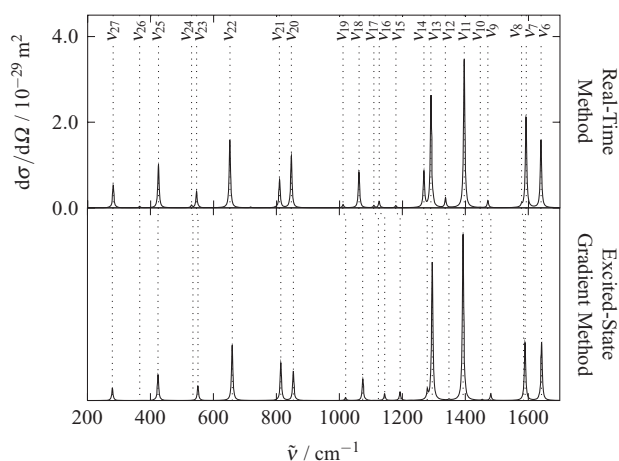

FIG. 6. Comparison of resonance Raman spectra with augmented basis set and PBE0 functional (peaks broadened by Lorentzian functions with a FWHM of 5 cm^{-1}).

tatively correct prediction of the resonance Raman spectrum. Nevertheless, there are slight changes, which probably would also arise when passing on to triple-zeta basis sets. However, the differences between the methods for the computation of resonance Raman spectra are reduced by using larger basis sets, so this investigation strongly supports the statement that the deviations between the methods can be attributed to the differing basis sets.

All approaches used here for the calculation of resonance Raman intensities consider only short-time dynamics. It is possible to extend the excited-state gradient method to include the vibronic structure of the excited state by explicitly considering vibrational levels via Franck-Condon factors,[15] where the potential energy surfaces are assumed to be displaced harmonic oscillators with identical normal modes and Duschinsky rotations are neglected. Guthmuller has shown that this is not important in the case of oNP.[18] The vibronic structure of the excited state cannot be treated within the real-time method because the nuclei are f xed in the RT-TDDFT simulations. No information about the excited-state potential energy surface is incorporated at all and details such as excited-state vibrational frequencies and Duschinsky rotations are not considered. Nevertheless, the real-time method provides the advantage that all electronic states are treated at once, whereas the excited-state gradients have to be calculated for every single state. This is not a problem for a simple molecule such as oNP, where only one excited state contributes to the resonance Raman scattering, but the real-time method can be advantageous for larger molecules where the contributions of many nearby electronic states have to be considered or the resonance Raman spectrum is needed for several different absorption bands, which have to be treated individually with the excited-stated gradient method. Furthermore, the real-time method delivers Raman scattering intensities for a wide range of excitation energies at once and also a non-resonant Raman spectrum can easily be extracted without further simulations. As another important fact, the real-time method gives absolute scattering cross sections, but these have to be treated carefully in the resonance case because they depend on the damping factor Γ chosen for the evaluation of Eq. (3).

The real-time method and the polarizability method are generally based on the same idea, but the way to calculate the polarizability is different. The polarizability method uses linear response theory, where the corresponding equations involve matrices over all virtual Kohn-Sham orbitals so that the calculation strongly depends on the basis set size. In the real-time method instead, the electron density is propagated in time domain and therefore only the occupied orbitals have to be considered in the time-dependent Kohn-Sham equations (1). In this case, the free evolution of the occupied orbitals intrinsically accounts for all electronic states described by the chosen basis set. Since the number of occupied orbitals is solely given by the number of electrons, the real-time method is expected to scale better with system size and basis set than the polarizability method.

Finally, we note that the real-time method can in principle be expanded to periodic systems by using the vector-potential formulation of the electric field[47] Otherwise, the representation of the electric fiel requires additional considerations.[48]

In fact, a real-time TDDFT approach has also been recently applied for the non-resonant Raman response in solids.[49]

V. CONCLUSION

A newly developed approach for the calculation of resonance Raman spectra is presented. It is based on dynamic polarizabilities as proposed by Jensen and Schatz[22] in analogy to Placzek's polarizability theory. However, the polarizabilities are not calculated in frequency domain using linear response theory, instead the RT-TDDFT method is used where the electron density is propagated in time domain as shown by Chen *et al.*[24] for the calculation of surface-enhanced Raman spectra. In order to test the method, oNP is used as a model system. The results of this new approach are found to be comparable to calculations of dynamic polarizabilities in frequency domain particularly with respect to the absolute scattering cross sections. Slight deviations in some individual intensity ratios are attributed to the differing basis sets used in the calculations here. The spectra are also compared to a vibronic theory within the short-time approximation where the resonance Raman intensities are estimated from excited-state gradients. Summarizing the results, all methods deliver very similar resonance Raman spectra and therefore it can be stated that the calculation of dynamic polarizabilities via RT-TDDFT provides a new alternative to estimate resonance Raman intensities.

We note further that the simulation of resonance Raman intensities via RT-TDDFT is very interesting with regard to the recent approach of Chen *et al.*[24] to describe surface-enhanced Raman scattering (SERS). They combine classical electrodynamics and quantum mechanics to model the electromagnetic enhancement mechanism where the RT-TDDFT method is used for the quantum-mechanical part. Another important contribution to SERS, the chemical enhancement mechanism, requires to describe the resonance of the excitation laser with a charge-transfer transition between molecule and metal surface. It is therefore important to note that it is in principle possible to describe the resonance Raman effect with the RT-TDDFT method so that both SERS enhancement mechanisms can be modeled within the same methodological framework.

ACKNOWLEDGMENTS

[1]D. Long, *The Raman Effect: A Unified Treatment of the Theory of Raman Scattering by Molecules* (Wiley, 2002).
[2]S. Tschierlei, M. Presselt, C. Kuhnt, A. Yartsev, T. Pascher, V. Sundström,
M. Karnahl, M. Schwalbe, B. Schäfer, S. Rau, M. Schmitt, B. Dietzek, and J. Popp, Chem. Eur. J. **15**, 7678 (2009).
[3]S. Tschierlei, M. Karnahl, M. Presselt, B. Dietzek, J. Guthmuller, L. González, M. Schmitt, S. Rau, and J. Popp, Angew. Chem. Int. Ed. **49**, 3981 (2010).
[4]J. Guthmuller and L. González, Phys. Chem. Chem. Phys. **12**, 14812 (2010).
[5]A. C. Albrecht, J. Chem. Phys. **34**, 1476 (1961).
[6]J. Tang and A. C. Albrecht, J. Chem. Phys. **49**, 1144 (1968).
[7]A. C. Albrecht and M. C. Hutley, J. Chem. Phys. **55**, 4438 (1971).
[8]E. J. Heller, R. Sundberg, and D. Tannor, J. Phys. Chem. **86**, 1822 (1982).
[9]S.-Y. Lee and E. J. Heller, J. Chem. Phys. **71**, 4777 (1979).
[10]D. J. Tannor and E. J. Heller, J. Chem. Phys. **77**, 202 (1982).
[11]E. J. Heller, Acc. Chem. Res. **14**, 368 (1981).
[12]H. Kramers and W. Heisenberg, Z. Phys. A: Hadrons Nucl. **31**, 681 (1925).
[13]P. A. M. Dirac, Proc. R. Soc. London, Ser. A **114**, 710 (1927).
[14]W. L. Peticolas and T. Rush, J. Comput. Chem. **16**, 1261 (1995).
[15]J. Guthmuller and B. Champagne, J. Chem. Phys. **127**, 164507 (2007).
[16]J. Guthmuller and B. Champagne, J. Phys. Chem. A **112**, 3215 (2008).
[17]J. Guthmuller, B. Champagne, C. Moucheron, and A. Kirsch De Mesmaeker, J. Phys. Chem. B **114**, 511 (2010).
[18]J. Guthmuller, J. Chem. Theory Comput. **7**, 1082 (2011).
[19]K. A. Kane and L. Jensen, J. Phys. Chem. C **114**, 5540 (2010).
[20]D. Rappoport, S. Shim, and A. Aspuru-Guzik, J. Phys. Chem. Lett. **2**, 1254 (2011).
[21]F. Santoro, C. Cappelli, and V. Barone, J. Chem. Theory Comput. **7**, 1824 (2011).
[22]L. Jensen, L. L. Zhao, J. Autschbach, and G. C. Schatz, J. Chem. Phys. **123**, 174110 (2005).
[23]L. Jensen, J. Autschbach, and G. C. Schatz, J. Chem. Phys. **122**, 224115 (2005).
[24]H. Chen, J. M. McMahon, M. A. Ratner, and G. C. Schatz, J. Phys. Chem. C **114**, 14384 (2010).
[25]A. Castro, M. A. L. Marques, and A. Rubio, J. Chem. Phys. **121**, 3425 (2004).
[26]A. Castro, H. Appel, M. Oliveira, C. A. Rozzi, X. Andrade, F. Lorenzen, M. A. L. Marques, E. K. U. Gross, and A. Rubio, Phys. Status Solidi B **243**, 2465 (2006).
[27]J. Neugebauer, M. Reiher, C. Kind, and B. A. Hess, J. Comput. Chem. **23**, 895 (2002).
[28]M. Krykunov, A. Banerjee, T. Ziegler, and J. Autschbach, J. Chem. Phys. **122**, 074105 (2005).
[29]G. te Velde, F. M. Bickelhaupt, E. J. Baerends, C. Fonseca Guerra, S. J. A. van Gisbergen, J. G. Snijders, and T. Ziegler, J. Comput. Chem. **22**, 931 (2001).
[30]E. J. Baerends, J. Autschbach, A. Bérces, F. M. Bickelhaupt, C. Bo, P. M. Boerrigter, L. Cavallo, D. P. Chong, L. Deng, R. M. Dickson, D. E. Ellis, M. van Faassen, L. Fan, T. H. Fischer, C. F. Guerra, S. J. A. van Gisbergen, J. A. Groeneveld, O. V. Gritsenko, M. Grüning, F. E. Harris, P. van den Hoek, C. R. Jacob, H. Jacobsen, L. Jensen, G. van Kessel, F. Kootstra, E. van Lenthe, D. A. McCormack, A. Michalak, J. Neugebauer, V. P. Osinga, S. Patchkovskii, P. H. T. Philipsen, D. Post, C. C. Pye, W. Ravenek, P. Ros, P. R. T. Schipper, G. Schreckenbach, J. G. Snijders, M. Solá, M. Swart, D. Swerhone, G. te Velde, P. Vernooijs, L. Versluis, L. Visscher, O. Visser, F. Wang, T. A. Wesolowski, E. van Wezenbeek, G. Wiesenekker, S. Wolff, T. Woo, A. Yakovlev, and T. Ziegler, Amsterdam density functional modeling suite, see http://www.scm.com.
[31]J. VandeVondele, M. Krack, F. Mohamed, M. Parrinello, T. Chassaing, and J. Hutter, Comput. Phys. Commun. **167**, 103 (2005).
[32]M. Krack, Theor. Chem. Acc. **114**, 145 (2005).
[33]J. P. Perdew, K. Burke, and M. Ernzerhof, Phys. Rev. Lett. **77**, 3865 (1996).
[34]C. Adamo and V. Barone, J. Chem. Phys. **110**, 6158 (1999).
[35]A. D. Becke, Phys. Rev. A **38**, 3098 (1988).
[36]C. Lee, W. Yang, and R. G. Parr, Phys. Rev. B **37**, 785 (1988).
[37]A. D. Becke, J. Chem. Phys. **98**, 5648 (1993).
[38]P. J. Stephens, F. J. Devlin, C. F. Chabalowski, and M. J. Frisch, J. Phys. Chem. **98**, 11623 (1994).
[39]L. Genovese, T. Deutsch, A. Neelov, S. Goedecker, and G. Beylkin, J. Chem. Phys. **125**, 074105 (2006).
[40]M. J. Frisch, G. W. Trucks, H. B. Schlegel, *et al.* GAUSSIAN 09, Revision a.1, Gaussian, Inc., Wallingford CT, 2009.
[41]Y. Tantirungrotechai, K. Phanasant, S. Roddecha, P. Surawatanawong, V. Sutthikhum, and J. Limtrakul, J. Mol. Struct.: THEOCHEM **760**, 189 (2006).

[42] J. P. Merrick, D. Moran, and L. Radom, J. Phys. Chem. A **111**, 11683 (2007).

[43] A. Kovacs, V. Izvekov, G. Keresztury, and G. Pongor, Chem. Phys. **238**, 231 (1998).

[44] Y.-Q. Wang, H.-G. Wang, S.-Q. Zhang, K.-M. Pei, X. Zheng, and D. L. Phillips, J. Chem. Phys. **125**, 214506 (2006).

[45] D. Rappoport, Chem. Phys. Chem. **12**, 3404 (2011).

[46] F. D. Vila, D. A. Strubbe, Y. Takimoto, X. Andrade, A. Rubio, S. G. Louie, and J. J. Rehr, J. Chem. Phys. **133**, 034111 (2010).

[47] G. F. Bertsch, J.-I. Iwata, A. Rubio, and K. Yabana, Phys. Rev. B **62**, 7998 (2000).

[48] M. Lazzeri and F. Mauri, Phys. Rev. Lett. **90**, 036401 (2003).

[49] R. Aggarwal, L. Farrar, S. Saikin, X. Andrade, A. Aspuru-Guzik, and D. Polla, Solid State Commun. **152**, 204 (2012).

4.2 A spectroscopic study of the cis/trans-isomers of penta-2,4-dienoic acid attached to gold nanoclusters

PCCP

Physical Chemistry Chemical Physics

www.rsc.org/pccp

$\hat{H}\psi = E\psi$

trans   cis

Raman   Raman

ROYAL SOCIETY
OF CHEMISTRY
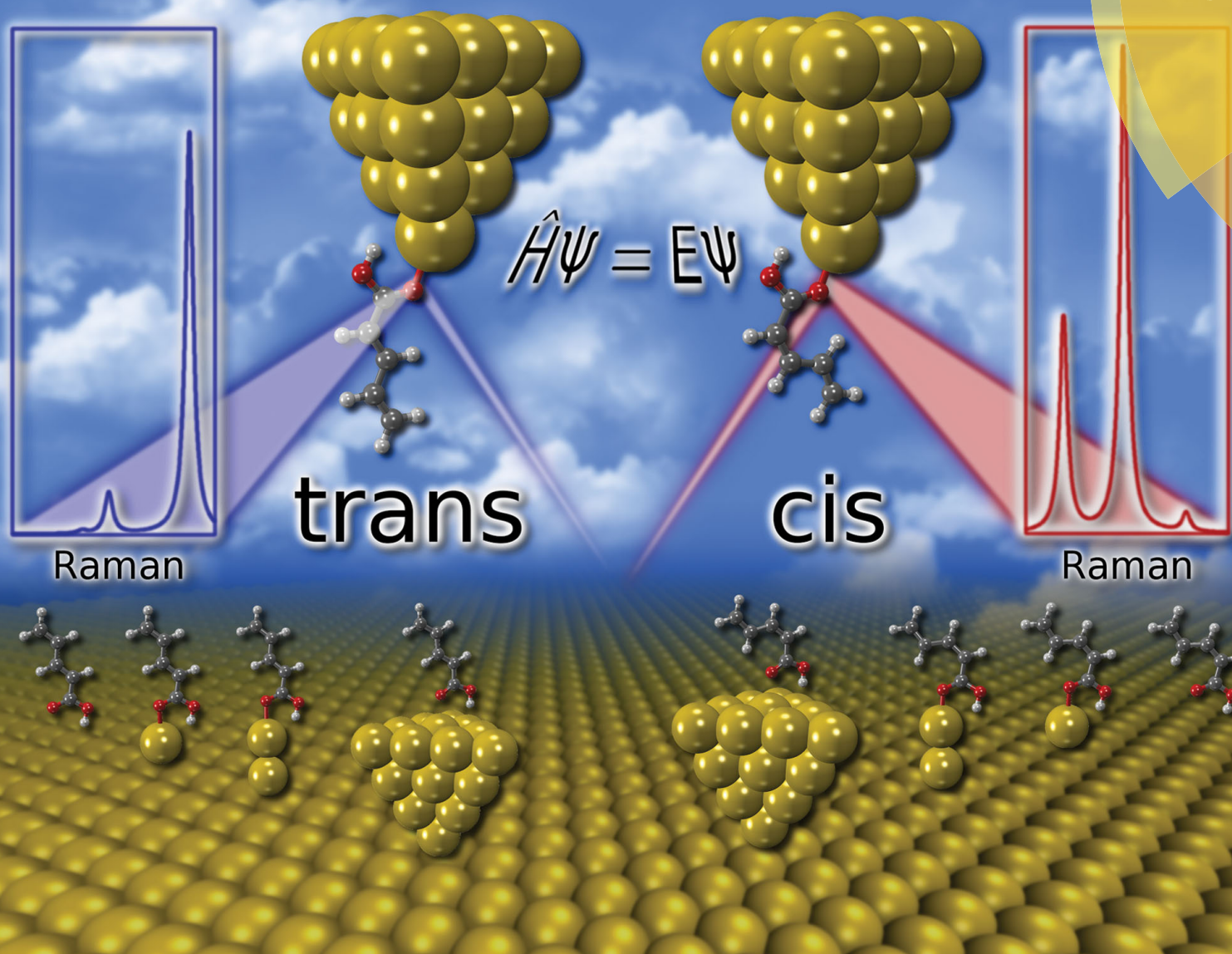
PAPER
Philipp Marquetand *et al.*
A spectroscopic study of the *cis/trans*-isomers of penta-2,4-dienoic acid
attached to gold nanoclusters

PCCP

A spectroscopic study of the *cis/trans*-isomers of penta-2,4-dienoic acid attached to gold nanoclusters

Federico Latorre,[ab] Julien Guthmuller[c] and Philipp Marquetand*[b]

In this theoretical work, we present a spectroscopic analysis of the *cis/trans*-isomers of a molecular switch, penta-2,4-dienoic acid, attached to gold clusters of different size (1, 2 and 20 gold atoms). We have simulated 4 different spectroscopic techniques: Infrared spectroscopy, normal Raman scattering, absorption spectra and resonance Raman scattering. We discuss how the position and the conformation of the molecule determine the electronic structure and hence, the spectra. The calculations have been performed using density functional theory for the properties of the ground state and time-dependent density functional theory for the excited-state properties. Special emphasis is put on the resonance Raman spectra for the study of the isomers. In the present case, resonance Raman scattering is best suited to discriminate between the isomers on the gold clusters.

I. Introduction

The remarkable functionalities of molecular switches in nature make it highly desirable to develop artificial systems in a similar fashion.[1] Molecular switches are molecules that can switch reversibly between different microscopic states. Various studies on this class of molecules exist, see *e.g.* ref. 2–12. One of the most prominent examples is the retinal isomerization in rhodopsin which is responsible for signal conversion in human vision.[13]

Anchoring such switches on surfaces may lead to new functional properties, which are relevant for different fields like molecular electronics, biocompatible devices or sensing.[14] A detailed study of their microscopic properties is vital for the correct understanding of their functionality. For the investigation of these properties, different spectroscopic techniques can be used, among others infrared spectroscopy (IR), Raman scattering (RS), resonance Raman scattering (RRS), and absorption spectra in the visible and/or ultraviolet regime (UV).[15] In presence of metal surfaces, the spectroscopic signals are often dramatically increased and the corresponding techniques have received much attention recently, which is documented in several reviews for surface-enhanced infrared absorption (SEIRA),[16–18] sum-frequency generation (SFG),[19,20] surface-enhanced Raman scattering (SERS)

and its resonance Raman analog (SERRS).[18,21–24] Another variant of RS employs sharp tips to exploit the surface effect. This tip-enhanced Raman scattering (TERS) yields remarkable spatial resolution in addition to the enhanced signals.[25–28] Furthermore, the vibrations of a molecule situated between two electrodes can be monitored *via* inelastic electron tunneling spectroscopy (IETS).[29–33] All these techniques are especially suited for surface analysis in organic electronics, microfluidics or smart materials, where molecular switches are applied.[14,34]

In the present work, we use penta-2,4-dienoic acid (PDA) as a model system because it can switch between its *trans* (Fig. 1a) and its *cis* form (Fig. 1b), absorbs in an experimentally accessible region of the electromagnetic spectrum, is commercially available, and – according to our calculations – should bind to metal surfaces. In order to mimic these metal surfaces, we attach the PDA to gold nanoclusters of different sizes (1, 2 and 20 gold atoms), see Fig. 1. Hence, we will be able to study the influence of the metal on the electronic structure of the anchored molecular switch in detail. For the Au_{20} cluster, we use a tetrahedral structure, because the latter is predicted to be the most stable conformation.[35–37] Consequently, the PDA molecule can be anchored at different sites of this cluster, where we choose the center of the face, the surface conformation (Fig. 1g and h), and the opposite position, the vertex (Fig. 1i and j).

II. Computational methods

All the quantum chemical calculations presented in this work have been carried out using the GAUSSIAN 09 program.[38]

[a] *Institute of Physical Chemistry, University of Jena, 07743 Jena, Germany*
[b] *Institute of Theoretical Chemistry, University of Vienna, 1090 Vienna, Austria.*
  E-mail: philipp.marquetand@univie.ac.at
[c] *Faculty of Applied Physics and Mathematics, Gdansk University of Technology,*
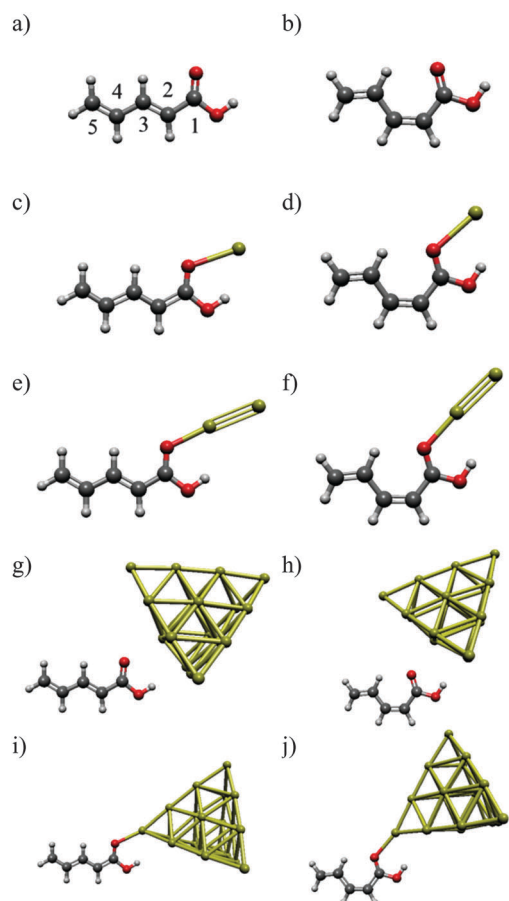 *80233 Gdansk, Poland*

Fig. 1 The systems under study: (a) *trans*-PDA (b) *cis*-PDA (c) *trans*-PDA–Au (d) *cis*-PDA–Au (e) *trans*-PDA–Au$_2$ (f) *cis*-PDA–Au$_2$ (g) *trans*-PDA–Au$_{20}$ surface (h) *cis*-PDA–Au$_{20}$ surface (i) *trans*-PDA–Au$_{20}$ vertex (j) *cis*-PDA–Au$_{20}$ vertex.

The geometries and frequencies in the ground state were calculated at the density functional theory (DFT) level[39] using the B3LYP exchange correlation (XC) functional.[40–42] With no experimental data at hand to compare to, we deem the B3LYP functional reliable for the simulation of the different spectra, see *e.g.* ref. 43. As basis sets, we use 6-311(d)[44] for the description of the PDA molecule and the quasi-relativistic effective core potential MWB60[45] for the description of the gold nanoclusters. Note that this latter choice is arbitrary to some extent since different effective core potentials yield results of similar quality, see *e.g.* ref. 46. The excited-state properties were obtained at the time-dependent DFT (TD-DFT) level[47] using the same XC functional, basis set and core potential. All systems are assumed neutral, *i.e.*, the systems with one Au atom are open-shell systems.

For the evaluation of the RRS intensities, we used the excited-state gradient method[48] employing our own code. For the isolated molecule and PDA–Au cluster, the RRS intensities were obtained within the short-time approximation (STA).[43,49,50] For a given normal mode r, its fundamental transition g0 → g1$_r$, from the vibrational ground state of the electronic ground state to the first vibrational excited state at the electronic ground state, the STA intensity expression is:

$$I_{g0 \to g1_r} \propto \frac{1}{\omega_r} \left(\frac{\partial E^e}{\partial Q_r} \right)_0^2,$$

where ω_r is the frequency of the rth normal vibration and $(\partial E^e / \partial Q_r)_0$ is the partial derivative of the resonant electronic excited state energy along the mass-weighted normal mode Q_r at the ground state equilibrium.[51]

The PDA–Au$_2$ and especially the PDA–Au$_{20}$ cluster exhibit several close-lying electronic states which are conjointly excited in a RRS process. Therefore, the RRS intensities cannot be obtained within the STA, but the sum-over-states expression has to be employed:[52,53]

$$I_{g0 \to g1_r}(\omega_L) \propto \omega_L(\omega_L - \omega_r)^3 \sum_{\alpha, \beta} \left| (\alpha_{\alpha\beta})_{g0 \to g1_r} \right|^2$$

where ω_L is the laser frequency and $(\alpha_{\alpha\beta})_{g0 \to g1_r}$ is expressed as:

$$(\alpha_{\alpha\beta})_{g0 \to g1_r} = \frac{1}{\hbar} \sum_e (\mu_{ge})_\alpha (\mu_{ge})_\beta \frac{\Delta_{e,r}}{\sqrt{2}} \{ \Phi_e(\omega_L) - \Phi_e(\omega_L - \omega_r) \}$$

where the summation over e takes all contributing electronic excited states into account, $(\mu_{ge})_\alpha$ is a component of the transition dipole, $\Delta_{e,r}$ is the dimensionless displacement of the potential minimum of the excited state e with respect to the potential minimum of the electronic ground state in the rth normal coordinate and Φ_e describes the RRS intensity with respect to the frequencies ω, see ref. 52. Following the procedure of previous works[52,54] the Frank–Condon factors were neglected in the function Φ_e.

III. Results and discussions

(a) Gold position

In order to locate the preferred binding site of the PDA to the gold clusters, we performed geometry optimizations with randomly varied starting positions. For PDA–Au, all simulations ended in one of two local minima, corresponding to conformations which we term A and B. Their structures are depicted in Fig. 2. The same binding sites were discovered for PDA–Au$_2$ (not shown) and from this fact as well as from the following results, we see no distinct impact of the closed-shell or open-shell character of the systems. In all calculations, the position A is more stable than the position B (see Table 1). Since calculations for PDA–Au$_{20}$ are expensive, only position A was considered for both surface and vertex conformers. As in the other cases, a potential minimum was found. Consequently, position A was taken as the global minimum and used in all further calculations.
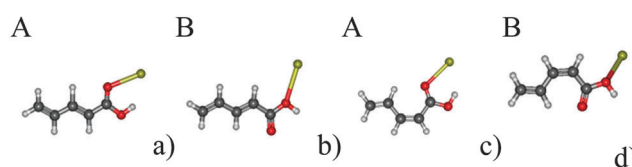

Fig. 2 The obtained stable positions for both isomers with 1 Au. (a) Position A for the *trans* isomer, (b) Position B for the *trans* isomer, (c) position A for the *cis* isomer, (d) position B for the *cis* isomer.

Table 1 Relative energies (in eV) of the different minima including zero-point energy corrections obtained for the binding of the PDA molecule to gold atoms

	Au/eV	Au$_2$/eV
cis		
Position A	0.00	0.00
Position B	0.16	0.27
trans		
Position A	0.00	0.00
Position B	0.17	0.30

(b) Property changes with gold-cluster size

When adding the different gold clusters, the electronic structure of the PDA molecule is changed. This modification is reflected in the geometry. Table 2 shows changes in bond lengths with respect to the single PDA molecule for different gold-cluster sizes. The molecule is attached *via* its carboxylic oxygen to the gold. As a consequence, the bond of the carboxyl group is stretched. The effect is promoted further along the conjugated chain of the PDA and the following bonds are contracted and stretched in alternating order. A second effect is that the O–H bond of the acid group is stretched, which implies that the bond is weakened and the molecule becomes more acidic.

The bond-length changes can be understood when looking at the electric charges with respect to the gold-cluster size. In all calculations, the gold cluster obtains a negative summed partial charge of approximately −0.1 e for the PDA–Au system and −0.2 e in the other systems, according to a Hirshfeld[55–57] population analysis (−0.2 e for all systems according to a Mulliken analysis). Hence, electron density is transferred from the PDA to the gold. This process can be seen as a partial enolisation. Thus, the gold acts as a Lewis acid.[58,59] It is interesting to note that the charge distribution in Au$_{20}$ is not uniform but a Hirshfeld charge of approximately −0.02 e (−1.0 e in the Mulliken analysis) is found at each of the four tips, while the center atom on each face is charged as approximately +0.02 e (+1.3 e in Mulliken analysis). This symmetrical distribution of the charges in the Au$_{20}$ leads to an overall dipole moment of zero.[35] Despite having a zero dipole moment, the Au$_{20}$ has a great ability to deform its electron density.

The dipole moment (defined as pointing from the negative to the positive charges) of the total system is pointing away from the gold cluster, approximately along the carbon chain of the PDA. The absolute values for the studied systems are compiled in Table 3. We find an increase of the dipole moment strength with cluster size with exception of the PDA–Au$_{20}$ surface cluster. In the latter case, the bond between molecule and Au cluster is longer due to steric reasons compared to the other systems. As a consequence, the electrostatic interaction is less pronounced and the dipole moment is smaller. When comparing the *trans* and *cis* isomers, we see that already for the pure molecule the *trans* isomer exhibits a stronger dipole moment than the *cis* form. The difference of ∼0.5 D is retained also for the different Au-cluster systems (see Table 3).

Table 2 Main bond lengths in the systems under study at their respective equilibrium geometry

	trans	*cis*
Bond	Distance/Å	Distance/Å
PDA		
C$_2$=C$_3$	1.343	1.348
C$_4$=C$_5$	1.339	1.339
C$_1$–C$_2$	1.473	1.473
C$_3$–C$_4$	1.449	1.452
C=O	1.210	1.211
C–OH	1.358	1.359
O–H	0.969	0.969
Au		
C$_2$=C$_3$	1.345	1.349
C$_4$=C$_5$	1.339	1.340
C$_1$–C$_2$	1.468	1.468
C$_3$–C$_4$	1.448	1.450
C=O	1.225	1.227
C–OH	1.339	1.340
O–H	0.980	0.980
O–Au	2.559	2.568
Au$_2$		
C$_2$=C$_3$	1.346	1.351
C$_4$=C$_5$	1.339	1.340
C$_1$–C$_2$	1.460	1.460
C$_3$–C$_4$	1.446	1.449
C=O	1.236	1.237
C–OH	1.330	1.332
O–H	0.980	0.980
O–Au	2.266	2.267
Au$_{20}$ vertex		
C$_2$=C$_3$	1.346	1.351
C$_4$=C$_5$	1.339	1.340
C$_1$–C$_2$	1.463	1.463
C$_3$–C$_4$	1.447	1.449
C=O	1.230	1.231
C–OH	1.338	1.340
O–H	0.976	0.976
O–Au	2.426	2.432
Au$_{20}$ surface		
C$_2$=C$_3$	1.334	1.349
C$_4$=C$_5$	1.339	1.340
C$_1$–C$_2$	1.472	1.472
C$_3$–C$_4$	1.449	1.451
C=O	1.217	1.218
C–OH	1.349	1.351
O–H	0.975	0.975
O–Au	2.882	2.905

Table 3 Dipole moments (in D) for each system

	$\bar{\mu}$ (D)	
System	*trans*	*cis*
Isolated molecule	1.7750	1.3012
Au cluster	4.1958	3.6838
Au$_2$ cluster	6.4474	5.8688
Au$_{20}$ vertex cluster	7.6507	7.0400
Au$_{20}$ surface cluster	3.1824	2.6136

The presence of the gold clusters leaves the energetic differences between both isomers unaffected, where the *trans* form is always more stable than the *cis* isomer with an energy difference of 0.082 eV. Since the thermal energy provided at

7650 | *Phys. Chem. Chem. Phys.*, 2015, **17**, 7648–7658

This journal is © the Owner Societies 2015

room temperature (298.15 K) is only 0.025 eV, the *trans* isomer is thermo-dynamically favored (*trans*/*cis* = 16:5 according to the Boltzmann distribution).

Next, we turn to the normal modes. We have identified three important ones for the study of the isomerization process, which we term the asymmetric C=C stretch ($\nu^a_{C=C}$), the symmetric C=C stretch ($\nu^s_{C=C}$), and the carbonyl stretch ($\nu_{C=O}$). They are indicated in Fig. 3 for the *cis* and the *trans* isomer,

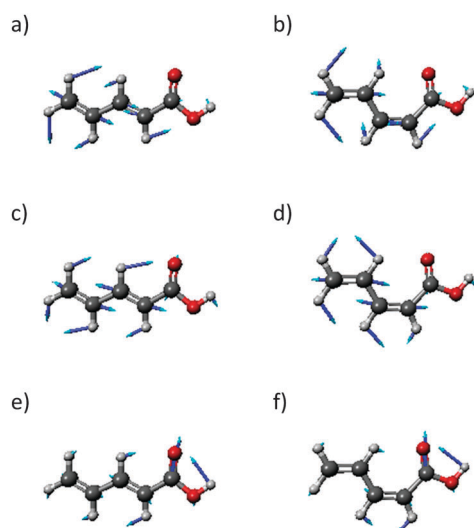respectively. The main feature of $\nu^a_{C=C}$ is that one of the C=C double bonds is enlarged while the other C=C double bond is shortened. For $\nu^s_{C=C}$, both C=C double bonds are stretched concertedly. The predominant vibration of $\nu_{C=O}$ is along the C=O double bond although the other atoms of the PDA are also involved. The corresponding frequencies for the different systems are listed in Table 4.

(c) Infrared spectra (IR)

All IR spectra presented in this section have been limited to a frequency range from 1000 to 1800 cm^{-1} in order to focus on the normal modes of interest. All frequencies have been scaled by a factor of 0.97 (to account for a systematic error in the DFT predictions)[60] and intensities convoluted by Lorentzians of 20 cm^{-1} full width at half maximum (FWHM)[61] to account for line broadening in possible future experimental spectra.

The intensity patterns in the IR spectra (Fig. 4) show a strong dependency on the size of the cluster. For the isolated molecule, the IR spectrum shows higher peaks in the range of the carbon–carbon single bond modes (ν_{C-C}, 1000–1300 cm^{-1}) than in the $\nu_{C=C}$ range (1500–1800 cm^{-1}). When the molecule interacts with one gold atom, the intensity ratio between these ranges is diminished for the *cis* isomer and even inverted for the *trans* isomer. Continuing with the PDA–Au$_2$ and PDA–Au$_{20}$ vertex cluster, this intensity inversion phenomenon is even more distinctive. In these cases, the ν_{C-C} modes are of minor importance with respect to the $\nu_{C=C}$ modes. For the PDA–Au$_{20}$ surface system, the trend does not continue, instead, the relative intensity patterns are very similar to the PDA–Au system. Note that

Fig. 3 Normal modes of the *trans* and *cis* PDA. (a) $\nu^a_{C=C}$ for the *trans* isomer, (b) $\nu^a_{C=C}$ for the *cis* isomer, (c) $\nu^s_{C=C}$ for the *trans* isomer, (d) $\nu^s_{C=C}$ for the *cis* isomer, (e) $\nu_{C=O}$ for the *trans* isomer, (f) $\nu_{C=O}$ for the *cis* isomer.

Table 4 Frequencies of selected normal modes and corresponding signal strength for different types of spectroscopy of the various systems under study. The frequencies were corrected by a scale factor of 0.97. The intensities units for infrared are km mol^{-1}, Raman scattering are Å^4 amu^{-1} and resonance Raman scattering are relative intensities

trans					*cis*			
Mode	$\tilde{\nu}$/cm^{-1}	I (IR)/km mol^{-1}	I (RS)/Å^4 amu^{-1}	I_{rel} (RRS)	$\tilde{\nu}$/cm^{-1}	I (IR)/km mol^{-1}	I (RS)/Å^4 amu^{-1}	I_{rel} (RR)
PDA								
$\nu^a_{C=C}$	1613.9	81.01	2.9	<0.01	1599.3	100.27	26.3	0.06
$\nu^s_{C=C}$	1650.7	108.57	797.9	1.00	1644.9	72.99	482.7	1.00
$\nu_{C=O}$	1746.1	254.96	21.3	<0.01	1737.3	215.54	17.7	0.01
PDA–Au								
$\nu^a_{C=C}$	1610.8	178.25	77.3	0.08	1594.1	204.67	117.0	0.20
$\nu^s_{C=C}$	1632.5	476.90	1578.5	1.00	1632.0	264.17	799.8	1.00
$\nu_{C=O}$	1673.6	211.75	64.9	0.04	1664.6	252.43	83.2	<0.01
PDA–Au$_2$								
$\nu^a_{C=C}$	1617.6	432.38	1082.3	0.73	1587.8	452.50	369.1	0.40
$\nu^s_{C=C}$	1606.8	686.88	417.0	1.00	1618.0	419.04	651.9	1.00
$\nu_{C=O}$	1661.5	124.03	40.2	0.06	1651.9	184.62	221.0	0.13
PDA–Au$_{20}$ vertex								
$\nu^a_{C=C}$	1608.0	742.65	1066.8	<0.01	1590.5	658.71	715.6	0.45
$\nu^s_{C=C}$	1622.4	978.96	3945.2	0.11	1623.3	780.96	2006.0	1.00
$\nu_{C=O}$	1666.1	195.94	362.43	1.00	1657.1	268.97	186.8	0.04
PDA–Au$_{20}$ surface								
$\nu^a_{C=C}$	1611.6	152.11	59.8	<0.01	1595.3	187.57	119.0	0.12
$\nu^s_{C=C}$	1642.8	377.45	2677.7	0.18	1639.1	194.05	872.7	1.00
$\nu_{C=O}$	1696.2	379.37	230.4	1.00	1690.4	394.20	332.9	0.15

This journal is © the Owner Societies 2015

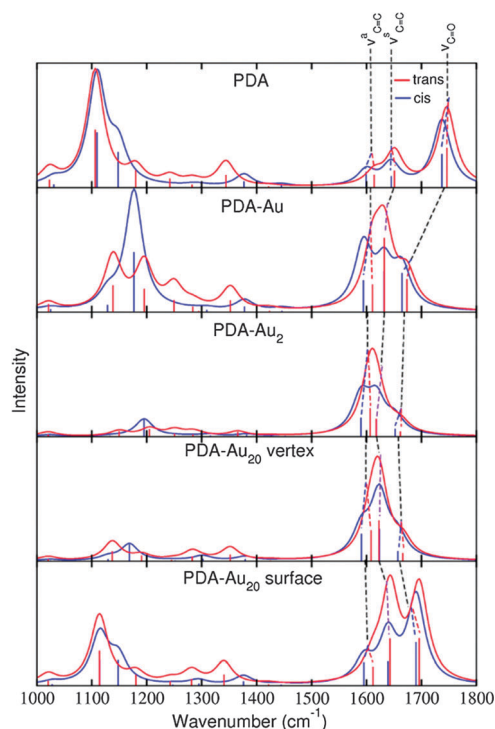*Phys. Chem. Chem. Phys.*, 2015, **17**, 7648–7658 | **7651**

Fig. 4 IR spectra of *trans* (red) and *cis* (blue) isomers of the different systems as indicated. The line spectra were convoluted by Lorentzians of 20 cm^{-1} FWHM.

the absolute intensities of the $\nu_{C=C}$ modes increase when the gold cluster size increases (Table 4), while the $\nu_{C=O}$ intensities decrease. Again, the PDA–Au$_{20}$ surface system is an exception to this rule, where the absolute intensities of the $\nu_{C=C}$ modes are similar to the ones of the isolated molecule.

Not only the intensities change for different cluster sizes, also the frequencies are shifted. As stated above, the gold acts as a Lewis acid leading to a partial enolisation of PDA. Accordingly, the C=C double bonds are elongated, accompanied by a shift of $\nu_{C=C}$ to lower frequencies. In turn, the C–C single bonds are shortened leading to a partial double bond character and hence, the $\nu_{C–C}$ modes shift to higher frequencies. Also due to the enolisation effect, the bond length of the carboxyl group is increased and therefore, lower frequency values of the $\nu_{C=O}$ mode can be observed. The absolute frequency shifts increase in the following order: PDA < PDA–Au$_{20}$ surface < PDA–Au < PDA–Au$_{20}$ vertex < PDA–Au$_2$. This order is directly reflected in the changes of the respective bond lengths, which are collected in Table 2. Not only the bond lengths related to the aforementioned partial enolisation fit to the observed order; also the distance between the binding oxygen of the PDA and the nearest gold atom fits this series. This distance is the shortest in PDA–Au$_2$ and the longest in PDA–Au$_{20}$ surface. The reason for the long bond in the latter system is the steric hindrance between the OH group and the Au surface.

It becomes clear that the geometry of the metal nanocluster where the molecule binds is of vital importance (see also ref. 62), leading to different results. Especially, the planar binding site in PDA–Au$_{20}$ surface compared to the tetrahedral one in PDA–Au$_{20}$

vertex (which resembles a metallic tip) shows intrinsic differences which can be interesting, *e.g.*, in the understanding of SERS and TERS or, in this case, SEIRA. Note that our simulations can reproduce only a part of the SEIRA enhancement mechanism, plasmonic contributions[18] or phenomena like hot electrons[63,64] are not described in the present approach.

We show additionally that the above-discussed changes are more pronounced in the *trans* than in the *cis* isomer (see Fig. 4). This difference is similar to the one for the dipole moment discussed above. The reason is that the *trans* isomer is bound closer to the Au cluster than the *cis* isomer.

If we want to distinguish between the isomers, IR spectra are expected to be unsuited, since the spectra are very similar for typical linewidths (see Fig. 4). High-resolution spectroscopy[15] could solve this problem. In this case, the attachment to gold clusters leads to more pronounced differences in the spectra and makes the differentiation between the isomers easier. Also the influence of the gold cluster size as described above could then be studied experimentally. However, if conventional IR spectra are recorded, the limited resolution might make such a task impossible. Consequently, other types of spectroscopy are considered in the following.

(d) Raman scattering (RS)

The RS spectra presented in this section have been prepared analogously to the IR spectra. Also the RS spectra are shown for a frequency range from 1000 to 1800 cm^{-1} (see Fig. 5), all frequencies have been scaled by a factor of 0.97 and convoluted
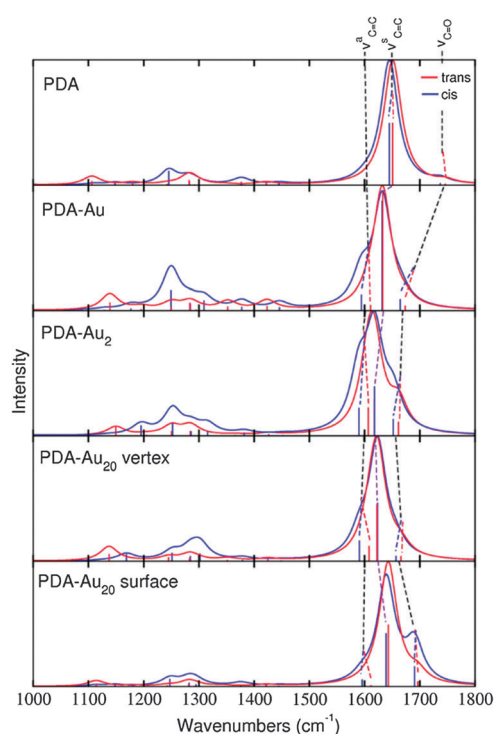

Fig. 5 RS spectra of *trans* (red) and *cis* (blue) isomers of the different systems as indicated assuming an excitation wavelength of 1064 nm. The line spectra were convoluted by Lorentzians of 20 cm^{-1} FWHM.

7652 | *Phys. Chem. Chem. Phys.*, 2015, **17**, 7648–7658

This journal is © the Owner Societies 2015

by Lorentzians of 20 cm^{-1} FWHM to account for a typical line broadening.[65] In order to simulate off-resonance RS, the excitation wavelength is chosen to be 1064 nm ($\cong$1.2 eV), where no transitions to electronic excited states are induced (see next section).

The frequencies of the vibrational modes are naturally the same as in the IR spectra. Due to the low symmetry of the system, especially when including the gold clusters, normal modes are obtained which are both IR and Raman active. Therefore, the properties of the frequencies in the Raman spectra have been already discussed in the previous section.

Looking at the intensities of the RS spectra (Fig. 5), one observes that the $\nu_{C=C}$ modes are dominating while the ν_{C-C} and $\nu_{C=O}$ modes – in contrast to the IR spectra – are less intense. No clear trend is found for the absolute intensities, in some cases the signal for $\nu^a_{C=C}$ is the strongest, in other cases the one for $\nu^s_{C=C}$, see Table 4. However, the absolute intensities of the $\nu_{C=C}$ and $\nu_{C=O}$ modes are higher for the larger gold clusters. This effect is well-known and contributes to the chemical enhancement mechanism in SERS.[18,66] Note that a full simulation of SERS spectra requires incorporating additional mechanisms like the electromagnetic enhancement induced by plasmonic excitations, see *e.g.* ref. 18 and 67. Table 4 also shows that the absolute intensities are higher for the PDA–Au$_{20}$ vertex than for the PDA–Au$_{20}$ surface system. This fact, once again, shows that the geometry of the metal nanostructure, where the molecule is attached, is important. Additionally, the absolute intensities are higher for the *trans* than for the *cis* systems and also the increase with gold-cluster size is more pronounced for the *trans* isomers. However, this effect in absolute intensity can be rarely observed in experimental spectra since the measurement of absolute scattering cross sections is difficult. Therefore, the spectra in Fig. 5 are normalized with respect to the highest peak of each spectrum as is often done in experiments. In combination with the typical line broadening, a distinction between *cis* and *trans* isomers is hardly possibly using RS. Higher resolution is commonly obtained employing RRS spectroscopy, which will be discussed below. As a pre-condition for RRS, information about the energies of the electronic excited states is required and thus, the UV absorption spectra will be discussed in the following.

(e) Absorption spectra (UV)

The study of the absorption spectra can provide valuable insight into the electronic structure and hence, the discrimination of different switch states might be possible directly. Beyond this fact, a study of the absorption spectra is needed in order to select the excited states which are in resonance in RRS and to identify the states with the properties of interest. In the present study, special attention is paid to states that have an important $\pi \rightarrow \pi^*$ contribution, because this transition influences the nature of the double bonds which are key for the *cis/trans* isomerization of the PDA molecule.

The absorption spectra are shown in Fig. 6. They are generated from TDDFT simulations, where the obtained line spectrum is broadened with Lorentzians of 0.05 eV FWHM. The computations include a maximum number of 10, 20, 50 or 1000
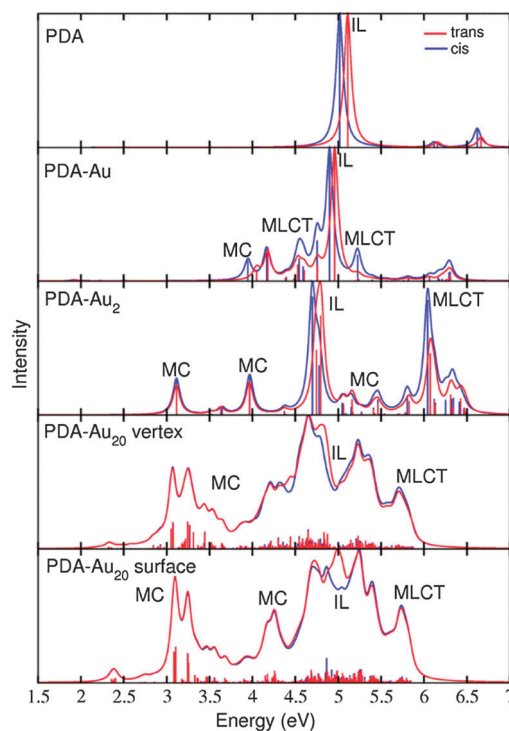

Fig. 6 Absorption spectra of *trans* (red) and *cis* (blue) isomers for the systems under study. The transitions were broadened by Lorentzians of 0.05 eV FWHM.

excited states for PDA, PDA–Au, PDA–Au$_2$ or PDA–Au$_{20}$, respectively. For further analysis, all computed electronic excited states are classified according to the nature of the Kohn–Sham orbitals participating in the transitions.[68]

In the following, states involving transitions, where both the initial and the final orbital are localized in the metal cluster alone, are termed metal center (MC) states. If the participating orbitals are localized only in the PDA molecule, which can be called ligand in order to stay in the terminology used for metallo-organic compounds, the corresponding state is termed intra-ligand (IL) state. If transitions from orbitals in the metal cluster to orbitals in the ligand play a role, the state is labeled as metal–ligand charge-transfer (MLCT) state. Obviously, an electronic state is not necessarily pure and also mixtures of MC, IL and MLCT character may occur.
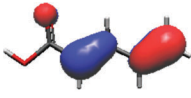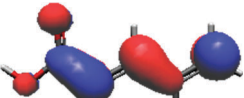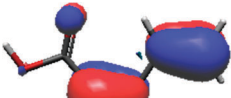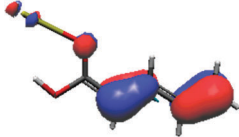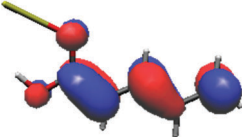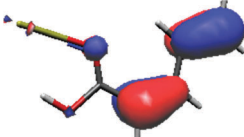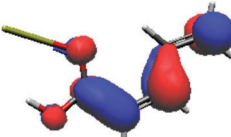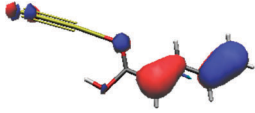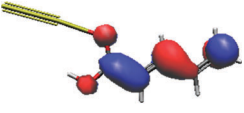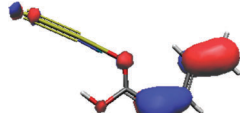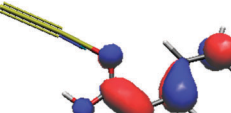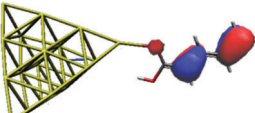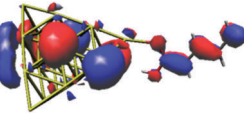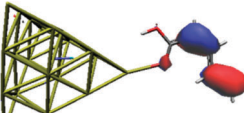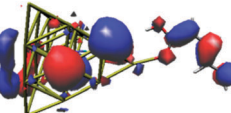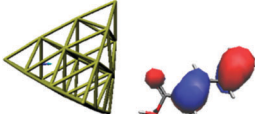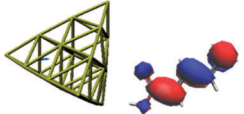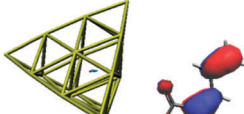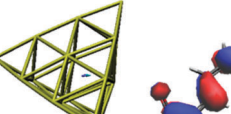
The absorption spectra (Fig. 6) reveal how the excited state composition changes for the different molecule-gold clusters. The low energy region of the absorption spectra is governed by MC states, the IL state of interest (with $\pi \rightarrow \pi^*$ transition) is found approximately between 4.5 and 5.5 eV and the high energy region (above 5.5 eV) is dominated by MLCT states.

In order to identify the desired $\pi \rightarrow \pi^*$ state, the simulation outcome is scanned for the orbitals of interest. These orbitals are plotted in Table 5 for the respective systems. States with a large contribution of this $\pi \rightarrow \pi^*$ transition are collected in Table 6.

While for the pure PDA molecule the $\pi \cdot \pi^*$ orbitals are important only for a single electronic state, the situation is more complex if metal atoms are added. For the cluster systems, the character of the

This journal is © the Owner Societies 2015

Phys. Chem. Chem. Phys., 2015, **17**, 7648–7658 | **7653**

Table 5 π and π* Kohn–Sham orbitals for each system calculated at the B3LYP/6-311(d)/MWB60 level of theory. The number of the respective orbital according to the G09 output is given in brackets to indicate the increasing complexity of the larger systems

trans		cis	
π → π		π → π*	

PDA

π(26) — π*(27) — π(26) — π*(27)

PDA–Au

π(35) — π*(37) — π(35) — π*(37)

PDA–Au$_2$

π(39) — π*(46) — π(39) — π*(46)

PDA–Au$_{20}$ vertex

π(195) — π*(226) — π(195) — π*(226)

PDA–Au$_{20}$ surface

π(210) — π*(227) — π(210) — π*(227)

states of interest is mixed and *e.g.* for the PDA–Au$_{20}$ surface system, the states are a mixture of IL (only 5–10%, including π → π*), MLCT, and MC type. A clear classification of the state character is hence impossible for the larger clusters, not only because of the mixing of transitions but also because the orbitals themselves already show some mixed character, see *e.g.* small contributions localized in the metal for the π orbitals of PDA–Au or PDA–Au$_2$ as shown in Table 5. This phenomenon is even more pronounced for the π* orbital of the PDA–Au$_{20}$ vertex system. Such mixed orbitals

are quite common and further conclusions based on this fact are difficult since in general a specific molecular orbital basis is not unique. However, the observed mixture may indicate that the different parts of the system (PDA molecule and metal cluster) may not be seen as separate fragments but are entangled to a great extent.

When comparing the *cis* and *trans* isomers, we find it difficult to distinguish the two forms of the respective systems, see Fig. 6 and Table 6. However, small differences can be found

Paper

Table 6 Energies, oscillator strengths (f) and composition of excited states with contribution of $\pi \rightarrow \pi^*$ transitions. For further details, see text

trans					cis				
State	ΔE/eV	f	Character	c^2/%	State	ΔE/eV	f	Character	c^2/%
PDA									
2	5.1104	0.706	IL	99.9	2	5.0166	0.566	IL	99.9
PDA–Au									
24	4.9584	0.778	IL	48.8	24	4.8998	0.492	IL	45.0
			MC	51.2				MC	55.0
PDA–Au$_2$									
17	4.7440	0.357	IL	32.2	17	4.6978	0.495	IL	73.0
			MC	67.8				MC	27.0
19	4.7981	0.547	IL	50.6	20	4.7771	0.207	IL	14.2
			MC	49.4				MC	85.8
PDA–Au$_{20}$ vertex									
433	4.5859	0.085	IL	3.6	434	4.5807	0.031	IL	7.8
			MC	71.9				MC	80.7
			MLCT	24.5				MLCT	11.5
445	4.6142	0.018	IL	8.6	459	4.6482	0.154	IL	2.8
			MC	68.6				MC	97.2
			MLCT	22.8					
456	4.6390	0.043	IL	2.6	519	4.7925	0.081	IL	3.2
			MC	80.0				MC	94.0
			MLCT	17.4				MLCT	2.8
458	4.6487	0.140	IL	3.2					
			MC	94.4					
			MLCT	2.4					
539	4.8344	0.133	IL	2.4					
			MC	68.8					
			MLCT	28.8					
PDA–Au$_{20}$ surface									
544	4.8733	0.080	IL	4.6	544	4.8659	0.177	IL	21.0
			MC	95.4				MC	79.0
552	4.8952	0.046	IL	5.0	567	4.9245	0.095	IL	6.8
			MC	90.6				MC	93.2
			MLCT	4.4					
579	4.9576	0.060	IL	7.4	586	4.9692	0.050	IL	2.4
			MC	83.2				MC	86.8
			MLCT	9.4				MLCT	10.8
590	4.9833	0.081	IL	5.2					
			MC	94.8					
592	4.9890	0.089	IL	4.8					
			MC	92.3					
			MLCT	2.9					

and these will lead to noticeable differences in the RRS spectra, as discussed in the next section.

(f) Resonance Raman scattering (RRS)

Fig. 7 shows the RRS spectra of the different PDA systems. All spectra are prepared in the same manner as the IR and RS spectra previously, *i.e.*, a frequency range from 1000 to 1800 cm^{-1} has been adopted and all the frequencies have been scaled by a factor of 0.97. Since RRS spectra offer high resolution,[43] the obtained line spectra have been convoluted by Lorentzians of 5 cm^{-1} FWHM.

The wavelength for the resonant excitation is chosen to match the energy difference between the electronic ground state and the IL states with a strong oscillator strength and the biggest contribution of the transition $\pi \rightarrow \pi^*$. The selected states and their energies, oscillator strengths and characters are presented in Table 6.

As intended by the choice of the excitation wavelength, the RRS spectra are dominated by peaks in the region of the $\nu_{C=C}$ modes.

The RRS spectra of the isolated PDA molecule are very similar comparing the *cis* and *trans* isomers. Only minor changes are observed for the molecule attached to a single gold atom. For the PDA–Au$_2$ system, differences are visible in the RRS spectra. The vibrational mode $\nu_{C=C}^a$ is shifted to higher wavenumbers in the *trans* isomer, while the *cis* isomer exhibits approximately the same frequency as the pure molecule. Differences in the spectra are even more pronounced for the PDA–Au$_{20}$ clusters. The *trans* isomers of the PDA–Au$_{20}$ surface and PDA–Au$_{20}$ vertex systems show an intense peak for the normal mode $\nu_{C=O}$ (1666.1 and 1696.2 cm^{-1} respectively), while the *cis* isomer exhibits an intense $\nu_{C=C}^s$ mode (1623.3 and 1639.1 cm^{-1} respectively). Additionally, the mode $\nu_{C=C}^a$ at 1595.3 cm^{-1} is enhanced in the *cis* isomer of the PDA–Au$_{20}$ vertex system, while in the *trans* isomer this vibrational normal mode has a very low intensity.

Such differences are not observed in the RS spectra (see Section d), where no resonance enhancement is present. Hence,
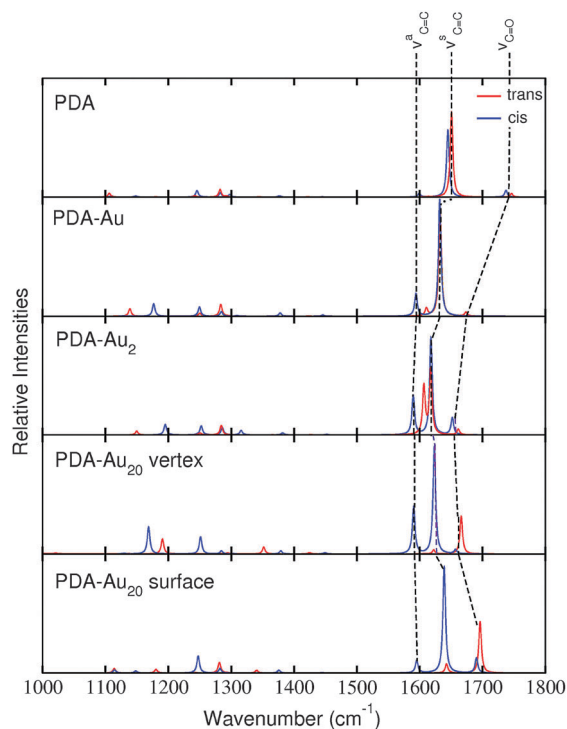
Fig. 7 RRS spectra of *trans* (red) and *cis* (blue) isomers of the various systems. The line spectra were convoluted by Lorentzians of 5 cm^{-1} FWHM.

these differences stem from the differing excited states which are involved for the *cis* or the *trans* isomer, respectively (see the different composition of the respective states in Table 6).

As stated above (see Section d), the attachment of a molecule to gold nanoparticles leads to significant enhancement of the spectroscopic signals. Hence, only a small amount of a substance is needed to carry out an analysis, *i.e.*, to record a SERRS spectrum in this case. The spectra presented here predict such SERRS signals, since the chemical effect included in the present calculations is mainly responsible for the relative intensities of the peaks, while plasmonic effects (neglected here) primarily influence the absolute intensities.[66,67]

From the different points given above, we infer that a combination of RRS and attachment to metal clusters is well-suited to distinguish between molecular species which are difficult to discern using other types of spectroscopy. The critical difference in the intensities of the $\nu_{C=C}$ and $\nu_{C=O}$ modes are the reason why we can discriminate between both isomers of PDA in the present case.

IV. Conclusions

We presented a computational study focused in the discrimination between the *cis* and *trans* isomers of the PDA molecule attached to gold clusters of different size using different spectroscopic techniques. It was shown that the interaction between our molecule and the gold clusters leads to a partial enolisation of the two isomers, which affects the intensity pattern of IR and RS spectra. The effect is more pronounced for larger gold clusters, however, the respective *cis* and *trans* isomers show very similar spectra.

Furthermore, we investigated properties of the excited states and simulated UV absorption spectra giving insight into how the molecule interacts with the gold cluster at higher energies. The data obtained in this way was then used in the simulation of RRS spectra. Finally, we found that RRS spectroscopy is a suitable tool for the discrimination of the PDA isomers attached to gold nanoparticles. Reasons are a high spectral resolution and more importantly, that excited-state properties influence the signal strength of vibrational modes differently for the different isomers.

Additionally, we have shown that the position where the molecule binds to a larger cluster matters. In the present study, the Au$_{20}$ vertex and Au$_{20}$ surface positions were compared and found to yield different spectra.

Last but not least, we hope to encourage experimental studies on the presented system in order to compare to the results that we showed in this work.

Acknowledgements

References

1 M. Weinelt and F. von Oppen, *J. Phys.: Condens. Matter*, 2012, **24**, 390201.
2 P. Marquetand, S. Gräfe, D. Scheidel and V. Engel, *J. Chem. Phys.*, 2006, **124**, 054325.
3 K. Hoki, M. Sato, M. Yamaki, R. Sahnoun, L. Gonzalez, S. Koseki and Y. Fujimura, *J. Phys. Chem. B*, 2004, **108**, 4916.
4 G. Pérez-Hernández, A. Pelzer, L. González and T. Seideman, *New J. Phys.*, 2010, **12**, 075007.
5 B. Klaumünzer and D. Kröner, *New J. Chem.*, 2009, **33**, 186.
6 D. Kinzel, P. Marquetand and L. González, *J. Phys. Chem. A*, 2012, **116**, 2743.
7 P. Marquetand, P. Nuernberger, T. Brixner and V. Engel, *J. Chem. Phys.*, 2008, **129**, 074303.
8 S. Banerjee, D. Kröner and P. Saalfrank, *J. Chem. Phys.*, 2012, **137**, 22A534.
9 B. Feringa and W. Browne, *Molecular Switches*, 2nd edn, 2011, vol. 1.
10 J. J. Bajo, J. González-Vázquez, I. Sola, J. Santamaria, M. Richter, P. Marquetand and L. González, *J. Phys. Chem. A*, 2012, **116**, 2800.
11 K. Lu, G. Finn, T. Lee and L. Nicholson, *Nat. Chem. Biol.*, 2007, **3**, 619.
12 R. Rowan, A. Warshel, B. D. Skyes and M. Karplus, *Biochemistry*, 1974, **13**, 970.
13 C. Dugave and L. Demange, *Chem. Rev.*, 2003, **103**, 2475.

7656 | *Phys. Chem. Chem. Phys.*, 2015, **17**, 7648–7658

This journal is © the Owner Societies 2015

14 W. Browne and B. Feringa, *Annu. Rev. Phys. Chem.*, 2009, **60**, 407.

15 M. Quack, *Fundamental Symmetries and Symmetry Violations from High Resolution Spectroscopy*, John Wiley & Sons, Ltd, 2011.

16 M. Osawa, Surface-enhanced infrared absorption, in *Near-Field Optics and Surface Plasmon Polaritons*, Topics in Applied Physics, ed. S. Kawata, Springer Berlin Heidelberg, 2001, vol. 81, pp. 163–187.

17 R. Aroca, D. Ross and C. Domingo, *Appl. Spectrosc.*, 2004, **58**, 324A.

18 S. M. Morton, D. W. Silverstein and L. Jensen, *Chem. Rev.*, 2011, **111**, 3962.

19 J. Guthmuller, F. Cecchet, D. Lis, Y. Caudano, A. A. Mani, P. A. Thiry, A. Peremans and B. Champagne, *ChemPhysChem*, 2009, **10**, 2132.

20 C. Feugmo and V. Liègeois, *ChemPhysChem*, 2013, **14**, 1633.

21 L. Jensen, C. M. Aikens and G. C. Schatz, *Chem. Soc. Rev.*, 2008, **37**, 1061.

22 D. Cialla, A. März, R. Böhme, F. Theil, K. Weber, M. Schmitt and J. Popp, *Anal. Bioanal. Chem.*, 2012, **403**, 27.

23 L. Tong, T. Zhu and Z. Liu, *Chem. Soc. Rev.*, 2011, **40**, 1296.

24 S. Schlücker, *Angew. Chem., Int. Ed.*, 2014, **53**, 4756.

25 E. Bailo and V. Deckert, *Chem. Soc. Rev.*, 2008, **37**, 921.

26 B. Pettinger, P. Schambach, C. J. Villagómez and N. Scott, *Annu. Rev. Phys. Chem.*, 2012, **63**, 379.

27 C. Blum, L. Opilik, J. M. Atkin, K. Braun, S. B. Kämmer, V. Kravtsov, N. Kumar, S. Lemeshko, J.-F. Li, K. Luszcz, T. Maleki, A. J. Meixner, S. Minne, M. B. Raschke, B. Ren, J. Rogalski, D. Roy, B. Stephanidis, X. Wang, D. Zhang, J.-H. Zhong and R. Zenobi, *J. Raman Spectrosc.*, 2014, **45**, 22.

28 D. Zhang, X. Wang, K. Braun, H.-J. Egelhaaf, M. Fleischer, L. Hennemann, H. Hintz, C. Stanciu, C. J. Brabec, D. P. Kern and A. J. Meixner, *J. Raman Spectrosc.*, 2009, **40**, 1371.

29 T. Böhler, A. Edtbauer and E. Scheer, *Phys. Rev. B: Condens. Matter Mater. Phys.*, 2007, **76**, 125432.

30 N. Okabayashi, M. Paulsson and T. Komeda, *Prog. Surf. Sci.*, 2013, **88**, 1.

31 J.-C. Leng, L. Lin, X.-N. Song, Z.-L. Li and C.-K. Wang, *J. Phys. Chem. C*, 2009, **113**, 18353.

32 M.-L. Bocquet and B. Wang, *Prog. Surf. Sci.*, 2010, **85**, 435.

33 A. Ségerie, V. Liégeois, B. Champagne, L.-L. Lin and Y. Luo, *J. Phys. Chem. A*, 2013, **117**, 12783.

34 S. Weigelt, C. Busse, L. Petersen, E. Rauls, B. Hammer, K. V. Gothelf, F. Besenbacher and T. R. Linderoth, *Nat. Mater.*, 2006, **5**, 112.

35 B. Assadollahzadeh and P. Schwerdtfeger, *J. Chem. Phys.*, 2009, **131**, 064306.

36 D. Schooss, P. Weis, O. Hampe and M. Kappes, *Philos. Trans. R. Soc., A*, 2010, **368**, 1211.

37 P. Gruene, D. M. Rayner, B. Redlich, A. F. G. Van Der Meer, J. T. Lyon, G. Meijer and A. Fielicke, *Science*, 2008, **321**, 674.

38 M. J. Frisch, G. W. Trucks, H. B. Schlegel, G. E. Scuseria, M. A. Robb, J. R. Cheeseman, G. Scalmani, V. Barone, B. Mennucci, G. A. Petersson, H. Nakatsuji, M. Caricato, X. Li, H. P. Hratchian, A. F. Izmaylov, J. Bloino, G. Zheng,

J. L. Sonnenberg, M. Hada, M. Ehara, K. Toyota, R. Fukuda, J. Hasegawa, M. Ishida, T. Nakajima, Y. Honda, O. Kitao, H. Nakai, T. Vreven, J. A. Montgomery, Jr., J. E. Peralta, F. Ogliaro, M. Bearpark, J. J. Heyd, E. Brothers, K. N. Kudin, V. N. Staroverov, R. Kobayashi, J. Normand, K. Raghavachari, A. Rendell, J. C. Burant, S. S. Iyengar, J. Tomasi, M. Cossi, N. Rega, J. M. Millam, M. Klene, J. E. Knox, J. B. Cross, V. Bakken, C. Adamo, J. Jaramillo, R. Gomperts, R. E. Stratmann, O. Yazyev, A. J. Austin, R. Cammi, C. Pomelli, J. W. Ochterski, R. L. Martin, K. Morokuma, V. G. Zakrzewski, G. A. Voth, P. Salvador, J. J. Dannenberg, S. Dapprich, A. D. Daniels, Ö. Farkas, J. B. Foresman, J. V. Ortiz, J. Cioslowski and D. J. Fox, *Gaussian 09, revision a.1*, Gaussian, Inc.: Wallingford CT, 2009.

39 P. Hohenberg and W. Kohn, *Phys. Rev.*, 1964, **136**, B864.

40 A. D. Becke, *Phys. Rev. A: At., Mol., Opt. Phys.*, 1988, **38**, 3098.

41 C. Lee, W. Yang and R. G. Parr, *Phys. Rev. B: Condens. Matter Mater. Phys.*, 1988, **37**, 785.

42 S. H. Vosko, L. Wilk and M. Nusair, *Can. J. Phys.*, 1980, **58**, 1200.

43 J. Guthmuller, *J. Chem. Theory Comput.*, 2011, **7**, 1082.

44 R. Krishnan, J. S. Binkley, R. Seeger and J. A. Pople, *J. Chem. Phys.*, 1980, **72**, 650.

45 M. Burkatzki, C. Filippi and M. Dolg, *J. Chem. Phys.*, 2007, **126**, 234105.

46 S. A. Serapian, M. J. Bearpark and F. Bresme, *Nanoscale*, 2013, **5**, 6445.

47 E. Runge and E. K. U. Gross, *Phys. Rev. Lett.*, 1984, **52**, 997.

48 J. Guthmuller and B. Champagne, *J. Chem. Phys.*, 2007, **127**, 164507.

49 T. Petrenko and F. Neese, *J. Chem. Phys.*, 2007, **127**, 164319.

50 M. Thomas, F. Latorre and P. Marquetand, *J. Chem. Phys.*, 2013, **138**, 044101.

51 E. J. Heller, R. Sundberg and D. Tannor, *J. Phys. Chem.*, 1982, **86**, 1822.

52 M. Wächtler, J. Guthmuller, L. González and B. Dietzek, *Coord. Chem. Rev.*, 2012, **256**, 1479.

53 J. Guthmuller, B. Champagne, C. Moucheron and A. Kirsch De Mesmaeker, *J. Phys. Chem. B*, 2010, **114**, 511.

54 J. Guthmuller and L. González, *Phys. Chem. Chem. Phys.*, 2010, **12**, 14812.

55 F. Hirshfeld, *Theor. Chim. Acta*, 1977, **44**, 129.

56 J. P. Ritchie, *J. Am. Chem. Soc.*, 1985, **107**, 1829.

57 J. P. Ritchie and S. M. Bachrach, *J. Comput. Chem.*, 1987, **8**, 499.

58 I. Kamiya, H. Tsunoyama, T. Tsukuda and H. Sakurai, *Chem. Lett.*, 2007, **36**, 646.

59 M. Stratakis and H. Garcia, *Chem. Rev.*, 2012, **112**, 4469.

60 J. P. Merrick, D. Moran and L. Radom, *J. Phys. Chem. A*, 2007, **111**, 11683.

61 K. Esperdy and D. D. Shillady, *J. Chem. Inf. Comput. Sci.*, 2001, **41**, 1547.

62 J. L. Payton, S. M. Morton, J. E. Moore and L. Jensen, *Acc. Chem. Res.*, 2014, **47**, 88–99.

This journal is © the Owner Societies 2015

Phys. Chem. Chem. Phys., 2015, **17**, 7648–7658 | **7657**

63 S. Mukherjee, F. Libisch, N. Large, O. Neumann, L. V. Brown, J. Cheng, J. B. Lassiter, E. A. Carter, P. Nordlander and N. J. Halas, *Nano Lett.*, 2013, **13**, 240.

64 M. W. Knight, Y. Wang, A. S. Urban, A. Sobhani, B. Y. Zheng, P. Nordlander and N. J. Halas, *Nano Lett.*, 2013, **13**, 1687.

65 F. Negri, C. Castiglioni, M. Tommasini and G. Zerbi, *J. Phys. Chem. A*, 2002, **106**, 3306.

66 J. R. Lombardi and R. L. Birke, *J. Phys. Chem. C*, 2008, **112**, 5605.

67 M. Thomas, S. Mühlig, T. Deckert-Gaudig, C. Rockstuhl, V. Deckert and P. Marquetand, *J. Raman Spectrosc.*, 2013, **44**, 1497.

68 R. Stowasser and R. Hoffmann, *J. Am. Chem. Soc.*, 1999, **121**, 3414.

4.3 Spatial Resolution of Tip-Enhanced Raman Spectroscopy - DFT Assessment of the Chemical Effect

Spatial resolution of tip-enhanced Raman spectroscopy – DFT assessment of the chemical effect†

Federico Latorre,[a] Stephan Kupfer,*[a] Thomas Bocklitz,[a,b] Daniel Kinzel,[a] Steffen Trautmann,[b] Stefanie Gräfe[a] and Volker Deckert*[a,b]

Experimental evidence of extremely high spatial resolution of tip-enhanced Raman scattering (TERS) has been recently demonstrated. Here, we present a full quantum chemical description (at the density functional level of theory) of the non-resonant chemical effects on the Raman spectrum of an adenine molecule mapped by a tip, modeled as a single silver atom or a small silver cluster. We show pronounced changes in the Raman pattern and its intensities depending on the conformation of the nanoparticle–substrate system, concluding that the spatial resolution of the chemical contribution of TERS can be in the sub-nm range.

1. Introduction

Improving spatial resolution is a major driving force for the development of microscopic techniques.[1–6] In addition to the well-known fluorescence based methods, such as stimulated-emission-depletion (STED),[1] photoactivated localization microscopy (PALM)[2] and stochastic optical reconstruction microscopy (STORM),[3] techniques based on near-field optics are capable of obtaining resolutions far beyond the diffraction limit.[4–6] Plasmon-based systems are particularly successful in this respect, where a nanoscale plasmonic object confines the electromagnetic field and at the same time enhances the signal.[7–15] Such systems are especially useful when fluorescence labeling cannot be used and intrinsic molecular information is required. The best known techniques based on plasmonic enhancement are surface and tip-enhanced Raman scattering (SERS and TERS, respectively)[16–18] as well as tip enhanced infrared absorption (TEIRA).[19,20] Signal enhancements observed in these techniques can be rationalized by two phenomena: the electromagnetic effect[8,21–28] and the chemical effect.[8,9,29–32] The former corresponds to the creation of a locally confined strong electric field by an incident light source, *i.e.* a plasmon, on a metallic cluster leading to a pronounced increase in the corresponding Raman signals of a substrate near the metal. The latter chemical effect is correlated to the interactions between molecules and metallic clusters and can be divided into three different contributions: ground state interactions between substrate and nanoparticle (non-resonant contribution), resonant enhancements of local (molecule) excitations (resonant contribution), and the emergence of new charge transfer states between the substrate and the nanoparticle (charge-transfer contribution).[8,9,33,34] These three contributions can lead to changes in the shape, spectral position and intensity of Raman bands due to changes in the local environment of the substrate under investigation.[22]

Interestingly, several recent TERS experiments have strongly indicated spatial resolutions of 1 nm or smaller (*i.e.*, single molecule resolution).[35–41] Such high resolutions are unexpected considering the dimensions of the commonly used plasmonic nanoparticles.[42,43] While a high resolution was predicted by Elfick and coworkers for tips with radii of 1 nm,[44] this tip size is generally difficult to achieve, and radii of 10–20 nm are considered more realistic.[45–48]

Recently, Aizpurua *et al.* and Sánchez-Portal *et al.* presented full quantum electrodynamic descriptions of plasmonic cavities, demonstrating the resolution capabilities of plasmonic nanoparticles due to extremely confined enhanced fields that can explain sub-nanometer resolution *via* the atom-scale features of small metal clusters.[49,50] Recent work on the resolution of TERS mapping, where mainly electromagnetic effects are discussed,[23] suggest that the confinement of the electric field near a tip is even more pronounced than expected due to the enhanced field-interaction with the (induced) dipole of the molecule. Moreover, the electric field gradient and its impact on the sub-nanometer spatial resolution[40,41,51] was evaluated theoretically[52] and experimentally.[53]

[a]Institute of Physical Chemistry and Abbe Center of Photonics, Friedrich-Schiller-University Jena, Helmholtzweg 4, 07743 Jena, Germany.
E-mail: stephan.kupfer@uni-jena.de, volker.deckert@uni-jena.de
[b]Leibniz Institute of Photonic Technology, Albert-Einstein-Str. 9, 07745 Jena, Germany
†Electronic supplementary information (ESI) available. See DOI: 10.1039/c6nr00093b

Quantum mechanical investigations studying the electromagnetic effects of plasmons on the Raman scattering process of a molecule in the vicinity of a metal nanoparticle have been performed by Jensen *et al.* who introduced a computational methodology to study plasmonic field effects on a substrate in the scope of SERS by means of a hybrid method combining atomistic electrodynamics and quantum mechanics.[48,54] Another approach by Dong *et al.* presents a quantum mechanical description of the interaction between the molecule and the metal tip, treated as a highly confined plasmonic field, using an electric field function.[55]

In contrast to the work of Aizpurua, Jensen and Dong, we will focus exclusively on the non-resonant chemical contributions to the signal enhancement/changes in TERS. We present the results of purely quantum chemical calculations based on density functional theory (DFT) to evaluate the spatial resolution of a metal tip acting on adenine by investigating the effect of minute lateral variations of the tip with respect to an individual sample molecule. Such position effects are generally not considered in the estimation of the chemical effects in SERS because a thermodynamically governed association of the metal particle and molecule (therefore, an optimized minimum energy geometry) can be assumed. However, in a TERS experiment, this assumption is not necessarily valid: the sample molecules are generally immobilized on a surface and, thus, cannot select specific sites on the plasmonic tip, allowing energetically unfavored conformations.

Adenine-silver nanoparticle interactions have already been the subject of several investigations of both experimental and theoretical studies using SERS[56–59] and TERS.[56,60–62] Here, we theoretically investigate "forced" tip-molecule conformations that can only be formed under TERS conditions and study the effects of such geometries on the Raman spectra with respect to the lateral resolution. This is intriguing because the specific local placement of a metal atom or metal cluster (as provided by the placement of the metal tip) with respect to a molecule can be considered a new unique molecule with specific and characteristic vibrational modes. In addition to the investigation of the lateral positioning, we also study the influence of the longitudinal metal-molecule distance. This is of specific interest for TERS experiments because the tip-sample distance is a crucial parameter that determines signal enhancement. Additionally, the investigation of tip-sample distance will provide an estimate of when the chemical effects start to play a major role. Thus, the quantum chemical calculations aim to unravel tip-sample interactions on a molecular scale and provide further spectral information due to non-resonant chemical effects.

Last but not least, a comparison between the effects of a single metal atom and a 20-atom metal cluster mimicking a metal tip will be shown, providing insight into second layer effects, *e.g.*, how strongly the atoms "behind" the front-most atom influence the molecular structure and consequently the vibrational spectra.

2. Computational details

Two models have been utilized to simulate the interactions between one adenine molecule and a silver tip: (i) mimicking the tip using a single silver atom and (ii) describing the metal tip as a small, tetrahedral cluster consisting of 20 silver atoms. Although the description of a metal tip as merely one silver atom might seem too be oversimplified, experiments indicate that, even for typical tip radii of approximately 10–20 nm, the very top of the tip seems to consist of a single atom.[45–48,50] Nevertheless, many effects are neglected in model (i), and model (ii) includes the effects of the second layer of atoms.

All quantum chemical calculations were performed using the Gaussian 09 program.[63] The planar adenine molecule, pre-optimized at the DFT level of theory using the range-separated CAM-B3LYP XC functional[64] and the 6-311+G(d,p) triple-ζ basis set,[65] was aligned within the *xy*-plane as depicted in Fig. 1(a).

The silver tip – represented by either a single silver atom (model i) or a silver cluster comprised of 20 atoms (model ii) – was placed on top of the adenine and moved in a grid of 6.5 Å by 5.5 Å with a step size of 0.5 Å, leading to a total of 168 grid points, as depicted in Fig. 1, per layer (*z*-coordinate). The interactions of the "tip" approaching the adenine were simulated for layers of *z* = 10, 8, 6, 5, 4, 3, and 2.5 Å; only the three layers of *z* = 10, 4, and 2.5 Å are discussed in detail.

For all calculations where the tip was modeled by one silver atom (model i) in Fig. 1(b), a complete quantum mechanical description was used, which consequently leads to a doublet ground state. Single point calculations with the same XC functional and basis set and subsequent vibrational analyses for the aforementioned layers have been performed. For the silver, the MWB28 relativistic core potential[66] was applied, where the inner shells are described by an effective core potential and the valence electrons (4s, 4p, 4d and 5s) explicitly with double-ζ quality. With respect to a realistic TERS setup with a substrate anchored parallel to a surface, and thus aligned in the *xy*-plane, the TERS signal is mainly obtained in the *z*-direction. Therefore, only the α_{zz}-component of the polarizability tensor would be subjected to electromagnetic enhancement; thus, the Raman intensity I_l of the *l*th vibrational normal mode is proportional to the absolute square of the derivative of α_{zz} with respect to the normal coordinate (q_l):

$$I_l \propto \left| \frac{\partial \alpha_{zz}}{\partial q_l} \right|^2. \tag{1}$$

The silver cluster (model ii) was oriented perpendicular to the *xy*-plane, while the vertex was placed accordingly on the grid (Fig. 1). Consequently, due to the even number of silver atoms, the singlet ground state was calculated for this model. As in the previous model (i), α_{zz} was obtained by frequency calculations, and again, the relative Raman intensity of the *l*th mode is given by eqn (1).

To correct for the lack of anharmonicity and the approximate treatment of electron correlation, all vibrational frequencies were scaled by a factor of 0.95[67] for both model (i) and model (ii) and broadened by Lorentzian functions with
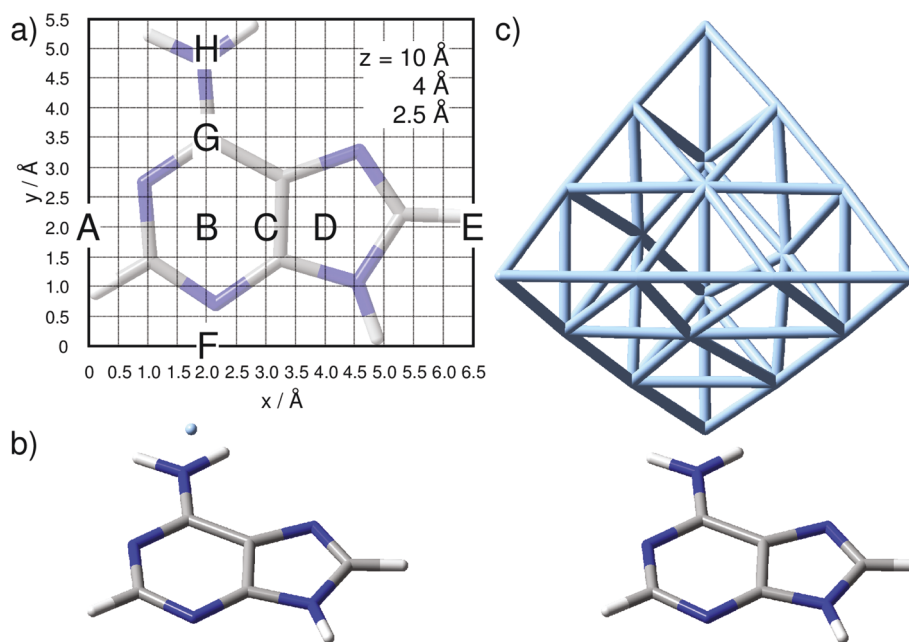
Fig. 1 (a) Adenine orientation and computational grid of 6.5 Å times 5.5 Å and with a step size of 0.5 Å as used in the quantum chemical simulations. Tip positions labeled **A–H** are discussed in detail. Tip modeled by (b) one silver atom and (c) a tetrahedral cluster comprising 20 silver atoms.

a full width at half maximum (FWHM) of 15 cm^{-1} to yield the Raman spectra. In order not to increase the computational demand of the grid calculations further, substrate-molecule interactions were not taken into account in this study. Such a simplification of the model system is valid in case of non-plasmonic surfaces that feature only weak chemical interactions at the substrate-molecule interface (*e.g.* mica). Furthermore, considering the uniform, specific substrate-molecule binding situation to be either unchanged or constant during the tip scanning along the grid may lead to spectral variations, however, the lateral resolution would not be decreased by including the substrate into the calculations.

To identify similar groups of TERS spectra within one layer, that is, the spatial resolution, statistical analysis of all computed spectra has been performed using the statistical language R.[68] In order to estimate such groups in the TERS grid, a principal component analysis followed by a *k*-means cluster analysis was carried out. In order to estimate the number of predefined clusters, *e.g.*, the *k* value, vector normalization was performed, and the square root of the between-cluster variance and the total in-cluster variance was calculated. The fraction of the standard deviation (SD) between the clusters divided by the within-cluster SD of a layer was used as marker for the number of groups present in the dataset. The number of predefined clusters (*k*) was determined in such a way that the fraction of SD between the clusters and within-cluster SD was above 1, and the smallest possible *k* was chosen. The rationale behind this procedure is that the difference between the clusters should be higher than within the cluster, and therefore, the situation when there are equal differences was used to define *k*.

3. Results

3.1. One-silver-atom model

Starting from a distance of *z* = 10 Å between the silver atom and the molecular plane (*xy*-plane) of the pre-optimized adenine molecule, the Raman intensity pattern along the grid has been calculated for each vibrational normal mode using eqn (1). The simulated Raman spectra at 10 Å along the grid points share a uniform intensity pattern, which is almost identical to the *z*-polarized Raman spectrum of an isolated adenine molecule (see Fig. S1 in the ESI†). Reducing the *z*-distance to 8 Å and further to 6 Å does not affect the calculated polarizability derivatives significantly, and no pronounced spectral alterations are observed with respect to the previous layer. However, with the silver atom further approaching the molecular plane and reaching regions of chemical interaction, changes in the appearances of the Raman signals are expected. Indeed, a pronounced dependency of the Raman spectrum on the silver position is observed at 4 Å. While the silver induces only slight shifts of the vibrational frequencies (up to approximately 4 cm^{-1}), indisputable alterations of intensity ratios and, thus, unique spectral patterns are found with respect to the specific lateral position of the silver atom.

As found by Sun *et al.*, enhancement due to resonance of charge transfer states between the molecule and the metal tip may influence the Raman intensity pattern substantially,[33,34] therefore, we rule out such a potential resonance enhancement at an excitation wavelength of 532 nm by calculating (doublet) excited states of adenine with the converging silver atom based on TDDFT simulations (see Fig. S2 in the ESI† for details).

The following discussion focuses on the vibrational modes in the spectral range between 500 and 1700 cm^{-1}. This region comprises the C–H and N–H vibrational normal modes, which are predominately affected in TERS.[56,57,69] Hence, the integrated, or rather summed, signal intensity I of each grid-point (x, y, z) within this frequency range ($8 \leq l \leq 37$) is given by:

$$I \propto \sum_{l=8}^{37} \left| \frac{\partial \alpha_{zz}}{\partial q_l} \right|^2. \tag{2}$$

Based on this expression, the integrated signal amplification A is obtained by normalization with respect to the minimum intensity I_{min} of the layer at $z = 10$ Å:

$$A = \frac{I}{I_{min}} = \sum_{l=8}^{37} \frac{\left| \dfrac{\partial \alpha_{zz}}{\partial q_l} \right|^2}{\left| \dfrac{\partial \alpha_{min,zz}}{\partial q_l} \right|^2} \tag{3}$$

This site-specific intensity amplification for $z = 10$ Å is illustrated in Fig. 2(a).

As expected, the intensity is independent of the "tip" position at this distance because the molecule interacts only very weakly with the silver atom. Hence, a constant value of $A \approx 1$ is obtained along the grid. Lowering the silver atom to $z = 4$ Å, see Fig. 2(b), results in an average signal amplification of approximately 5.6 along the grid. However, locally, an amplification of up to 10.6 and 17.9 is observed for the tip positions on top of the C–H bonds of the pyrimidine and the imidazole moieties. Moving the silver atom closer to the molecular plane, *i.e.*, to $z = 2.5$ Å, amplifies the integrated signal to an average value of 95.8. Then, as illustrated in Fig. 2(c), the grid-points on top of the C–H bonds feature the highest signal amplifications of 631.8 (pyrimidine) and 553.2 (imidazole), while the overall intensity profile along the entire grid shows a more pronounced structure than the layer at 4 Å.

In order to study the tip-induced alterations in more detail, five silver positions along the central line of the purine fragment (position **A**, **B**, **C**, **D**, and **E**) and four positions along the pyrimidine-amino axis (position **F**, **B**, **G**, and **H**) have been
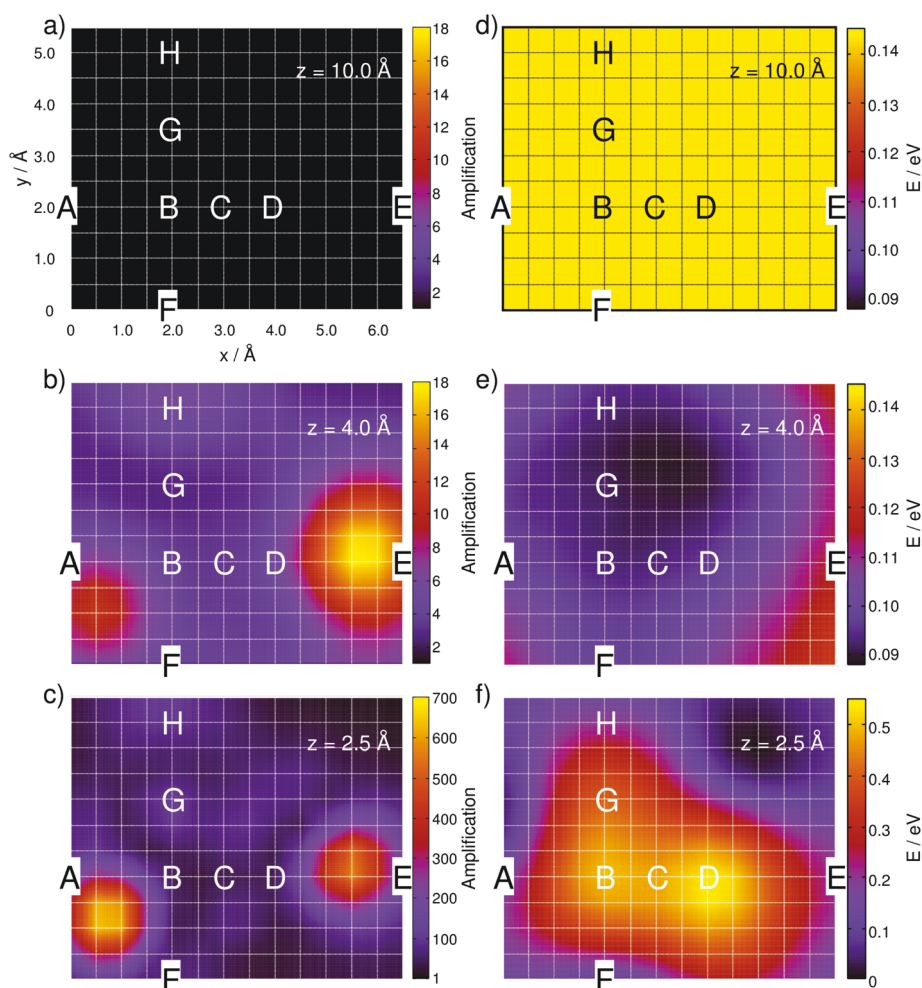

Fig. 2 Simulated integrated Raman signal amplification based on eqn (3) along the grid at (a) $z = 10$ Å, (b) 4 Å and (c) 2.5 Å for the one-silver-atom model. (d)–(f) illustrate the relative ground state potential energy surfaces (E in eV) of the respective layers. Notice the adjusted color bars scales for the amplification and energy in (c) and (f).

selected, see Fig. 1(a) for detailed positions. The point of intersection of both lines (**B**) is localized in the middle of the pyrimidine moiety. Selected spectra for each scan line at a height of $z = 4$ Å are shown in Fig. 3(a) and (b).

The Raman spectra along the purine line are dominated by intense in-plane C–H bending modes. While for **A** and **B**, the C–H mode of the pyrimidine moiety (975–980 cm^{-1}) shows the highest intensity, the spectra at **D** and **E** feature an intense C–H mode of the imidazole fragment (870–875 cm^{-1}), Fig. 3(a). Position **C** exhibits C–H modes of both the pyrimidine and the imidazole moieties; however, the intensity of the C–H bending mode of the imidazole (870–875 cm^{-1}) is considerably lower. Thus, position **C** can be addressed as a spectral intermediate of positions **A** and **E** or rather **B** and **D**.
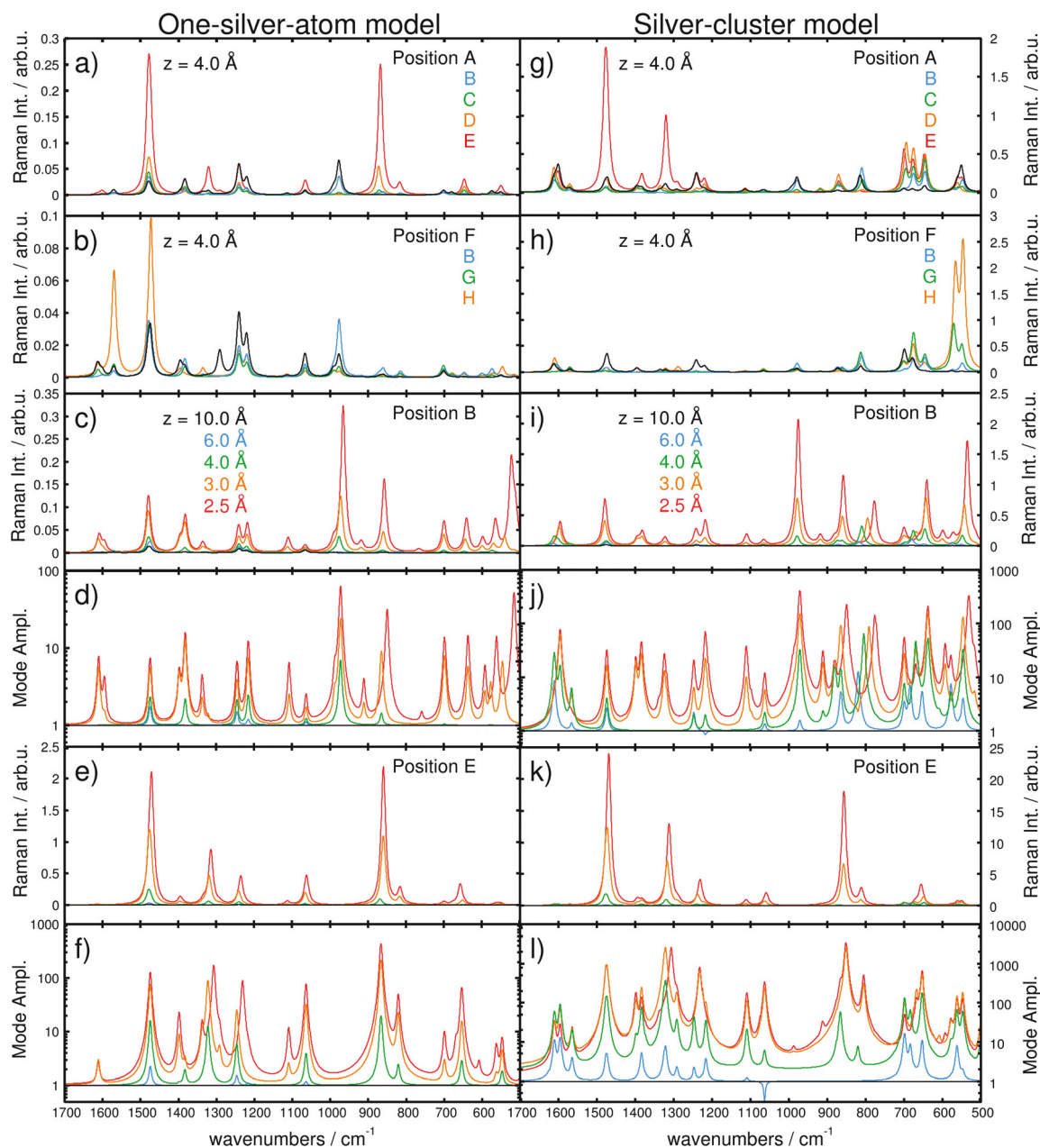
Fig. 3 Simulated Raman spectra based on the one-silver-atom model for (a) the purine line at $x = 2.0$ Å (**A**, **B**, **C**, **D**, and **E**) and (b) the pyrimidine-amino line at $y = 2.0$ Å (**F**, **B**, **G**, and **H**) and a z-distance of 4.0 Å. The z-dependencies are shown for positions **B** and **E** at 10.0, 6.0, 4.0, 3.0, and 2.5 Å in Raman intensity (in arb. u.) in (c) and (e) and in mode amplification in (d) and (f), respectively. Raman spectra based on the silver-cluster model are shown in (g) and (h) for the purin and the pyrimidine line, while (i) and (k) illustrate the z-dependency at **B** and **E** (Raman Intensity in arb. u.). Mode amplifications (A_I) in **B** and **E** are shown in (j) and (l). Vibrational normal modes were broadened by Lorentzians with a FWHM of 15 cm^{-1}. Note the different scales for models (i) and (ii).

In addition to the shape of the Raman pattern, a pronounced dependency with respect to the intensity or rather the mode amplification A_l is also observed, which is defined as:

$$A_l = \frac{I_l}{I_{l,\min}} = \frac{\left|\frac{\partial \alpha_{zz}}{\partial q_l}\right|^2}{\left|\frac{\partial \alpha_{\min,zz}}{\partial q_l}\right|^2}, \qquad (4)$$

where $I_{l,\min}$ is the respective mode intensity at $z = 10$ Å.

The positions **A–D** feature different spectral patterns, see Fig. 3(a), while further variations can be determined based on the maximal A_l values ranging from approximately 2.8 in **C** to 13 in **A** (all for $z = 4$ Å).

However, at **E** (above the hydrogen atom), the Raman spectrum exhibits even larger mode amplifications of up to approximately 20 (for $z = 4$ Å).

This finding is in accordance with the results illustrated in Fig. 2(b), where the highest signal amplifications are observed in the region of the C–H bonds close to the positions **A** and **E**. By examination of the underlying Raman spectra, it is evident that the enormous local amplification in the region of the C–H bonds is correlated to the intense C–H bending modes of the pyrimidine and the imidazole fragments.

Analogously, the spectra along the pyrimidine-amino line position (**F**, **B**, **G**, and **H**) show a pronounced dependency with respect to the tip position. At **F** and **H**, intense C–H (pyrimidine) and amino bending modes (1470–1475 cm^{-1}) dominate the pattern. Additionally, an intense characteristic N–H bending mode at approximately 1570 cm^{-1} is observed in **H**. The Raman spectra in **B** and **G** are of mixed character and feature characteristics of both **F** and **H**. Comparison of the spectra for these four positions, depicted in Fig. 3(b), yields a moderate mode amplification of merely 4.7 for **F**, 7.1 for **B** (explicitly shown in Fig. 3(c) and (d), and 2.4 for **G**, while **H** features values of $A_l \geq 13$ (all for $z = 4$ Å). Hence, the localization of the silver atom directly above a C–H (**E**) or N–H (**H**) bond induces a selective amplification of normal modes correlated to that specific position. Further convergence of the tip model towards the adenine (in the z-direction) substantially increases the interaction.

Consequently, the computed Raman spectra in each z-layer can be differentiated by means of the intensity pattern, and thus, by band shifts, deviations in the relative intensity, the absolute intensity and the mode amplification A_l. To further investigate the Raman signal with respect to the "tip" position, the dependency in the longitudinal z-coordinate was evaluated. The general behavior of the intensity as a function of the metal-molecule distance (z-coordinate) is illustrated in Fig. 3(c) and (e) for positions **B** and **E** at $z = 10.0$, 6.0, 4.0, 3.0, and 2.5 Å, respectively, while the mode amplifications are presented in Fig. 3(d) and (f). At 10.0 Å, the spectra in **B** and **E** are identical and dominated by intense C–H and N–H bending modes. Starting at 4 Å, alterations are induced by the silver atom (see differences in the mode amplification and in the spectra; green lines in Fig. 3(d) and (f) as well as 3(c) and (e),

respectively). At 3 Å, the spectrum in **B** is dominated by three intense CH/NH bending modes at 1490, 1390 and 980 cm^{-1}; at the same distance in **E**, the Raman intensity pattern features two intense modes at 1490 and 880 cm^{-1} (CH/NH bending), both at higher absolute intensities compared to **B**. Moving the tip closer to $z = 2.5$ Å – corresponding to a repulsive interaction (see Fig. 2(f) and S3(b)†) – substantially alters the intensity pattern in **B**. Now, the intense CH bending mode (880 cm^{-1}) is shifted by 12 cm^{-1} to lower frequencies, and an intense skeleton mode at 520 cm^{-1} emerges. In addition to the chemical shifts and the intensity pattern, the absolute intensity and, thus, the integrated amplification (eqn (3)) depend strongly on the "tip"-sample distance. Therefore, compared with 10 Å, distances of 8, 6, 5, 4, 3 and 2.5 Å have calculated amplification factors (A) of 1.1, 1.6, 2.2, 3.7, 14.8 and 34.4 for **B** and 1.2, 2.0, 3.8, 13.7, 83.9 and 165.3 for **E**, respectively.

By fitting the integrated intensity amplification A (eqn (3)) at position **B** along z to an exponential function, it is evident that the amplification decreases exponentially with the z-distance, see Fig. S3(a).†

The potential energy surface (PES) features attractive interactions of the silver atom and the adenine in the range of 6 to 3 Å, with the minimum at approximately 3.62 Å. At larger distances, the attractive interactions decay; therefore, the ground state energy increases towards the threshold of 0.06 eV. This trend is in agreement with the evolution of the amplification factors in the interval between 6 and 10 Å from 1.6 to 1.1 (8 Å) and 1.0 (Fig. S3a†). At small distances ($z < 3$Å), the PES is dominated by repulsive interactions and consequently increases to 0.06 and 0.41 eV at 3.0 and 2.5 Å, respectively.

In order to unravel the pronounced dependency of the Raman intensity on the silver atom position, 2D PESs of the electronic ground state are presented in Fig. 2 for the grids at 10, 4 and 2.5 Å, $i.e.$, in the long-range non-interactive region, close to the equilibrium distance and in the strongly repulsive region. As illustrated in Fig. 2(d) for the layer at $z = 10$ Å, an almost uniform energy landscape is obtained with deviations of less than 0.001 eV. Moving the silver atom to 4 Å induces pronounced alterations in the PES, as depicted in Fig. 2(e); these changes originate from attractive interactions between the silver and the molecule. Hence, in general, the energy of the system is stabilized, while the minimum energy at this layer is localized between the amino-group and the nearby nitrogen atom of the imidazole moiety, where a stabilization of approximately 0.05 eV is calculated with respect to the former layer (10 Å). By moving the silver atom even closer to 2.5 Å, strong repulsive interactions between the silver and the adenine are observed, which can be easily seen in Fig. 2(f). The strongest (repulsive) interactions are found at positions **B** (0.50 eV) and **D** (0.54 eV), $i.e.$, in the centers of the pyrimidine and the imidazole moieties. The global minimum energy is localized close to the non-protonated nitrogen of the imidazole; this grid point exhibits the lowest potential energy of all three layers depicted in Fig. 2(d)–(f).

To rationalize the local effects of the silver atoms on the Raman spectrum as well as on the potential energy landscape,

the electronic wave function and the frontier orbitals of the adenine and the silver are studied in detail. Due to the odd number of electrons of the silver atom ($4d^{10} \cdot 5s^1$), the electronic ground state of the adenine-silver system is a doublet, where the 5s orbital of the silver is occupied in α-spin but unoccupied in β-spin, also known as a semi-occupied molecular orbital (SOMO). The first orbital occupied in both α- and β-spin is the highest bonding π-orbital of the adenine. In order to study interactions among these orbitals, a linear combination of the π-orbital (adenine) and the 5s-orbital (silver) was created, where the positive combinations are denoted π(α) + s(α) and π(β) + s(β) and the negative ones π(α) − s(α) and π(β) − s(β); more details with respect to this linear combination can be found in Fig. S4.† Based on these four orbitals occupied by three electrons, a bond order of 0.5 is obtained. At z = 10 Å the positive and negative linear combinations are almost degenerate; however, with the tip converging towards the adenine, this degeneration becomes abrogated, which is shown in Fig. 4 for the positions **B** and **E** in the 4 Å layer.

It can be easily seen that the interaction of the 5s orbital with the π-system depends strongly on the silver atom position and eventually on the presence of a nodal plane between the silver and the adenine. For positions in the periphery of the molecule, e.g., in **E**, where the s-orbital of the silver interacts with the p-orbitals of the carbon atoms of the imidazole (see Fig. 4), only small interactions are observed. Here, a constructive overlap is obtained for the positive linear combination and a node for the negative linear combination. The orbital interactions in the center of the purine fragment are more complicated; constructive as well as destructive interactions are found for π + s as well as for π − s, as can be seen for position **B** in Fig. 4. Lowering the silver atom further towards the adenine consequently enhances the constructive and destructive orbital interactions. The spherical shape of the s-orbital

leads to a manifold of delocalized interactions with the π-orbital, especially in the center of the pyrimidine and the imidazole rings. Hence, in these regions, a bonding situation is unfavorable, which can also be seen in the high potential energies in **B** and **D** in Fig. 2(f).

To elucidate the resolution of a TERS experiment, where positioning accuracy is eventually limited by noise and drift in all three dimensions, a principal component analysis followed by a k-means cluster analysis was carried out using the computed z-polarized Raman spectra of the layers at 10.0, 4.0 and 2.5 Å. This analysis was done to account for averaging effects, which are expected due to the above-mentioned limitations of an actual experiment. The statistical analysis incorporates information with respect to the spectral pattern as well as with respect to the intensity. Fig. 5(a)–(c) illustrates these results for the aforementioned layers at 10.0, 4.0 and 2.5 Å.

Fig. 4 Constructed positive and negative linear combinations, π(β) ± s(β), of the highest occupied molecular orbital of the adenine and the 5s orbital of the silver atom with β spin for the positions **B** and **E** at z = 4 Å.
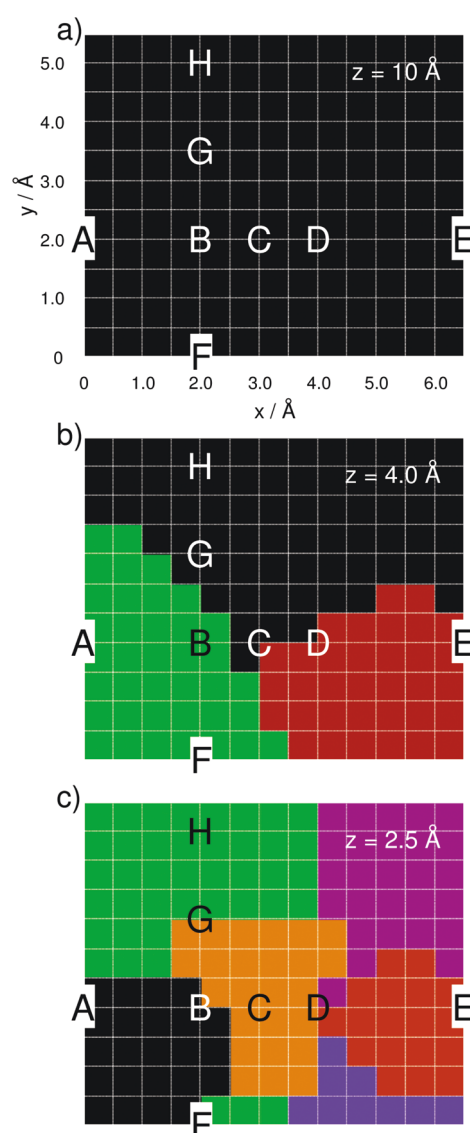
Fig. 5 Spectral groups along the computational grid for the layers of 10.0 (a), 4.0 (b) and 2.5 Å (c) as obtained by statistical analysis.

At $z = 10.0$ Å, the statistical analysis yields merely one spectral group, which corresponds to a uniform Raman pattern at this distance. Moving the silver atom to 4.0 and then to 2.5 Å yields three and six spectral groups, respectively. The average spectra within each spectral group are illustrated in Fig. S5 of the ESI.† The obtained spectral groups along the grid are in very good agreement with the computed amplifications of Fig. 2(a)–(c) and show that TERS with sub-nanometer resolution is possible depending on the distance between the tip and the substrate, even when considering noise and drift-induced variations of the actual tip position.

In the following section, the results obtained for the one-silver-atom model (i) will be compared to the enhanced silver-cluster model (ii).

3.2. Silver-cluster model

To verify the results obtained for the one-silver-atom model presented in section 3.1, as well as to investigate a dependency with respect to the tip size, pre-selected traces on the molecule as well as the entire layer at $z = 4$ Å have been calculated with the 20-silver-atom tip model. This model considers chemical effects of the silver atoms in the second, third and fourth layers of the tetrahedral cluster on the TERS signals. Analogous to section 3.1, we present the evolution of the z-polarized Raman signal for the 2D layer at 4 Å, while particular emphasis was set on the purine line (positions **A**, **B**, **C**, **D** and **E**) and on the pyrimidine-amino line (positions **F**, **B**, **G** and **H**). In addition, the z-dependency and, hence, the signal amplification in z, is evaluated at positions **B** and **E**.

First, the results on the z-dependency are presented. Calculations at $z = 10, 6, 4, 3$ and 2.5 Å were performed at **B** and **E**. The integrated amplification is defined using the intensity (see eqn (2)) divided by the intensity at $z = 10$ Å. A very similar behavior of the amplification with respect to z is obtained for both models. Interestingly, the amplification is even larger with the silver-cluster model. While, by definition, a value of $A = 1$ is obtained at 10 Å, upon approach, the amplification at position **B** increases to 5.1, 18.1, 51.8 and 105.1 at 6, 4, 3 and 2.5 Å, respectively, see Fig. S6(a).† At **E**, even larger amplifications of 7.7, 63.8, 363.1 and 747.0 (at 6, 4, 3 and 2.5 Å) are calculated, in accordance with the results obtained for the one-silver-atom model, where amplifications of 34.4 and 165.3 ($z = 2.5$ Å) were computed for **B** and **E**. Interestingly, the potential minimum and thus the bonding region of the cluster and the adenine is offset from 3.62 to 3.14 Å, while the bonding energy increased from 0.06 to 0.22 eV, see Fig. S6(b).†

Second, the dependency of the signal amplification as well as the spectral pattern along the purine and the pyrimidine-amino line at $z = 4$ Å is shown in Fig. 3(g) and (h). The z-polarized Raman spectra along the purine line [Fig. 3(g) **A**, **B**, **C**, **D** and **E**] feature similar intensities in **A** to **D**, while the intensity in **E** close to the imidazole C–H bond is substantially enhanced. Superficially, the spectra obtained with the silver-cluster model seem similar to the ones obtained with the one-silver-atom model. In accordance with the results obtained with the one-silver-atom model, the spectra in **A** and **B** are

dominated by intense in-plane modes localized on the C–H group of the pyrimidine but also on the C–H and N–H groups of the imidazole and the amino group. **E** features mainly intense in-plane (xy-polarized) C–H and N–H modes of the imidazole moiety at approximately 1300 and 1500 cm^{-1}, while **C** and **D** show contributions of all fragments and can be seen as spectral intermediates. In a similar manner, the spectra along the pyrimidine-amino line, see Fig. 3(h), are mainly dominated in **A** by C–H bending modes of the pyrimidine fragment and in **H** by N–H bending modes of the amino group polarized in the xy-plane, while the intermediate positions **B** and **G** show contributions from both functional groups. However, in contrast to the spectra in Fig. 3(a) and (b) (one-silver-atom model), all spectra calculated using the extended tip model have intense vibrational modes in the frequency range between 500 and 800 cm^{-1}. These modes have exclusively out-of-plane character (z-polarized), where the modes between 500 and 600 cm^{-1} are correlated to the amino-group, those between 600 and 700 cm^{-1} to C–H and N–H modes of the imidazole fragment and those at approximately 800 cm^{-1} to frame modes. Similar to the frequency range between 800 and 1700 cm^{-1}, modes localized close to the silver cluster are selectively increased, *i.e.*, in **H** (and **G**) very intense amino modes with mode amplifications, A_l, of up to 478.7 (and 131.8) are observed (500–600 cm^{-1}). In **C**, **D** and **E**, C–H and N–H modes of the imidazole fragment dominate the fingerprint region, where A_l values of up to 83.8, 119.2 and 200.0 were obtained, respectively (all for $z = 4$ Å).

The observed variations in the z-polarized Raman spectra with respect to the model size are predominantly accounted for by the amplification of all C–H and N–H out-of-plane modes with the silver cluster tip model. This is evident by comparing the amplifications at $z = 4$ Å for the one-silver-atom model and the silver-cluster model, see Fig. 2(b) and 6.

In order to unravel the impact of the tip model size on the out-of-pane modes, the "tip" must be examined more closely. Both the silver atom and the 20-silver-atom tetrahedron feature, independently of the grid point, overall charges of approximately −0.1 (Mulliken charge). However, the four vertex
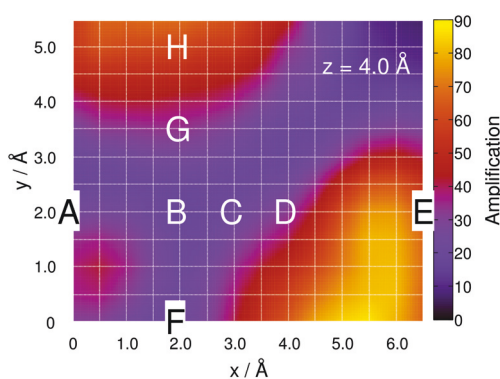

Fig. 6 Simulated Raman signal amplification based on eqn (3) along the grid at 4 Å for the silver-cluster model.

positions of the silver cluster hold pronounced negative charges. At $z = 10$ Å, all four vertices are degenerate and feature partial charges of approximately -1.6, whereas at shorter z-distance, e.g., at 4 Å, this degeneration is abolished. Here, the "tip"-atom (vertex towards the molecule) features charges of up to -2.0 for grid points above the purine moiety. Hence, this charge, or rather the charge gradient, along z induces distinct chemical effects that mainly affect the z-polarized C–H and N–H out-of-plane modes.

This phenomenon can also be observed by the evolution of the Raman intensity, or rather mode amplification, at positions **B** and **E** with respect to the "tip" convergence, as depicted in Fig. 3(i)–(l). The A_I values obtained using the silver-cluster model are larger than those obtained using the one-silver-atom model. This is especially evident at position **E**, where mode amplifications of up to approximately 3500 ($z = 2.5$ Å at 852 cm^{-1}) were obtained using the silver cluster, while amplifications of only approximately 450 ($z = 2.5$ Å at 865 cm^{-1}) were calculated for the one-silver-atom model.

4.   Conclusions

In the present contribution, the possibility of sub-nanometer-resolution in TERS has been investigated by means of quantum chemical simulations at the DFT level of theory of an adenine molecule-silver tip model system. Three-dimensional grid calculations were performed for two models in which the silver tip was approximated by one silver atom or by a tetrahedron comprised of 20 silver atoms. Both computational models suggest a hypothetical TERS resolution in the Ångström regime. Pronounced dependencies of the simulated Raman patterns and intensities on the tip model and its position were found. Mode amplifications of up to almost 3500 were computed based on the chemical interactions between the adenine and the silver tip. From an experimental point of view, a sub-Ångström resolution is unrealistic at the moment due to, e.g., tip positioning noise and thermal drift of the sample. Such effects would result in a decreased lateral resolution based on signal averaging. However, the lateral contrast obtained in recent TERS experiments using scanning probe systems with sub-nanometer stability can now be explained to a certain extent. It is important to note that external fields, particularly the field confinement due to plasmonic effects, were not considered here. Only the molecular properties of the silver-adenine system were accounted for, while locally confined inhomogeneous electromagnetic fields and strong field gradients may increase the lateral resolution even further. Still, a surprisingly strong enhancement of the signals due to polarizability changes was observed. At first glance, the strong dependence of the spectra towards the local position of the metal seems disturbing; however, this dependence mainly influences the intensity ratios rather than the band positions. Consequently, for an assignment to a specific structure, the actual band positions are of higher importance than their intensity ratios.

In summary, we think these findings will encourage further joint spectroscopic-theoretical investigations. In particular incorporating the plasmonic enhancement based on the interaction of the sample with the electric field and the electric field gradients, in the case of inhomogeneous fields, and chemical as well as chemical/plasmonic effects at the surface-substrate interface are envisioned in prospective studies.

Acknowledgements

References

1 S. Hell and J. Wichmann, *Opt. Lett.*, 1994, **19**(11), 780–782.
2 E. Betzig, G. H. Patterson, R. Sougrat, O. W. Lindwasser, S. Olenych, J. S. Bonifacino, M. W. Davidson, J. Lippincott-Schwartz and H. F. Hess, *Science*, 2006, **313**(5793), 1642–1645.
3 M. J. Rust, M. Bates and X. Zhuang, *Nat. Methods*, 2006, **3**(10), 793–796.
4 E. Betzig, J. K. Trautman, T. D. Harris, J. S. Weiner and R. L. Kostelak, *Science*, 1991, **251**(5000), 1468–1470.
5 E. J. Sánchez, L. Novotny and X. S. Xie, *Phys. Rev. Lett.*, 1999, **82**(20), 4014–4017.
6 J. Y. Lee, B. H. Hong, W. Y. Kim, S. K. Min, Y. Kim, M. V. Jouravlev, R. Bose, K. S. Kim, I.-C. Hwang, L. J. Kaufman, C. W. Wong, P. Kim and K. S. Kim, *Nature*, 2009, **460**(7254), 498–501.
7 M. Osawa, in *Near-Field Optics and Surface Plasmon Polaritons*, ed. S. Kawata, Topics in Applied Physics, Springer, Berlin Heidelberg, 2001, vol. 81, pp. 163–187.
8 S. M. Morton, D. W. Silverstein and L. Jensen, *Chem. Rev.*, 2011, **111**(6), 3962–3994.
9 L. Jensen, C. M. Aikens and G. C. Schatz, *Chem. Soc. Rev.*, 2008, **37**(5), 1061–1073.
10 D. Cialla, A. März, R. Böhme, F. Theil, K. Weber, M. Schmitt and J. Popp, *Anal. Bioanal. Chem.*, 2012, **403**(1), 27–54.
11 L. Tong, T. Zhu and Z. Liu, *Chem. Soc. Rev.*, 2011, **40**(3), 1296–1304.
12 S. Schlücker, *Angew. Chem., Int. Ed.*, 2014, **53**(19), 4756–4795.
13 E. Bailo and V. Deckert, *Chem. Soc. Rev.*, 2008, **37**(5), 921–930.
14 B. Pettinger, P. Schambach, C. J. Villagómez and N. Scott, *Annu. Rev. Phys. Chem.*, 2012, **63**(1), 379–399.

15 C. Blum, L. Opilik, J. M. Atkin, K. Braun, S. B. Kämmer, V. Kravtsov, N. Kumar, S. Lemeshko, J.-F. Li, K. Luszcz, T. Maleki, A. J. Meixner, S. Minne, M. B. Raschke, B. Ren, J. Rogalski, D. Roy, B. Stephanidis, X. Wang, D. Zhang, J.-H. Zhong and R. Zenobi, *J. Raman Spectrosc.*, 2014, **45**(1), 22–31.

16 R. M. Stöckle, Y. D. Suh, V. Deckert and R. Zenobi, *Chem. Phys. Lett.*, 2000, **318**(1–3), 131–136.

17 N. Hayazawa, Y. Inouye, Z. Sekkat and S. Kawata, *Opt. Commun.*, 2000, **183**(1–4), 333–336.

18 M. S. Anderson, *Appl. Phys. Lett.*, 2000, **76**(21), 3130–3132.

19 B. Knoll and F. Keilmann, *Nature*, 1999, **399**(6732), 134–137.

20 T. Taubner, F. Keilmann and R. Hillenbrand, *Nano Lett.*, 2004, **4**(9), 1669–1672.

21 N. Chiang, N. Jiang, D. V. Chulhai, E. A. Pozzi, M. C. Hersam, L. Jensen, T. Seideman and R. P. Van Duyne, *Nano Lett.*, 2015, **15**(6), 4114–4120.

22 M. Thomas, S. Mühlig, T. Deckert-Gaudig, C. Rockstuhl, V. Deckert and P. Marquetand, *J. Raman Spectrosc.*, 2013, **44**, 1497–1505.

23 C. Zhang, B.-Q. Chen and Z.-Y. Li, *J. Phys. Chem. C*, 2015, **119**(21), 11858–11871.

24 S. Corni and J. Tomasi, *J. Chem. Phys.*, 2001, **114**(8), 3739–3751.

25 S. Corni and J. Tomasi, *Chem. Phys. Lett.*, 2001, **342**(1–2), 135–140.

26 S. Corni and J. Tomasi, *J. Chem. Phys.*, 2002, **116**(3), 1156–1164.

27 S. Corni and J. Tomasi, *J. Chem. Phys.*, 2002, **117**(15), 7266–7278.

28 D. V. Chulhai and L. Jensen, *J. Phys. Chem. C*, 2013, **117**(38), 19622–19631.

29 L. Zhao, L. Jensen and G. C. Schatz, *J. Am. Chem. Soc.*, 2006, **128**(9), 2911–2919.

30 L. Jensen, L. L. Zhao and G. C. Schatz, *J. Phys. Chem. C*, 2007, **111**(12), 4756–4764.

31 S. Liu, X. Zhao, Y. Li, M. Chen and M. Sun, *Spectrochim. Acta, Part A*, 2009, **73**(2), 382–387.

32 F. Latorre, J. Guthmuller and P. Marquetand, *Phys. Chem. Chem. Phys.*, 2015, **17**(12), 7648–7658.

33 L. Xia, M. Chen, X. Zhao, Z. Zhang, J. Xia, H. Xu and M. Sun, *J. Raman Spectrosc.*, 2014, **45**(7), 533–540.

34 M. Sun, Y. Fang, Z. Yang and H. Xu, *Phys. Chem. Chem. Phys.*, 2009, **11**(41), 9412–9419.

35 R. Zhang, Y. Zhang, Z. C. Dong, S. Jiang, C. Zhang, L. G. Chen, L. Zhang, Y. Liao, J. Aizpurua, Y. Luo, J. L. Yang and J. G. Hou, *Nature*, 2013, **498**(7452), 82–86.

36 T. Deckert-Gaudig, E. Kämmer and V. Deckert, *J. Biophotonics*, 2012, **5**(3), 215–219.

37 P. Singh and V. Deckert, *Chem. Commun.*, 2014, **50**(76), 11204–11207.

38 J. M. Klingsporn, N. Jiang, E. A. Pozzi, M. D. Sonntag, D. Chulhai, T. Seideman, L. Jensen, M. C. Hersam and R. P. V. Duyne, *J. Am. Chem. Soc.*, 2014, **136**(10), 3881–3887.

39 S. Jiang, Y. Zhang, R. Zhang, C. Hu, M. Liao, Y. Luo, J. Yang, Z. Dong and J. G. Hou, *Nat. Nanotechnol.*, 2015, **10**(10), 865–869.

40 Y. Fang, Z. Zhang, L. Chen and M. Sun, *Phys. Chem. Chem. Phys.*, 2014, **17**(2), 783–794.

41 M. Sun, Z. Zhang, L. Chen, S. Sheng and H. Xu, *Adv. Opt. Mater.*, 2014, **2**(1), 74–80.

42 Z. Yang, J. Aizpurua and H. Xu, *J. Raman Spectrosc.*, 2009, **40**(10), 1343–1348.

43 A. Downes, D. Salter and A. Elfick, *J. Phys. Chem. B*, 2006, **110**(13), 6692–6698.

44 A. Downes, D. Salter and A. Elfick, *J. Microsc.*, 2008, **229**(2), 184–188.

45 Y. C. Martin, H. F. Hamann and H. K. Wickramasinghe, *J. Appl. Phys.*, 2001, **89**(10), 5774–5778.

46 P. I. Geshev, S. Klein, T. Witting, K. Dickmann and M. Hietschold, *Phys. Rev. B: Condens. Matter Mater. Phys.*, 2004, **70**(7), 075402.

47 I. Notingher and A. Elfick, *J. Phys. Chem. B*, 2005, **109**(33), 15699–15706.

48 J. L. Payton, S. M. Morton, J. E. Moore and L. Jensen, *Acc. Chem. Res.*, 2014, **47**(1), 88–99.

49 M. K. Schmidt, R. Esteban, A. Gonzalez-Tudela, G. Giedke and J. Aizpurua, 2015, arXiv:1509.03851 [physics.optics].

50 M. Barbry, P. Koval, F. Marchesin, R. Esteban, A. G. Borisov, J. Aizpurua and D. Sánchez-Portal, *Nano Lett.*, 2015, **15**(5), 3410–3419.

51 L. Meng, Z. Yang, J. Chen and M. Sun, *Sci. Rep.*, 2015, **5**, 9240–9244.

52 P. Knoll, M. Marchl and W. Kiefer, *Indian J. Pure Appl. Phys.*, 1988, **26**(2–3), 268–277.

53 E. J. Ayars, H. D. Hallen and C. L. Jahncke, *Phys. Rev. Lett.*, 2000, **85**(19), 4180–4183.

54 J. L. Payton, S. M. Morton, J. E. Moore and L. Jensen, *J. Chem. Phys.*, 2012, **136**(21), 214103.

55 S. Duan, G. Tian, Y. Ji, J. Shao, Z. Dong and Y. Luo, *J. Am. Chem. Soc.*, 2015, **137**(30), 9515–9518.

56 A. Rasmussen and V. Deckert, *J. Raman Spectrosc.*, 2006, **37**(1–3), 311–317.

57 R. Huang, H.-T. Yang, L. Cui, D.-Y. Wu, B. Ren and Z.-Q. Tian, *J. Phys. Chem. C*, 2013, **117**(45), 23730–23737.

58 T. A. Mohamed, I. A. Shabaan, W. M. Zoghaib, J. Husband, R. S. Farag and A. E.-N. M. A. Alajhaz, *J. Mol. Struct.*, 2009, **938**(1–3), 263–276.

59 B. Giese and D. McNaughton, *J. Phys. Chem. B*, 2002, **106**(1), 101–112.

60 H. Watanabe, Y. Ishida, N. Hayazawa, Y. Inouye and S. Kawata, *Phys. Rev. B: Condens. Matter Mater. Phys.*, 2004, **69**(15), 155418.

61 N. Hayazawa, H. Watanabe, Y. Saito and S. Kawata, *J. Chem. Phys.*, 2006, **125**(24), 244706.

62 K. F. Domke, D. Zhang and B. Pettinger, *J. Am. Chem. Soc.*, 2007, **129**(21), 6708–6709.

63 M. J. Frisch, G. W. Trucks, H. B. Schlegel, G. E. Scuseria, M. A. Robb, J. R. Cheeseman, G. Scalmani, V. Barone, B. Mennucci, G. A. Petersson, H. Nakatsuji, M. Caricato, X. Li, H. P. Hratchian, A. F. Izmaylov, J. Bloino, G. Zheng, J. L. Sonnenberg, M. Hada, M. Ehara, K. Toyota, R. Fukuda,

J. Hasegawa, M. Ishida, T. Nakajima, Y. Honda, O. Kitao, H. Nakai, T. Vreven, J. A. Montgomery Jr., J. E. Peralta, F. Ogliaro, M. Bearpark, J. J. Heyd, E. Brothers, K. N. Kudin, V. N. Staroverov, R. Kobayashi, J. Normand, K. Raghavachari, A. Rendell, J. C. Burant, S. S. Iyengar, J. Tomasi, M. Cossi, N. Rega, J. M. Millam, M. Klene, J. E. Knox, J. B. Cross, V. Bakken, C. Adamo, J. Jaramillo, R. Gomperts, R. E. Stratmann, O. Yazyev, A. J. Austin, R. Cammi, C. Pomelli, J. W. Ochterski, R. L. Martin, K. Morokuma, V. G. Zakrzewski, G. A. Voth, P. Salvador, J. J. Dannenberg, S. Dapprich, A. D. Daniels, Ö. Farkas, J. B. Foresman, J. V. Ortiz, J. Cioslowski and D. J. Fox, *Gaussian 09, Revision A.2*.

64 T. Yanai, D. P. Tew and N. C. Handy, *Chem. Phys. Lett.*, 2004, **393**(1–3), 51–57.

65 P. C. Hariharan and J. A. Pople, *Theor. Chim. Acta*, 1973, **28**(3), 213–222.

66 D. Andrae, U. Häußermann, M. Dolg, H. Stoll and H. Preuß, *Theor. Chim. Acta*, 1990, **77**(2), 123–141.

67 NIST Computational Chemistry Comparison and Benchmark Database, NIST Standard Reference Database Number 101 Release 17b, September 2015, Editor: Russell D. Johnson III http://cccbdb.nist.gov/.

68 R Development Core Team, *R: A Language and Environment for Statistical Computing*, the R Foundation for Statistical Computing, Vienna, Austria, 2011, ISBN: 3-900051-07-0. Available online at http://www.R-project.org/.

69 M. D. Sonntag, D. Chulhai, T. Seideman, L. Jensen and R. P. Van Duyne, *J. Am. Chem. Soc.*, 2013, **135**(45), 17187–17192.

Contributions to the appended publications

1. Thomas, M., <u>Latorre, F.</u>, and Marquetand P.
   Resonance Raman spectra of ortho-nitrophenol calculated by real-time time-dependent density functional theory
   J. Chem. Phys. **138**, 044101 (2013)

   I contributed to this article was to perform the quantum chemical calculations for the vibronic theory and dynamic polarizabilities method and I helped in writing the computational setup of the manuscript. Martin Thomas performed all quantum chemical calculations of the real-time method, the analysis of the results of all three methods and wrote the initial draft of the manuscript. Philipp Marquetand conceived and supervised the quantum chemical calculations and finalized the manuscript. [1.0]

2. <u>Latorre, F.</u>, Guthmuller, J., and Marquetand, P.
   Resonance Raman combined with nanoparticles as a tool for distinguishing the two isomers of penta-2,4-dienoic acid
   Phys. Chem. Chem. Phys. **1**,7 7648-7658 (2015)

   My contribution to this publication by performing all quantum chemical calculations, the analysis of the results, the simulation of infrared, Raman, absorption and resonance Raman spectra and I helped writing the manuscript. Julien Guthmuller assisted with his expertise during the analysis of the results and supervised the quantum chemical calculations. Philipp Marquetand conceived and supervised the theoretical work and wrote the manuscript. [1.0]

3. <u>Latorre, F.</u>, Kupfer, S., Bocklitz, T., Kinzel, D., Trautmann, S., Gräfe, S., and Deckert, V.
   Spatial Resolution of Tip-Enhanced Raman Spectroscopy - DFT Assessment of the Chemical Effect
   Nanoscale **6**, 10229-10239 (2016)

   I contributed by performing all quantum chemical calculations, their analysis and the writing of the writing of the manuscript. Stephan Kupfer guided the quantum chemical calculations, participated in the analysis of the spectra and the writing of the manuscript. The statistical analysis was performed by Thomas Bocklitz, nd the corresponding part of the manuscript were performed by Thomas Bocklitz. Daniel

Chapter 5

Summary

Upon the discovery of the Raman effect in 1928 a manifold of techniques that utilize this effect have been established in vibrational spectroscopy. However, standard Raman spectroscopy features a major drawback, which is its low sensitivity. Therefore, several methods have been developed to overcome this shortcoming. Among the most prominent ones are resonance Raman (RR) which enables a signal enhancement by a factor of 10^2 up to 10^6 by virtue of a resonance of the incidental light with a (bright) electronic excited state of the chemical system of interest. Furthermore, plasmonic resonance can increase the Raman signal drastically (up to $10^6 - 10^8$), such plasmon enhancement is the keystone of surface enhanced Raman scattering (SERS) and tip-enhanced Raman scattering (TERS). Despite the fact that plasmon-enhanced Raman spectroscopy, i.e. SERS and TERS, are widely used tools in modern vibrational spectroscopy, the fundamental physical principles are far from being understood. Therefore, the present thesis aims to shed light on SERS and TERS spectroscopy, especially on the chemical effect of both spectroscopic techniques.

The chemical effect in SERS and TERS can be explained by three different contributions: the non-resonant, the charge transfer and the resonant term. The first contribution, the non-resonant term, can be rationalized by the same process as Raman scattering (RS), while the second one, charge transfer, originates from the interaction between the metal nanoparticle and the sample, and while the latter, resonant contribution, can be described by virtue of RR scattering.

Prior to this thesis, Chen et al. developed a method that combines classical electrodynamics and quantum chemistry to model the electromagnetic as well as chemical enhancement to evaluate SERS spectroscopy. The real time-time dependent density function theory (RT-TDDFT) method is used for the quantum-chemical part, while Mie theory is used to model the electromagnetic enhancement produced by the surface of an

homogeneous spherical nanoparticle.

In this thesis a novel approach to simulate RR scattering, called the real time (RT) method, has been introduced. This method is based on the methodology developed by Chen et al., but neglects the electromagnetic enhancement, resulting in a new approach utilizing RT-TDDFT to calculate the polarizabilty tensor within time domain, in contrast to other methods which employ the frequency domain. The RT method was benchmarked by evaluating the RR spectrum of *ortho* - Nitrophenol against two well-known methods, namely the vibronic method (within the short-time approximation) and the dynamic polarizability method. The comparison of the obtained RR spectra allowed an unbiased validation of the RT approach. Therefore, the RT method provides a new alternative to simulate resonance Raman intensities, while this method was originally developed in the scope of SERS or rather SER(R)S.

While the latter study gave an insight into RR scattering, in order to achieve a proper understanding of the chemical effect in SERS it is necessary to model the sample and nanoparticle with quantum chemical tools. For this purpose a computational study focused on the discrimination between the isomers of a small photo induced switch attached to gold nanoclusters of different size using various spectroscopic techniques (IR, RS, UV and RR scattering) has been presented in this thesis. The penta-2,4-dienoic acid (PDAH) molecule was chosen because of its light triggered *cis/trans* isomerization of the double bond. Therefore, with this system it was possible to study the chemical interactions between the PDAH with the gold nanoclusters and how the chemical effect evolves with the size of the nanoparticle.

IR absorption and RS allowed to investigate equilibrium structures of both isomers as well as the structural variations of PDAH induced by small gold clusters, while surface and vertex anchoring orientations were also taken into account. Thus, the influence of surface defects in SER(R)S was investigated by means of the chemical effect (exclusively). It was shown that in the ground state, the interaction between PDAH and the gold clusters led to a partial enolisation of the two isomers, which affects the intensity pattern of IR and RS spectra. This enolisation is more pronounced for larger gold clusters, however, the respective *cis* and *trans* isomers show very similar spectra.

In the excited state, the PDAH-Au interaction led to a mixing between PDAH IL states and MC states of the Au_{20} cluster. This trend increases with the size of the gold nanocluster. Additionally, the *cis* isomer showed less mixed IL states than the *trans* isomer on the Au_{20} systems. This difference in the mixing of the IL states between both isomers affects the way that the normal modes related to the double bonds of the PDAH molecule are activated in the RR spectra. Consequently, the RR spectroscopy

stands out as a suitable tool for the discrimination of the PDAH isomers attached to gold nanoparticles. Also, the natural high spectral resolution that the RR spectrum features helped to have a clearer distinction between the spectra of both isomers.

It was also shown how the PDAH orientation on Au_{20}, e.g. vertex and surface, resulted in different spectra. These spectral variations are caused by distinct chemical interaction, and thus, showing how defects on real surfaces can affect the overall SER(R)S spectra. While in this thesis the chemical effect of the SERS spectroscopy was studied, in general the electromagnetic effect has to be evaluated and added to the chemical effect. The Mie theory cannot be used because it is limited to model homogeneous spherical nanoparticles. To study how surface defects affect the overall SERS signal an alternative method to describe the electromagnetic properties of in-homogeneously shaped nanoparticles has to be used, e.g. the finite element method (FEM).

Hence, it was shown that SER(R)S can be utilized in order to distinguish between the (surface immobilized) *cis* and *trans* isomers of PDAH. These results clearly indicate that SER(R)S is a powerful spectroscopic technique to study materials such as smart surfaces, which consist of photoswitchable molecules anchored on a conductive surface, i.e. metal nano-clusters.

Recently TERS has gained special attention in the scientific community because of its high spatial resolution that permits to study single molecule samples or to map molecules. Like in SERS, TERS can be explained by an electromagnetic and a chemical effect that are analogue to SERS. Therefore, the models and level of theory used to study SERS can be accommodated to study the fundamental principles of TERS.

In this thesis, the lateral resolution of TERS was studied by simulating exclusively the chemical effect in TERS. Here, an adenine molecule was mapped by a silver tip, using a similar level of theory that was used before for RR and SERS. For the study of the lateral resolution on TERS, a 3D grid was spanned on top of the adenine molecule oriented flat on a fictional surface. With this computational set up, the adenine molecule is aligned in the xy-plane, consequently the TERS signal is mainly obtained in z-direction and the Raman intensity was evaluated with respect to $|\alpha_{zz}|^2$. The silver tip was modeled by a single Ag atom or by a Ag_{20} nanocluster. While the former model approximates the silver atom of the tip that directly interacts with the adenine molecule, the latter model incorporates effects of further atomic layers layers within the tip.

Both models suggested a hypothetical TERS resolution in the Ångström regime. Pronounced dependencies of the simulated Raman patterns and intensities on the tip model and its position were found. Mode amplifications of up to almost 3500 were computed based on the chemical interactions between the adenine and the silver tip. From an ex-

perimental point of view, a sub-Ångström resolution is unrealistic at the moment due to several factors (tip positioning noise and thermal drift of the sample). These factors would decrease the calculated lateral resolution based on signal averaging. However, the lateral contrast obtained in recent TERS experiments using scanning probe systems with sub-nanometer stability can be explained to a certain extent with the results presented in this thesis.

At first glance, it can be thought that the strong dependence of the spectra on the local position of the metal seems disturbing and it will have direct impact on the band positions and thus in the molecular fingerprint. However, this dependence mainly influences the intensity ratios rather than the band positions. Consequently, for an assignment to a specific structure, the actual band positions are of higher importance than the actual intensity ratios.

In summary, this thesis studied state-of-the-art signal-enhanced Raman spectroscopy techniques, i.e. RR, SERS and TERS, using quantum chemical methods. In SERS and TERS the focus was the chemical effect and it was studied in detail. Our computational approach allowed to investigate the chemical effect on a molecular level and this way gave insight into the fundamental (photo)physical principles of plasmon-enhanced Raman spectroscopy. Most strikingly, the potential subnanometer resolution in TERS was for the first time explained, to the best of our knowledge, based on a solely quantum mechanical approach.

Kapitel 6

Zusammenfassung

Die vorliegende Dissertation beschäftigt sich allgemein mit Licht-Materie-Wechselwirkung und genauer gesagt mit der inelastischen Streuung von elektromagnetischer Strahlung an kleinen organischen Molekülen; Namensgeber dieses Effektes war Sir C. V. Raman, der diesen 1928 beschrieb. Seit dieser Zeit hat sich eine große Bandbreite schwingungs-spektroskopischer Methoden entwickelt, die sich diesen Raman-Effekt zu Nutze macht. Diese Methoden werden allgemein unter dem Begriff der Raman-Spektroskopie zusammengefasst. Ein grundlegendes Problem der Raman-Spektroskopie ist allerdings deren geringe Sensitivität. Dies resultiert aus der Tatsache, dass ein Großteil der wechselwirkenden Photonen nicht inelastisch, sondern elastisch gestreut wird. Bei diesem als Rayleigh-Streuung bezeichneten Prozess kommt es nicht zu einer Energieübertragung auf die Materie und somit wird keine schwingungsspektroskopische Information erhalten. Daher wurde eine Vielzahl von Methoden entwickelt um die Raman-Signalintensität zu steigern. Zu den prominentesten Vertretern dieser Verfahren gehört die Resonanz-Raman-Spektroskopie, kurz RR-Spektroskopie, sowie die oberflächenverstärkte und die spitzen-verstärkte Raman-Spekroskopie (SERS und TERS). Trotz der Tatsache, dass SERS und TERS, oder allgemein plasmonenverstärkte Raman-Spektroskopie, heutzutage zu weit-verbreiteten Verfahren, unter anderem in der Strukturaufklärung von Enzymen, gehören, sind die zugrundeliegenden physikalischen Prinzipien noch nicht vollkommen verstanden. Die vorliegende Arbeit beschäftigt sich vornehmlich mit der chemischen Wechselwirkung von plasmonisch-aktiven Nanopartikeln und kleinen organischen Molekülen im Hinblick auf SERS und TERS, wobei Effekte des durch den Nanopartikel verstärkten Feldes bzw. Feldgradienten, welche zur Signalverstärkung ebenso beitragen, hier nicht berücksichtigt wurden.

Ausgangspunkt für die vorliegende theoretische Arbeit stellt eine neuartige Möglichkeit zur Beschreibung der RR-Spektroskopie dar. Diese sogenannte RT(Echtzeit)-Methode ba-

siert auf der von Chen et al. entwickelten Methodik zur Simulation von SERS-Spektren und berechnet im Gegensatz zu Standardverfahren die zeitliche Entwicklung des Polarisierbarkeitstensors in Abhängigkeit des zeitabhängigen externen elektrischen Feldes direkt in der Zeitdomäne und verzichtet auf einen Wechsel in die Frequenzdomäne. Dies wird mittels der Echtzeit zeitabhängigen Dichtefunktionaltheorie (RT-TDDFT) realisiert. Um die Fähigkeit der neuartigen RT-Methodik zur Simulation von RR-Spektren zu untersuchen, wurde diese am Beipiel von ortho-Nitrophenol eingesetzt und mit den Ergebnissen zweier etablierter Verfahen zur Simulation von RR-Spektren verglichen, genauer gesagt der vibronischen Methode (in der Kurzzeit-Näherung) und der Methode zur Beschreibung von dynamischen Polarisierbarkeiten. Der direkte Vergleich der drei Methoden erlaubt eine Validierung des RT-Ansatzes zur Simulation von RR-Intensitäten und Schwingungsfrequenzen, wobei festgestellt wurde, dass alle drei Methoden konsistente Resultate erbringen. Es konnte somit gezeigt werden, dass der RT-Ansatz neben seiner ursprünglichen Bestimmung zur Beschreibung von SERS-Spektren ebenso zur Vorhersage von RR-Spektren geeignet ist.

Wie bereits beschrieben, werden neben Resonanzen mit angeregten elektronischen Zuständen von Molekülen (RR-Spektroskopie) auch Plasmon-Resonanzen (SERS und TERS) zur Verstärkung des Raman-Signals eingesetzt. Daher ist für die (quantenmechanische) Beschreibung des letzteren Falles, die Einbeziehung des plasmon-aktiven Nanopartikels unabdingbar. Für die ausschließlich theoretisch untersuchte Diskrimierung von *cis*- und *trans*-penta-2,4-diencarbon säure (PDAH) mittels RR- bzw. SERRS (oberflächenverstärkter RR-Spektroskopie) wurden daher Gold-Nanocluster verschiedener Größe in die quantenchemischen Rechnungen einbezogen. Daher stand neben der spektroskopischen Unterscheidung beider Isomere der Einfluß des Goldclusters, dessen Größe und die chemische Interaktion zwischen Cluster und PDAH im Fokus. Zusätzlich zur RR- und SERRS-Spektroskopie wurden ebenso die Infrarot- (IR-), die nicht-resonante Ramanspektroskopie und die UV-Vis-Spektroskopie zur Untersuchung des lichtinduzierten, molekularen *cis-trans* Schalters verwendet. Wie mittels IR- und nicht-resonanter-Raman-Spektroskopie gezeigt werden konnte, kommt es im elektronischen Grundzustand von (*cis*- und *trans*-)PDAH zu einer partiellen Enolisierung aufgrund der Wechselwirkung mit dem Nanopartikel, welche die IR- und Raman-Spektren im Vergleich zum isolierten PDAH beeinflußt. Der Grad der Enolisierung steigt mit der Clustergröße (1, 2 und 20 Atomen) an, allerdings ist eine Unterscheidung beider Isomere (auch in Abhängigkeit der Clustergröße) nicht möglich. Interessanterweise zeigen die angeregten Zustände das Au-PDAH-System eine ausgeprägte Vermischung von PDAH-zentrierten lokalen Anregungen des π-Systems mit metall-zentrierten Zuständen des Goldclusters, wobei das Ausmaß dieser Mischung

der Zustände mit der Clustergröße steigt. Allerdings zeigt sich im Falle des *cis*-Isomers gegenüber der *trans*-Isomers ein geringerer Grad der Mischung. Dieser Unterschied in der Mischung der IL Zustände zwischen beiden Isomeren beeinflusst die Art und Weise wie die Normalmoden mit Beteiligung der Doppelbindungen des PDAH Moleküls während des RR-Prozess aktiviert werden. Folglich stellt die RR-Spektroskopie ein geeignetes Werkzeug für die Unterscheidung der an Goldnanopartikeln gebundenen PDAH Isomere dar. Auch die hohe spektrale Auflösung, die die RR-Spektren aufweisen, tragen dazu bei, eine deutliche Unterscheidung zwischen den Spektren beider Isomere zu erreichen.

Variiert man die plasmonisch-aktive Oberfläche in SERS hin zu einem Nanopartikel, resultieren lokalbegrenzte Interaktionen des Metalls und dem sensibilisierten Probemolekül. Diese lokal sehr beschränkten Wechselwirkungen in der TERS-Spektroskopie und der daraus resultierenden möglichen lateralen Auflösungen, bis hin in den Ångström-Bereich, werden derzeit kontrovers diskutiert. Um die Möglichkeit einer solchen lateralen Auflösung der TERS-Spektroskopie bis in den Ångström-Bereich mittels quantenchemischer Methoden zu untersuchen, wurde ein Modelsystem aus einem flach orientierten Adenin-Molekül und einem dazu senkrecht ausgerichteten Silber-Nanopartikel verwendet. Dabei wurde der Nanopartikel mittels eines einzigen Silberatoms, sowie eines kleinen Clusters, bestehend aus 20 Silberatomen, modelliert. Letzteres Modell berücksichtigt neben den Wechselwirkungen über das äußerste Silberatom ebenso Wechselwirkungen über die zweite und dritte Silberlage im Cluster. DFT-Rechnungen entlang eines vordefinierten 3D-Gitters ermöglichen die Beschreibung des chemischen Effektes, und somit der Potentiallandschaft über das 3D-Gitter und der TERS-Spektren in jedem Gitterpunkt. Die TERS-Spektren wurden dabei ausschließlich unter Berücksichtigung der z-Komponente der Ableitung des Polarisierbarkeitstensors, welche im Modell senkrecht zur Adeninmolekülebene orientiert ist, entlang der 3N-6 Normalmoden simuliert. Die Intensität einer i-ten Mode ergibt sich somit proportional zu $\left|\frac{\partial(\alpha_{zz})_l}{\partial q_l}\right|^2$. Unabhängig von der verwendeten Clustergröße prognostizieren beide Modelle eine mögliche Auflösung von TERS bis in das Ångstöm-Regime hinein. Ausgeprägte Abhängigkeiten der Raman-Intensitätsmuster von der Position des Silbers in Bezug auf das Adenin-Molekül konnten ermittelt werden. Dabei konnten Verstärkungen der Intensitäten einzelner Moden um bis zu 3500 Einheiten, ausschließlich unter Berücksichtigung des chemischen Effektes, berechnet werden. Momentan,von einem experimentellen Standpunkt aus, ist eine Auflösung unterhalb des Ångström-Regimes unrealistisch aufgrund mehrerer Faktoren (z.B. Spitzenpositionierungsrauschen und thermische Drift der Probe). Dem laterale Kontrast in den musten TERS Experimenten erhalten jedoch Rastersondensysteme, welche Sub-Nanometer Stabilisierung verwenden, kann mit den Ergebnissen in dieser Arbeit zu einem gewissen Grad

erklärt werden.

Die vorliegende Dissertation beschäftigt sich mit der quantenchemischen Beschreibung (hoch)moderner Raman-spektroskopischer Verfahren, d.h. der RR-, der SERS- und der TERS-spektroskopie. Für die Plasmon-verstärkten Verfahren (SERS und TERS) stand die Beschreibung der chemischen Wechselwirkung zwischen dem Plasmon-aktiven Metall-nanopartikel und des Probemoleküls auf molekularer Ebene im Fokus der Untersuchung. Im Bereich der TERS-Spektroskopie konnte erstmals mittels eines reinen quantenmechanischen Ansatzes eine laterale Auflösung im Ångstöm-Bereich vorausgesagt werden.

Bibliography

[1] Raman, C. V. ; Krishnan, K. S. *Proc. Indian Assoc. Cultiv. Sci.* **11**, 387–398 (1927-1928).

[2] Raman, C. V. ; Krishnan, K. S. *Nature* **121**(3048), 501–502 (1928).

[3] Raman, C. V. ; Krishnan, K. S. *Nature* **121**(3053), 711 (1928).

[4] Raman, C. V. ; Krishnan, K. S. *Nature* **122**(3066), 169 (1928).

[5] Long, D. *The Raman effect: a unified treatment of the theory of Raman scattering by molecules.* Wiley, Chichester, (2002).

[6] Wächtler, M., Guthmuller, J., González, L., and Dietzek, B. *Coord. Chem. Rev.* **256**, 1479 – 1508 (2012).

[7] Hu, S., Smith, K. M., and Spiro, T. G. *J. Am. Chem. Soc.* **118**(50), 12638–12646 (1996).

[8] Tschierlei, S., Presselt, M., Kuhnt, C., Yartsev, A., Pascher, T., Sundström, V., Karnahl, M., Schwalbe, M., Schäfer, B., Rau, S., Schmitt, M., Dietzek, B., and Popp, J. *Chem. Eur. J.* **15**(31), 7678–7688 (2009).

[9] Tschierlei, S., Karnahl, M., Presselt, M., Dietzek, B., Guthmuller, J., González, L., Schmitt, M., Rau, S., and Popp, J. *Angew. Chem. Int. Ed.* **49**(23), 3981–3984 (2010).

[10] Guthmuller, J. and González, L. *Phys. Chem. Chem. Phys.* **12**, 14812–14821 (2010).

[11] Fleischmann, M., Hendra, P., and McQuillan, A. *Chem. Phys. Lett.* **26**(2), 163–166 (1974).

[12] Ritchie, R. H. *Phys. Rev.* **106**, 874–881 Jun (1957).

[13] Morton, S. M., Silverstein, D. W., and Jensen, L. *Chem. Rev.* **111**(6), 3962–3994 (2011).

[14] Chiang, N., Jiang, N., Chulhai, D. V., Pozzi, E. A., Hersam, M. C., Jensen, L., Seideman, T., and Van Duyne, R. P. *Nano Letters* **15**(6), 4114–4120 (2015).

[15] Chulhai, D. V. and Jensen, L. *J. Phys. Chem. C* **117**(38), 19622–19631 (2013).

[16] Corni, S. and Tomasi, J. *J. Chem. Phys.* **114**(8), 3739–3751 (2001).

[17] Corni, S. and Tomasi, J. *Chem. Phys. Lett.* **342**(1-2), 135–140 (2001).

[18] Corni, S. and Tomasi, J. *J. Chem. Phys.* **116**(3), 1156–1164 (2002).

[19] Corni, S. and Tomasi, J. *J. Chem. Phys.* **117**(15), 7266–7278 (2002).

[20] Thomas, M., Mühlig, S., Deckert-Gaudig, T., Rockstuhl, C., Deckert, V., and Marquetand, P. *J. Raman Spec.* **44**, 1497–1505 (2013).

[21] Zhang, C., Chen, B.-Q., and Li, Z.-Y. *J. Phys. Chem. C* **119**(21), 11858–11871 (2015).

[22] Jensen, L., Aikens, C. M., and Schatz, G. C. *Chem. Soc. Rev.* **37**(5), 1061–1073 (2008).

[23] Jensen, F. *Introduction to Computational Chemistry.* John Wiley & Sons, Ltd, 2 edition, (2007).

[24] Latorre, F., Guthmuller, J., and Marquetand, P. *Phys. Chem. Chem. Phys.* **17**(12), 7648–7658 (2015).

[25] Liu, S., Zhao, X., Li, Y., Chen, M., and Sun, M. *Spectrochim. Acta A* **73**(2), 382–387 (2009).

[26] Zhao, L., Jensen, L., and Schatz, G. C. *J. Am. Chem. Soc.* **128**(9), 2911–2919 (2006).

[27] Xu, H., Wang, X.-H., Persson, M. P., Xu, H. Q., Käll, M., and Johansson, P. *Phys. Rev. Lett.* **93**, 243002 (2004).

[28] Johansson, P., Xu, H., and Käll, M. *Phys. Rev. B* **72**, 035427 (2005).

[29] Lopata, K. and Neuhauser, D. *J. Chem. Phys.* **130**(10), 104707 (2009).

[30] Payton, J. L., Morton, S. M., Moore, J. E., and Jensen, L. *J. Chem. Phys.* **136**(21), 214103 (2012).

[31] Payton, J. L., Morton, S. M., Moore, J. E., and Jensen, L. *Accounts of Chemical Research* **47**(1), 88–99 (2014).

[32] Chen, H., McMahon, J. M., Ratner, M. A., and Schatz, G. C. *J. Phys. Chem. C* **114**(34), 14384–14392 (2010).

[33] Chen, H., Blaber, M. G., Standridge, S. D., DeMarco, E. J., Hupp, J. T., Ratner, M. A., and Schatz, G. C. *J. Phys. Chem. C* **116**(18), 10215–10221 (2012).

[34] Pettinger, B., Schambach, P., Villagómez, C. J., and Scott, N. *Annu. Rev. Phys. Chem.* **63**(1), 379–399 (2012).

[35] Kumar, N., Mignuzzi, S., Su, W., and Roy, D. *EPJ T* **2**(1), 1–23 (2015).

[36] Wessel, J. *J. Opt. Soc. Am. B* **2**(9), 1538–1541 (1985).

[37] Zhang, R., Zhang, Y., Dong, Z. C., Jiang, S., Zhang, C., Chen, L. G., Zhang, L., Liao, Y., Aizpurua, J., Luo, Y., Yang, J. L., and Hou, J. G. *Nature* **498**(7452), 82–86 (2013).

[38] Singh, P. and Deckert, V. *Chem. Commun.* **50**(76), 11204–11207 (2014).

[39] Klingsporn, J. M., Jiang, N., Pozzi, E. A., Sonntag, M. D., Chulhai, D., Seideman, T., Jensen, L., Hersam, M. C., and Duyne, R. P. V. *J. Am. Chem. Soc.* **136**(10), 3881–3887 (2014).

[40] Deckert-Gaudig, T., Kämmer, E., and Deckert, V. *J. Biophotonics* **5**(3), 215–219 (2012).

[41] Downes, A., Salter, D., and Elfick, A. *J. Microsc.* **229**(2), 184–188 (2008).

[42] Geshev, P. I., Klein, S., Witting, T., Dickmann, a., and Hietschold, M. *Phys. Rev. B* **70**(7), 075402 (1–16) (2004).

[43] Martin, Y. C., Hamann, H. F., and Wickramasinghe, H. K. *J. Appl. Phys.* **89**(10), 5774–5778 (2001).

[44] Notingher, I. and Elfick, A. *J. Phys. Chem. B* **109**(33), 15699–15706 (2005).

[45] Browne, W. and Feringa, B. *Annu. Rev. Phys. Chem.* **60**, 407–428 (2009).

[46] Yasuda, S., Nakamura, T, M. M., , and Shigekawa, H. *J. Am. Chem. Soc.* **125**(52), 16430–16433 (2003).

[47] Bettega, H. C.-Y., Hissler, M., Moutet, J.-C., and Ziessel, R. *Chem. Mater.* **9**(1), 3–5 (1997).

[48] de Ruiter, G., Gupta, T., and van der Boom, M. E. *J. Am. Chem. Soc.* **130**(9), 2744–2745 (2008).

[49] Rogers, J. A., Bao, Z., Baldwin, K., Dodabalapur, A., Crone, B., Raju, V. R., Kuck, V., Katz, H., Amundson, K., Ewing, J., and Drzaic, P. *Proc Natl Acad Sci U S A* **98**(9), 4835–4840 (2001).

[50] Feringa, B. and Browne, W. *Molecular Switches, Second Edition,* volume 1. (2011).

[51] Marquetand, P., Nuernberger, P., Brixner, T., and Engel, V. *J. Chem. Phys.* **129**(7), 074303 (2008).

[52] Kinzel, D., Marquetand, P., and González, L. *J. Phys. Chem. A* **116**(11), 2743–2749 (2012).

[53] Klaumünzer, B. and Kröner, D. *New J. Chem.* **33**, 186–195 (2009).

[54] Hoki, K., Sato, M., Yamaki, M., Sahnoun, R., Gonzalez, L., Koseki, S., and Fujimura, Y. *J. Phys. Chem. B* **108**, 4916–4921 (2004).

[55] Bajo, J. J., González-Vázquez, J., Sola, I., Santamaria, J., Richter, M., Marquetand, P., and González, L. *J. Phys. Chem. A* **116**(11), 2800–2807 (2012).

[56] Rowan, R., Warshel, A., Skyes, B. D., and Karplus, M. *Biochem.* **13**(5), 970–981 (1974).

[57] Dugave, C. and Demange, L. *Chem. Rev.* **103**(7), 2475–2532 (2003).

[58] Weigelt, S., Busse, C., Petersen, L., Rauls, E., Hammer, B., Gothelf, K., Besenbacher, F., and Linderoth, T. *Nat. Mater.* **5**(2), 112–117 (2006).

[59] Born, M. and Oppenheimer, R. *Ann. Phys.* **389**(20), 457–484 (1927).

[60] Slater, J. C. *Phys. Rev.* **34**(10), 1293–1322 (1929).

[61] Pauli, W. *Z. Phys.* **31**(1), 765–783 (1925).

[62] Hartree, D. R. *Math. Proc. Cambridge* **24**(01), 89–110 (1928).

[63] Roothaan, C. C. J. *Rev. Mod Phys.* **23**(2), 69–89 (1951).

[64] Hall, G. G. *P. Roy. Soc. Lond. A. Mat.* **205**(1083), 541–552 (1951).

[65] Slater, J. C. *Phys. Rev.* **32**(3), 339–348 (1928).

[66] Löwdin, P. *Adv. Chem. Phys.* **2**, 207–322 (1959).

[67] Hohenberg, P. and Kohn, W. *Phys. Rev.* **136**, B864–B871 (1964).

[68] Levine, I. N. *Quantum Chemistry.* Prentice Hall, (2001).

[69] Stowasser, R. and Hoffmann, R. *J. Am. Chem. Soc.* **121**(14), 3414–3420 (1999).

[70] Kohn, W. and Sham, L. J. *Phys. Rev.* **140**, 1133–1138 (1965).

[71] Slater, J. C. *The Self-Consistent Field for Molecular and Solids, Quantum Theory of Molecular and Solids.* McGraw-Hill, (1974).

[72] Vosko, S. H., Wilk, L., and Nusair, M. *Can. J. Phys.* **58**(8), 1200–1211 (1980).

[73] Slater, J. C. *Phys. Rev. B* **58**, 1200–1211 (1951).

[74] Becke, A. D. *Phys. Rev. A* **38**, 3098–3100 (1988).

[75] Lee, C., Yang, W., and Parr, R. G. *Phys. Rev. B* **37**, 785–789 (1988).

[76] Perdew, J. P., Chevary, J. A., Vosko, S. H., Jackson, K. A., Pederson, M. R., Singh, D. J., and Fiolhais, C. *Phys. Rev. B* **46**, 6671–6687 (1992).

[77] Perdew, J. P., Burke, K., and Ernzerhof, M. *Phys. Rev. Lett.* **77**, 3865–3868 (1996).

[78] Koch, W. and Holthausen, M. C. *A Chemist's Guide to Density Functional Theory.* Wiley-VCH, Weinheim, (2001).

[79] Lee, C., Yang, W., and Parr, R. G. *Phys. Rev. B* **37**(2), 785 (1988).

[80] Yanai, T., Tew, D. P., and Handy, N. C. *Chemical Physics Letters* **393**(1-3), 51 – 57 (2004).

[81] Runge, E. and Gross, E. K. U. *Phys. Rev. Lett.* **52**, 997–1000 (1984).

[82] Marques, M. A. L., U. C. A. N. F. R. A. B. K. and Gross, E. K. U. *Lect. Notes Phys.* **837**, 53–99 (2012).

[83] Castro, A., Marques, M. A. L., and Rubio, A. *J. Chem. Phys.* **121**(8), 3425–3433 (2004).

[84] Slater, J. *Phys. Rev.* **36**, 57–64 (1930).

[85] Kato, T. *Commun. Pure Appl. Math.* **10**, 151–177 (1957).

[86] Boys, S. F. *Proc. R. Soc. London Ser. A* **200** (1950).

[87] Krishnan, R., Binkley, J. S., Seeger, R., and Pople, J. A. *J. Chem. Phys.* **72**(1), 650–654 (1980).

[88] Burkatzki, M., Filippi, C., and Dolg, M. *J. Chem. Phys.* **126**(23), 234105 (2007).

[89] Hilborn, R. C. *Am. J. Phys.* **50**(11), 982 (1982).

[90] Einstein, A. and Stern, O. *Ann. Phys.* **345**(3), 551–560 (1913).

[91] Smekal, A. *Naturwiss.* **11**, 873–875 (1923).

[92] Kramers, H. and Heisenberg, W. *Z. Phys. A: Hadrons Nucl.* **31**, 681–708 (1925).

[93] Dirac, P. A. M. *Proc. R. Soc. London, Ser. A* **114**(769), 710–728 (1927).

[94] Franck, J. *Trans. Faraday Soc.* **21**, 536–542 (1926).

[95] Condon, E. U. *Phys. Rev.* **28**, 1182–1201 (1926).

[96] Condon, E. U. *Phys. Rev.* **32**, 858–872 (1928).

[97] Jensen, L., Zhao, L. L., Autschbach, J., and Schatz, G. C. *J. Chem. Phys.* **123**(17), 174110 (2005).

[98] Hizhnyak, V. and Tehver, I. *Phys. Status Solid* **21**, 755–768 (1967).

[99] Tonks, D. L. and Page, J. B. *Chem. Phys. Lett.* **66**, 449–453 (1979).

[100] Blazej, D. C. and Peticolas, W. L. *J. Chem. Phys.* **72**, 3134–3142 (1980).

[101] Page, J. B. and Tonks, D. L. *J. Chem. Phys.* **75**, 5694–5708 (1981).

[102] Peticolas, W. L. and Rush, T. *J. Comput. Chem.* **16**(10), 1261–1270 (1995).

[103] Heller, E. J., Sundberg, R., and Tannor, D. *J. Phys. Chem.* **86**(10), 1822–1833 (1982).

[104] Guthmuller, J. *J. Chem. Theory Comput.* **7**(4), 1082–1089 (2011).

[105] Adamo, C. and Barone, V. *J. Chem. Phys.* **110**(13), 6158–6170 (1999).

[106] VandeVondele, J., Krack, M., Mohamed, F., Parrinello, M., Chassaing, T., and Hutter, J. *Comput. Phys. Commun.* **167**(2), 103–128 (2005).

[107] Krack, M. *Theor. Chem. Acc.* **114**, 145–152 (2005).

[108] Genovese, L., Deutsch, T., Neelov, A., Goedecker, S., and Beylkin, G. *J. Chem. Phys.* **125**(7), 074105 (2006).

[109] Baerends, E. J., Autschbach, J., Bérces, A., Bickelhaupt, F. M., Bo, C., Boerrigter, P. M., Cavallo, L., Chong, D. P., Deng, L., Dickson, R. M., Ellis, D. E., van Faassen, M., Fan, L., Fischer, T. H., Guerra, C. F., van Gisbergen, S. J. A., Groeneveld, J. A., Gritsenko, O. V., Grüning, M., Harris, F. E., van den Hoek, P., Jacob, C. R., Jacobsen, H., Jensen, L., van Kessel, G., Kootstra, F., van Lenthe, E., McCormack, D. A., Michalak, A., Neugebauer, J., Osinga, V. P., Patchkovskii, S., Philipsen, P. H. T., Post, D., Pye, C. C., Ravenek, W., Ros, P., Schipper, P. R. T., Schreckenbach, G., Snijders, J. G., Solá, M., Swart, M., Swerhone, D., te Velde, G., Vernooijs, P., Versluis, L., Visscher, L., Visser, O., Wang, F., Wesolowski, T. A., van Wezenbeek, E., Wiesenekker, G., Wolff, S., Woo, T., Yakovlev, A., and Ziegler, T. URL http://www.scm.com.

[110] Chong, D. P., Van Lenthe, E., Van Gisbergen, S., and Baerends, E. J. *J. Comput. Chem.* **25**(8), 1030–1036 (2004).

[111] Frisch, M. J., Trucks, G. W., Schlegel, H. B., Scuseria, G. E., Robb, M. A., Cheeseman, J. R., Scalmani, G., Barone, V., Mennucci, B., Petersson, G. A., Nakatsuji, H., Caricato, M., Li, X., Hratchian, H. P., Izmaylov, A. F., Bloino, J., Zheng, G., Sonnenberg, J. L., Hada, M., Ehara, M., Toyota, K., Fukuda, R., Hasegawa, J., Ishida, M., Nakajima, T., Honda, Y., Kitao, O., Nakai, H., Vreven, T., Montgomery, J. A., Jr., Peralta, J. E., Ogliaro, F., Bearpark, M., Heyd, J. J., Brothers, E., Kudin, K. N., Staroverov, V. N., Kobayashi, R., Normand, J., Raghavachari, K., Rendell, A., Burant, J. C., Iyengar, S. S., Tomasi, J., Cossi, M., Rega, N., Millam, J. M., Klene, M., Knox, J. E., Cross, J. B., Bakken, V., Adamo, C., Jaramillo, J., Gomperts, R., Stratmann, R. E., Yazyev, O., Austin, A. J., Cammi, R., Pomelli, C., Ochterski, J. W., Martin, R. L., Morokuma, K., Zakrzewski, V. G., Voth, G. A., Salvador, P., Dannenberg, J. J., Dapprich, S., Daniels, A. D., Farkas, Ö., Foresman, J. B., Ortiz, J. V., Cioslowski, J., , and Fox, D. J. Gaussian, Inc.: Wallingford CT, 2009.

[112] Petersson, G. A. and Al Laham, M. A. *J. Chem. Phys.* **94**(9), 6081–6090 (1991).

[113] Assadollahzadeh, B. and Schwerdtfeger, P. *J. Chem. Phys.* **131**(6), 064306 (2009).

[114] Schooss, D., Weis, P., Hampe, O., and Kappes, M. *Phil. Trans. R. Soc. A* **368**(1915), 1211–1243 (2010).

[115] Gruene, P., Rayner, D., Redlich, B., Van Der Meer, A., Lyon, J., Meijer, G., and Fielicke, A. *Science* **321**(5889), 674–676 (2008).

[116] Guthmuller, J. and Champagne, B. *J. Chem. Phys.* **127**(16), 164507 (2007).

[117] Kamiya, I., Tsunoyama, H., Tsukuda, T., and Sakurai, H. *Chem. Lett.* **36**(5), 646–647 (2007).

[118] Merrick, J. P., Moran, D., and Radom, L. *J. Phys. Chem. A* **111**(45), 11683–11700 (2007).

[119] Esperdy, K. and Shillady, D. D. *J. Chem. Inf. Comput. Sci.* **41**(6), 1547–1552 (2001).

[120] Mukherjee, S., Libisch, F., Large, N., Neumann, O., Brown, L. V., Cheng, J., Lassiter, J. B., Carter, E. A., Nordlander, P., and Halas, N. J. *Nano Lett.* **13**(1), 240–247 (2013).

[121] Knight, M. W., Wang, Y., Urban, A. S., Sobhani, A., Zheng, B. Y., Nordlander, P., and Halas, N. J. *Nano Lett.* **13**(4), 1687–1692 (2013).

[122] Quack, M. *Fundamental Symmetries and Symmetry Violations from High Resolution Spectroscopy*. John Wiley & Sons, Ltd (2011).

[123] Lombardi, J. R. and Birke, R. L. *J. Phys. Chem. C* **112**(14), 5605–5617 (2008).

[124] Thomas, M., Mühlig, S., Deckert-Gaudig, T., Rockstuhl, C., Deckert, V., and Marquetand, P. *J. Raman Spec.* **44**, 1497–1505 (2013).

[125] Negri, F., Castiglioni, C., Tommasini, M., and Zerbi, G. *J. Phys. Chem. A* **106**(14), 3306–3317 (2002).

[126] Rasmussen, A. and Deckert, V. *J. Raman Spectrosc.* **37**(1-3), 311–317 (2006).

[127] Huang, R., Yang, H.-T., Cui, L., Wu, D.-Y., Ren, B., and Tian, Z.-Q. *J. Phys. Chem. C* **117**(45), 23730–23737 (2013).

[128] Mohamed, T. A., Shabaan, I. A., Zoghaib, W. M., Husband, J., Farag, R. S., and Alajhaz, A. E.-N. M. A. *J. Mol. Struct.* **938**(1-3), 263–276 (2009).

[129] Giese, B. and McNaughton, D. *J. Phys. Chem. B* **106**(1), 101–112 (2002).

[130] Watanabe, H., Ishida, Y., Hayazawa, N., Inouye, Y., and Kawata, S. *Phys. Rev. B* **69**(15), 155418 (1–11) (2004).

[131] Hayazawa, N., Watanabe, H., Saito, Y., and Kawata, S. *J. Chem. Phys.* **125**(24), 244706 (1–7) (2006).

[132] Domke, K. F., Zhang, D., and Pettinger, B. *J. Am. Chem. Soc.* **129**(21), 6708–6709 (2007).

[133] Hariharan, P. C. and Pople, J. A. *Theor. Chim. Acta* **28**(3), 213–222 (1973).

[134] Sonntag, M. D., Chulhai, D., Seideman, T., Jensen, L., and Van Duyne, R. P. *J. Am. Chem. Soc.* **135**(45), 17187–17192 (2013).

Chapter 7

Acknowledgements

Here I would like to thank all the people that contributed to finish my thesis. First, I would like to thank my parents, **Federico** and **Trinidad**, for their support and education they have given me that allowed me to complete this difficult task such as is a doctoral thesis. Especially I'm grateful to my mother for taking care of me all the time. Furthermore, I would like to thank my closest friends in Valencia, **Beltrán**, **María** and **Ximo**, for always being there to help me relax at my hometown during the last years.

Moreover, I would like to show gratitude to PD Dr. **Belén Ruiz** for giving me an opportunity to start my first scientific research under her supervision in the Friedrich-Alexander Universität Erlangen. Thanks to her supervision prior to finish my Chemistry studies in the Universidad de Valencia, I could get a chance to start this thesis. This thesis was prepared in the working group of Prof. Dr. **Leticia González** at Wien Universität. I am very grateful to her for giving me the chance to do my PhD in her group. Also I would like to thank Prof. Dr. **Volker Deckert** and Prof. Dr. **Stefanie Gräfe** and their respective groups at the Friedrich-Schiller-Universität Jena for accepting me in their groups and offering me the chance to do the last research that completed this thesis.

Of fundamental importance for this thesis are Dr. **Julien Guthmuller**, for teaching me on the topic of Raman spectroscopy and its variants, and Dr. **Philipp Marquetand** for continuing my formation in the topic and his supervision of my work in my time at Wien Universität.

Special thanks goes to my good friends and fellow colleagues Dr. **Stephan Kupfer**, Dr. **Martin Richter**, Dr. **David Hierro**, Dr. **Juanjo Nogueira**, Dr. **Daniel Kinzel** and Dr. **Mariana Aßmann**. Your support and company made the time in the office and life in Vienna and Jena more pleasant. I hope our friendship lasts beyond the end of this thesis. Also, I would like to thank the rest of my colleagues that I share many memories in the groups at Vienna and Jena.

I want to finish this chapter with the people that accompanied me during my last years in Jena. Firstly I want to thank the **Seishinkai kendo club** in Jena for accepting me in their trainings and help me to improve my kendo skills under their tutelage. Also I want to thank **Antonio** for organizing the Spanish Stammtisch every week that let me meet some interesting people, particularly, **Asami Namikawa**. Thanks to you, Asami, for contributing to improve my life in Jena during these last months.

Selbstständigkeitserklärung

Hiermit erkläre ich, dass ich diese Arbeit selbstständig und ohne Zuhilfenahme weiterer als der angegebenen Hilfsmittel angefertig habe. Alle verwendeten Textausschnitte, Zitate oder Inhalte anderer Verfasser wurden ausdrücklich als solche gekennzeichnet.

Federico Latorre

Curriculum vitae

Pesonal data

Name	Federico Manuel Latorre Contreras
Birth	25th August 1985, 46009 Valencia
Citizenship	Spain
Nationality	Spanish
personal status	unmarried
E-mail	latorrf3@gmail.com

Scientific experience

12/2015	Researcher in the theoretical chemistry group of Prof. Dr. Gräfe at the University of Jena, Germany
01/2015–08/2015	Researcher in the nano-spectroscopy group of Prof. Dr. Deckert at the University of Jena, Germany
08/2011–08/2016	Doctoral studies in the group of Prof. Dr. Leticia González at the Institute of Physical Chemistry, Friedrich-Schiller-University Jena, Germany
09/2009 - 06/2010	Research project under the supervision of M. B. Ruiz at the University of Erlangen, Germany

Degrees and education

06/2011	Diploma in Chemistry
09/2004–06/2011	Studies of Chemistry, Universidad de Valencia, Spain
09/2002–06/2004	Bachillerato studies, I.E.S Benlliure, Valencia
09/2001–06/2002	E.S.O. studies, I.E.S Benlliure, Valencia

Complementary training in foreign laboratories

04-08/06/2012	Training School on the Dynamics of Molecular Excited States Induced by Ultrashort Pulses, Zaragoza, Spain

Language skills

Spanish	Mother tongue
English	Fluent in writing and speaking
German	Basic knowledge

IT skills

Scientific	Quantum chemistry suites (Gaussian 09, ORCA, ADF), molecular and scientific visualization software, LaTeX
General	Office suites, Windows and UNIX/Linux based OSs

List of Publications

1. Latorre, F., Kupfer, S., Bocklitz, T., Kinzel, D., Trautmann, S., Gräfe, S. and Deckert V.
   Spatial Resolution of Tip-Enhanced Raman Spectroscopy - DFT Assessment of the Chemical Effect
   Nanoscale **8**, 10229-10239 (2016)

2. Ruiz, M. B. , Latorre, F. and Frolov, A. M.
   Chapter Five: Singlet and Triplet Bound State Spectra in the Four-Electron Be-Like Atomic Systems
   Advances in Quantum Chemistry **73**, 119-138, Academic Press, (2016).

3. Latorre, F., Guthmuller, J., and Marquetand, P.
   A spectroscopic study of the cis/trans-isomers of penta-2,4-dienoic acid attached to gold nanoclusters
   Phys. Chem. Chem. Phys. **12**, 7648-7658 (2015)

4. Thoma, M., Latorre, F. and Marquetand, P.
   Resonance Raman spectra of ortho-nitrophenol calculated by real-time time-dependent density functional theory
   J. Chem. Phys. **138**, 044101 (2013).